Experimental Evaluation of Advanced Diffusion MRI Methods Towards Improved Assessment of Myelinated Neural Tissue

By

Nathaniel D. Kelm

Dissertation

Submitted to the Faculty of the

Graduate School of Vanderbilt University

in partial fulfillment of the requirements

for the degree of

DOCTOR OF PHILOSOPHY

In

Biomedical Engineering

May, 2017

Nashville, Tennessee

Approved:

Mark D. Does, Ph.D.

John C. Gore, Ph.D.

Adam W. Anderson, Ph.D.

Robert P. Carson, M.D., Ph.D.

Wesley P. Thayer, M.D., Ph.D.

To my sweet daughter, Emma, who brings such joy to my life

and

To my amazing wife, Jessica, who has been extremely loving and supportive

ACKNOWLEDGEMENTS

This work was made possible through financial support from multiple funding sources, including grants for Sub-voxel Tissue Characterization with MRI and MRI Toolbox for Rodent Brain Microstructure Imaging, as well as a T32 institutional training grant, from the National Institute of Health. I would like to thank my collaborators from the Carson and Thayer labs, who provided the animal models that formed the foundation for much of this work. Also, I would like to thank Dr. Gore and all of the staff and resources at the Vanderbilt University Institute of Imaging Science for their substantial support. I have enjoyed working in such a friendly, collaborative environment and am thankful for the training I received at such a prestigious institution. Next, I would like to thank the Does lab for inspiration and fruitful discussion, especially Kathryn, who contributed significantly to this work. I would like to especially thank my advisor, Dr. Mark Does, for his mentorship and training over the years. I truly appreciate the time he has invested in my development as a researcher and for instilling in me the importance of detailed experimental design, critical thought, and effective communication.

I am extremely grateful for all of my friends and family who have been understanding throughout this entire process, including my parents-in-law Dan and Traci Beard, who have always been a source of encouragement and support. I would like to especially thank my parents, Randy and Sandy Kelm, who taught me the importance of education and hard work, but more importantly, to be a better person. I also wish to thank my daughter, Emma, who brings me joy each and every day and motivates me to do my best. Most importantly, I would like to thank my wife, Jessica, who has been with me every step of this journey, for her overwhelming love, patience, and encouragement.

TABLE OF CONTENTS

Page

LIST OF TABLES

LIST OF FIGURES

LIST OF ABBREVIATIONS

AC – anterior commissure

AD – axial diffusivity

AK – axial kurtosis

AKT – protein kinase B

b – diffusion-weighting b-value

BW – receiver bandwidth

CKO – conditional knockout

CNS – central nervous system

CPMG – Carr-Purcell-Meiboom-Gill

δ – diffusion gradient pulse duration

Δ – diffusion time

d_a – axon diameter

D_a – intra-axonal diffusivity

$D_{e,\parallel}$ – extra-axonal axial diffusivity

$D_{e,\perp}$ – extra-axonal radial diffusivity

DKI – diffusion kurtosis imaging

DTI – diffusion tensor imaging

DWI – diffusion-weighted imaging

EC – external capsule

EM – electron microscopy

EPG – extended phase graph

EPI – echo-planar imaging

ESP – echo spacing

ETL – echo train length

F – fornix/fimbria of the hippocampus

FA – fractional anisotropy

f_a – histologic axon fraction

F_a – axonal water fraction

f_m – histologic myelin fraction

FOV – field of view

FSE – fast spin-echo

FSL – FMRIB software library

g – g-ratio

GCC – genu

GRASE – gradient and spin-echo

IC – internal capsule

MD – mean diffusivity

MERA – multi-exponential relaxation analysis

MET_2 – multi-exponential T_2

MidCC – midbody of the corpus callosum

MK – mean kurtosis

MR – magnetic resonance

MRI – magnetic resonance imaging

mTOR – mammalian target of rapamycin

MWF – myelin water fraction

NEX – number of excitations

NMR – nuclear magnetic resonance

NNLS – non-negative least squares

PBS – phosphate-buffered saline

PDF – probability density function

PGSE – pulsed gradient spin-echo

PI3K – phosphatidylinositide 3-kinase

PNS – peripheral nervous system

PSR – macromolecular pool-size ratio

qMT – quantitative magnetization transfer

ρ_a – myelinated axon density

RD – radial diffusivity

RK – radial kurtosis

ROI – region of interest

SCC – splenium

SEM – standard error of the mean

SNR – signal-to-noise ratio

TE – echo time

TI – inversion time

TR – repetition time

TSC – tuberous sclerosis complex

WM – white matter

WMTI – white matter tract integrity

z_m – myelin thickness

CHAPTER 1

INTRODUCTION

1.1 Motivation and Aims

Since its initial application in humans more than 30 years ago, magnetic resonance imaging (MRI) has revolutionized the field of medical imaging due to its excellent soft-tissue contrast and high resolution, making it particularly useful in non-invasive assessment of the nervous system. MRI exploits fundamental properties of atomic nuclei (in most cases, hydrogen protons) in the presence of an external magnetic field to essentially visualize water content, and therefore tissue, in the body. More specifically, MRI leverages a wide array of pulse sequence configurations to produce unique tissue contrasts related to intrinsic characteristics of the underlying tissue structure, such as proton density and relaxation. Currently, the majority of clinical MRI studies are based on qualitative evaluation of tissue contrast, yet in recent years, there has been a push in MR research for the development of quantitative MR biomarkers that offer improved assessment of neural tissue microstructure. The field of diffusion MRI or diffusion-weighted imaging (DWI), which involves the sensitization of the MR signal to the displacement of water molecules at the micron scale, has shown promise in the characterization of both healthy and pathological neural tissue. Since the displacement of water molecules is greatly influenced by barriers (e.g. cell membranes, myelin) present in neural tissue, measurement of this displacement can be highly sensitive to underlying microstructural changes.

One relatively common DWI method is diffusion tensor imaging (DTI), which describes the anisotropic behavior of diffusion, making it especially applicable for white matter imaging.

However, while basic DWI metrics, such as those from DTI, have shown to be sensitive to neural tissue, in many cases their specificity is inadequate for clinical diagnostic capability. Recently-developed advanced DWI models could offer both improved sensitivity and specificity, thereby providing further insight into neural tissue microstructure, but demands on hardware and scan duration make many of these not feasible for clinical applications. However, two of these models that are clinically practical, diffusion kurtosis imaging (DKI) and the DKI-based white matter tract integrity (WMTI) model, have shown promise in assessment of neural pathology, development, and injury, yet further experimental validation and application in various tissue models is necessary.

Due to the importance and complexity of the nervous system in the body, improved characterization of normal and pathological neural tissue would be extremely beneficial. Abnormal brain myelination is manifest in a variety of neurological diseases, including multiple sclerosis. Therefore, non-invasive assessment of myelin microstructure would be helpful in the diagnosis and treatment of such pathologies. Additionally, brain development involves complex changes in both axon and myelin structure. Various disorders, such as autism, exhibit alterations to the normal progression of white matter development, so an improved understanding of the underlying microstructure may aid in the advancement of therapies. Lastly, peripheral nerve injury and regeneration includes pronounced changes in axon and myelin microstructure, yet non-invasive diagnostic tests, particularly soon after injury, are limited. Non-invasive evaluation of peripheral nerve injury and regeneration would be valuable in determining the necessity of surgical intervention and improve the chances of fully-restored nerve function. Animal models that replicate the microstructural changes present in these conditions would be useful in evaluating the efficacy of quantitative MRI methods, such as DKI and WMTI, in

characterization of neural tissue, in addition to determining the potential of these methods to improve clinical diagnosis and treatment assessment.

Therefore, this work aims to elucidate the relationship between these advanced DWI models and neural microstructure in the following animal models:

1. Hypomyelinated and hypermyelinated mouse brain
2. Normally-developing and abnormally-developing mouse brain
3. Peripheral nerve injury and repair in rat sciatic nerve

1.2 Neural Tissue

Neurons are the primary functional cells in both the central nervous system (CNS) and peripheral nervous system (PNS) and are made up of three primary components: a cell body, an axon, and dendrites. Conventionally, dendrites receive neural signals and axons transmit them to other neurons, muscles, or glands through synapses. Myelin is an insulating lipid membrane wrapped in layers around axons of both the CNS and PNS that speeds up neuronal signal propagation along the axon as the signal jumps between non-myelinated sections called the nodes of Ranvier. Increases in axon diameter and the thickness of the myelin sheath each result in faster signal propagation along the axon (Hursh, 1939; Waxman, 1980). In the CNS, myelin is produced by oligodendrocytes, which branch and wrap myelin around multiple axons, whereas in the PNS, myelin is produced by Schwann cells, which support only a single axon.

In the CNS, neural tissue is separated into two major components: gray matter and white matter. Gray matter (so named because of its grayish appearance) is primarily composed of neuronal cell bodies, as well as glial cells, dendrites, and non-myelinated axons. On the other hand, white matter is mostly made up of myelinated axons, receiving its white coloring from the

lipid-based myelin sheaths wrapped around the axons. Generally speaking, neuronal signals are generated and processed in gray matter and rapidly transported between different sections of the CNS through white matter axons.

There are many neurological diseases and disorders, including multiple sclerosis (Kutzelnigg, 2005), schizophrenia (Davis et al., 2003), and tuberous sclerosis complex (Peters et al., 2012), that are characterized by abnormalities in CNS white matter. Changes in white matter that may impede proper function include axonal injury, reduction in the number of axons, decrease in axon diameter, decrease in myelin thickness, decrease in overall myelin content, and disorganization of fiber tracts. Although histological evaluation of these abnormalities can provide accurate quantitative measures, this is mostly limited to a small, pre-selected region of tissue and is not practical for widespread research in humans. The ability to non-invasively detect and specify microstructural changes in white matter would have a tremendous clinical impact. Non-invasive imaging sensitive to changes in white matter is essential for the early diagnosis of white matter diseases and the development of treatments and therapies.

1.3 Transgenic Mouse Models of Abnormal Myelination

The PI3K/AKT/mTOR (PI3K = phosphatidylinositide 3-kinase, AKT = protein kinase B, mTOR = mammalian target of rapamycin) pathway, shown in Fig. 1.1 (LaSarge and Danzer, 2014), is a prominent cell signaling pathway related to the regulation of different stages of the cell cycle, including cell division. In the nervous system, alterations in this signaling pathway can have a significant effect on various aspects of neural development, such as myelination. In this work, three conditional knockout (CKO) transgenic mouse models involving inactivation of genes in the PI3K/AKT/mTOR pathway, are investigated. Specifically, the targeted genes were *Tsc2*,

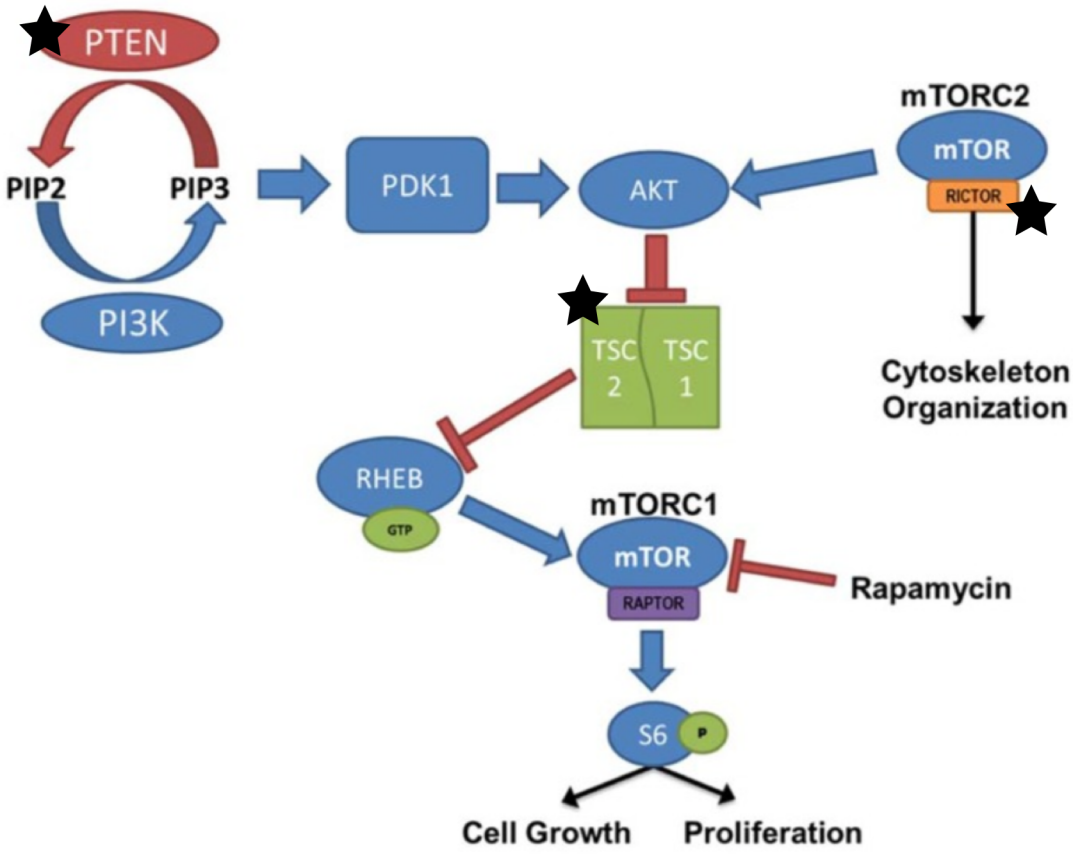

FIG. 1.1. PI3K/AKT/mTOR signaling pathway. The genes targeted in this work are indicated by back stars.

Rictor, and *Pten* (indicated with stars in Fig 1.1). For each of these models, Cre recombinase and the *Olig2* promoter were utilized to selectively delete the genes in oligodendrocyte precursor cells, ideally limiting its effects to myelin development.

Inactivation of these genes produces a wide range of phenotypes regarding myelin development. *Tsc2*, which codes for the protein tuberin, works with *Tsc1* to inhibit mTORC1 signaling and activate mTORC2 signaling. Deletion of either *Tsc1* or *Tsc2* causes an increase in mTORC1 signaling and a decrease in mTORC2 signaling, and is the cause of the human genetic disorder tuberous sclerosis complex. Selective inactivation of *Tsc2* using the *Olig2* promoter results in a decrease in the number of both mature and immature oligodendrocytes, causing a

severe reduction in myelination (Carson et al., 2015). *Rictor*, or rapamycin insensitive companion of mTOR, is a key requirement for mTORC2 signaling. Inactivation of the *Rictor* gene impairs mTORC2 signaling without affecting mTORC1 signaling. When *Rictor* is deleted in oligodendrocyte precursor cells, the result is a moderate hypomyelination phenotype, as opposed to the severe hypomyelination exhibited by the *Tsc2* CKO (Carson et al., 2013). *Pten*, which codes for the phosphatase and tensin homolog protein, regulates PI3K activity and has been identified as a tumor suppressor. Therefore, inactivation of *Pten* causes an increase in PI3K activity. When *Pten* is conditionally knocked out using the *Olig2* promoter, the increase in PI3K activity results in hypermyelination characterized by increased myelin thickness (Harrington et al., 2010). Since these models result in varied levels of myelination, they are valuable tools in the evaluation of the relationship between brain myelination and MR imaging methods.

1.4 Wallerian Degeneration

When axons are severed from the neuron cell body (i.e., axotomy), such as in a transection or crush injury in peripheral nerve, the axon segments distal to the injury degenerate in a process called Wallerian degeneration. Named after Augustus Waller, who first observed this degenerative process in frog nerves in the 19th century (Waller, 1850), Wallerian degeneration entails the breakdown of axonal membranes, fragmentation of myelin, and removal of axon and myelin debris by macrophages and Schwann cells distal to a nerve injury (Faweett and Keynes, 1990). Also, traumatic injury will induce edema around the injury site. Furthermore, the clean-up and recycling of axon and myelin fragments is crucial for proper nerve regeneration to take place.

Unlike the majority of the central nervous system, peripheral nerves are capable of regeneration after an injury. Within a day after axotomy, axons begin to regenerate from the proximal stump. As long as they are not inhibited by debris and the gap between the proximal and distal segments is not too large, axons will grow into the remaining endoneurial sheaths in the distal stump. In many cases of nerve transection, surgical repair is necessary to align the proximal and distal nerve segments and improve the chances of axons reaching their target. Axons will typically grow at a rate of approximately 1 mm per day, meaning that full regeneration in human peripheral nerve can take on the order of months.

A common model for studying peripheral nerve injury and repair is a crush or transection injury of rat sciatic nerve. In this model, soon after injury, edema appears near the injury site, yet distal axon degeneration may take up to 24 hours to begin. First axons, then myelin, degenerate distally away from the injury site and a proliferation of macrophages and Schwann cells occurs in order to remove axon and myelin fragments. After 1 week, degeneration is mostly complete, and regeneration has already begun. Additionally, after degeneration completes, edema will decrease and be mostly gone by 6 weeks. Nerve regeneration in the rat leg is mostly complete by 6 weeks, although it may take up to 12 weeks for full function to be restored (Bendszus et al., 2004).

1.5 Basics of Diffusion-weighted MRI

1.5.1 Molecular Diffusion of Water

The diffusion of water is characterized by random or Brownian motion of water molecules. First proposed by Albert Einstein, there exists a relationship between the diffusion coefficient of a

liquid and the root-mean-squared displacement of molecules in the liquid during a given amount of time. This relationship, known as the Einstein equation for diffusion, is defined as:

$$x_{rms} = \sqrt{2Dt}, \quad [1.1]$$

where x_{rms} is the 1D root-mean-squared displacement, D is the diffusion coefficient in units of distance squared per time, and t is the diffusion time (Einstein, 1905). In an unrestricted medium, the diffusion of water molecules can also be described by a Gaussian probability density function $P(x, t)$:

$$P(x, t) = (4\pi Dt)^{-\frac{3}{2}} \exp\left(-\frac{x^2}{4Dt}\right). \quad [1.2]$$

However, when considering water diffusion in biological tissue, this does not hold true. Barriers such as organelles, cell membranes, macromolecules, and other cellular structures hinder water diffusion, causing a reduction in the apparent diffusion coefficient of water and a deviation from a pure Gaussian diffusion displacement probability density function (PDF) (Le Bihan et al., 1986). Because of this phenomenon, changes in the apparent water diffusion coefficient in biological tissues can provide insight into the underlying tissue microstructure.

1.5.2 Diffusion MRI Signal and PGSE

The idea of measuring water diffusion using nuclear magnetic resonance (NMR) existed long before the development of the modern MRI scanner. Through NMR experiments during the 1950s, it was discovered that the diffusion of water molecules in the presence of a magnetic field gradient (or spatially-varying magnetic field) causes a phase dispersion of the transverse

magnetization and a resulting attenuation of NMR signal (Carr and Purcell, 1954). Therefore, the same magnetic field gradients that are used for spatial encoding in conventional MRI experiments can also be used to indirectly measure the diffusion of water through signal attenuation or "diffusion weighting."

Although magnetic field gradients can be applied in a variety of different schemes to cause diffusion weighting of the signal, the most common method is the pulsed gradient spin-echo (PGSE) introduced by Stejskal and Tanner in 1965 (Stejskal and Tanner, 1965) shown in Fig. 1.2. This method utilizes two diffusion-weighting gradient pulses equal in area: the first

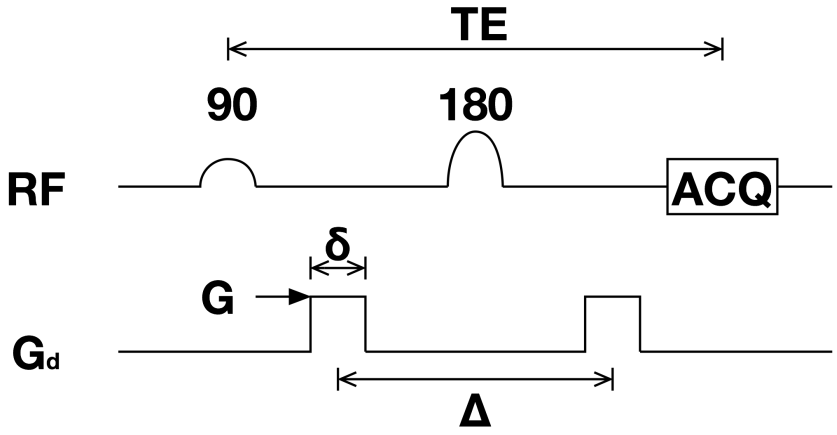

FIG. 1.2. PGSE pulse sequence. Similar to a conventional spin-echo pulse sequence, spins are excited by the 90-degree RF pulse, refocused by the 180-degree pulse, and the echo signal is acquired at the echo time, TE. Diffusion-weighting gradient pulses with amplitude G and duration δ are added on both sides of the 180-degree pulse, separated by a diffusion time Δ.

induces a spatially-dependent phase shift on the magnetic spins along the direction of the applied gradient and the second rewinds this shift. The diffusion of water molecules during the time between the two pulses along the same direction of the applied gradient pulses will cause a phase accumulation ϕ that is proportional to the displacement of the molecules:

$$\phi = \gamma \int_0^t \vec{G}(t')\vec{r}(t')dt', \quad [1.3]$$

where γ is the gyromagnetic ratio, $\vec{G}(t)$ is the magnetic field gradient and $\vec{r}(t)$ is the location of the magnetic spins. As noted earlier, in the case of unrestricted diffusion, the diffusion displacement of spins can be described by a Gaussian PDF. Due to the diffusing spins having different displacements, and therefore different phases, within a given voxel, the MRI signal will be attenuated and the attenuation will be related to the variance of the Gaussian phase PDF, $< \phi^2 >$:

$$S = S_0 \exp(-< \phi^2 >), \quad [1.4]$$

where S is the acquired signal and S_0 is the signal without diffusion weighting. The relationship between the signal and the diffusion coefficient D follows:

$$S = S_0 \exp\left(-D\gamma^2 \int_0^{TE} \left[\int_0^t G(t')dt'\right]^2\right) = S_0 \exp(-bD), \quad [1.5]$$

where

$$b = \gamma^2 \int_0^{TE} \left[\int_0^t G(t')dt'\right]^2. \quad [1.6]$$

b or the b-value is essentially the amount of diffusion weighting imparted by magnetic field gradients throughout the entire pulse sequence, although typically only gradients located between the diffusion gradient pulses are included in b-value calculations. Assuming rectangular diffusion

gradient lobes and negligible imaging and background gradients, the b-value for a PGSE pulse sequence is:

$$b = \gamma^2 G^2 \delta^2 (\Delta - \frac{\delta}{3}), \quad [1.7]$$

where G is the diffusion gradient amplitude, δ is the gradient duration, and Δ is the gradient separation or diffusion time.

From Eq. 1.5, it is apparent that the diffusion-weighted signal is a function of the b-value, which is pre-determined by the pulse sequence parameters G, δ, and Δ. Since b can be computed using the acquisition parameters, Eq. 1.5 contains two unknown variables: S_0 and D. Therefore, estimating S_0 and D requires at least two acquisitions with different b-values (conventionally one image without diffusion weighting or "b=0" and one with diffusion weighting). Although useful qualitative information may be gained through a single diffusion-weighted image (such as in ischemic stroke), most diffusion MRI applications include the quantitative measurement of D using the above method.

1.6 DWI Models

1.6.1 Diffusion Tensor Imaging

In biological tissue, not only do restrictions cause the diffusion displacement PDF to become non-Gaussian, but they also cause the apparent water diffusion to be anisotropic. This anisotropy is especially prominent in white matter and peripheral nerve where axons are aligned parallel to each other in bundles. Over diffusion times used in conventional DWI experiments, water inside

the axons moves further along the length of the axon than it does perpendicular to the axon. Axonal membranes and myelin act as barriers to the diffusion of water perpendicular to the axon, so if these axons are aligned with one another within a given imaging voxel, then the measured water diffusion will be highly anisotropic.

As previously noted, diffusion gradients sensitize the MRI signal to water diffusion along a single direction. Therefore, if water diffusion is anisotropic, then the measured diffusivity will change depending upon the direction. Generally, in white matter and peripheral nerve, this means that the measured diffusion coefficient will be greatest in the direction parallel to the axons within a given voxel. Determining the directional dependence of the diffusion of water could provide useful information regarding neural tissue microstructure and forms the basis of what is known as diffusion tensor imaging (DTI).

In order to appropriately quantify orientation-dependent water diffusion, a 3D Gaussian model of displacements is needed. As opposed to using a single scalar diffusion coefficient, a symmetric, rank-2 diffusion tensor **D** or DT is used to characterize the diffusion along each axis (x, y, and z) as well as correlations between the diffusion on each axis (xy, xz, and yz) (Basser et al., 1994):

$$\boldsymbol{D} = \begin{bmatrix} D_{xx} & D_{xy} & D_{xz} \\ D_{xy} & D_{yy} & D_{yz} \\ D_{xz} & D_{yz} & D_{zz} \end{bmatrix}. \quad [1.8]$$

Since the tensor is symmetric, there are a total of 6 unique elements. In order to estimate **D**, diffusion coefficients along at least 6 non-collinear, non-coplanar directions must be estimated. Taking into account that at least 2 b-values are needed to estimate each diffusion coefficient, the minimum number of acquisitions required for DTI is 7 (1 b=0 and non-zero b-value along 6

different directions). The number of images acquired may be much greater than this if more b-values are needed for a better estimate of each diffusion coefficient or if more directions are desired to provide a better estimate of **D**. One way to calculate **D** from the diffusion coefficients is through the equation:

$$D(\boldsymbol{n}) = \sum_{i,j=1}^{3} n_i n_j \boldsymbol{D}_{ij}, \qquad [1.9]$$

where $D(\boldsymbol{n})$ is the diffusion coefficient along a single direction and n_i is a normalized diffusion gradient component for each direction. **D** can also be estimated directly from the diffusion-weighted signal, rather than estimating the directional diffusivities first.

Once the diffusion tensor is estimated, it can be diagonalized so that rotationally invariant parameters can be calculated:

$$\boldsymbol{D} = \begin{bmatrix} \lambda_1 & & \\ & \lambda_2 & \\ & & \lambda_3 \end{bmatrix}, \qquad [1.10]$$

where λ_1, λ_2, and λ_3 are the eigenvalues with corresponding eigenvectors ε_1, ε_2, and ε_3. In a 3D sense, the rms diffusion displacement can be described by a diffusion ellipsoid. If the diffusion is isotropic, then the ellipsoid is spherical; if diffusion is anisotropic, then the ellipsoid will be prolate or oblate. The axes of the ellipsoid are aligned with the eigenvectors ε_1, ε_2, and ε_3 and the size of the ellipsoid corresponds with the eigenvalues λ_1, λ_2, and λ_3. By convention, the eigenvalues are sorted from highest to lowest so that λ_1, and accordingly ε_1, correspond to the principal direction of diffusion. In the case of white matter DTI, it is generally assumed that the direction described by ε_1 is parallel to the axons within each voxel, since it corresponds to the

direction of highest diffusion. This convention forms the basis of DTI tractography, in which nerve fibers are mapped out according to the direction of the principal eigenvector (Basser et al., 2000; Mori et al., 1999).

From the diffusion tensor eigenvalues, useful rotationally invariant DTI indices, including fractional anisotropy (FA) and mean, axial, and radial diffusivity (MD, AD, and RD, respectively) can be calculated. Mean diffusivity describes the average diffusion coefficient over all directions and can be calculated by taking the mean of the eigenvalues:

$$MD = (\lambda_1 + \lambda_2 + \lambda_3)/3. \quad [1.11]$$

Axial diffusivity is defined as diffusivity along the principal diffusion direction and radial diffusivity represents the average diffusivity along the other two axes:

$$AD = \lambda_1 \quad [1.12]$$

and

$$RD = (\lambda_2 + \lambda_3)/2. \quad [1.13]$$

Fractional anisotropy is a dimensionless metric ranging in value from 0 to 1 that characterizes the level of diffusion anisotropy present in a voxel, with 0 being completely isotropic and 1 being completely anisotropic (Basser, 1995):

$$FA = \sqrt{\frac{3}{2}}\frac{\sqrt{(\lambda_1 - MD)^2 + (\lambda_2 - MD)^2 + (\lambda_3 - MD)^2}}{\sqrt{\lambda_1^2 + \lambda_2^2 + \lambda_3^2}}. \quad [1.14]$$

Typically, FA is used as a measure of overall fiber integrity, AD is related to axon structure, and RD is linked to myelination, although other confounding factors can influence these measures (Jones et al., 2013; Song et al., 2003). Despite an inherent lack of specificity, combinations of FA, MD, AD, and RD are commonly used to evaluate white matter microstructure and have been shown to be sensitive to various pathologies.

1.6.2 Diffusion Kurtosis Imaging

1.6.2.1 Kurtosis and the DWI Signal

Kurtosis is a dimensionless statistical metric that characterizes the sharpness of a distribution compared to a Gaussian distribution (DeCarlo, 1997). The excess kurtosis K of a distribution is defined by the equation:

$$K = \frac{M_4}{M_2^2} - 3, \qquad [1.15]$$

where M_N is the nth moment of the distribution about its mean. For a purely Gaussian distribution, $K = 0$. A positive kurtosis (leptokurtic) means that the distribution is more peaked and has heavier tails compared with a Gaussian, whereas a negative kurtosis (platykurtic) means that the distribution is less peaked with less weight on its tails. Basically, the kurtosis can be used to characterize the non-Gaussianity of a distribution. Fig. 1.3 demonstrates how variations in kurtosis can affect the shape of a distribution. As described previously, in the case of unrestricted diffusion, the water diffusion displacement PDF is strictly Gaussian. However, in biological tissue, water diffusion is no longer unrestricted and the displacement PDF becomes non-Gaussian, with a water diffusion kurtosis greater than 0, or a more peaked distribution than

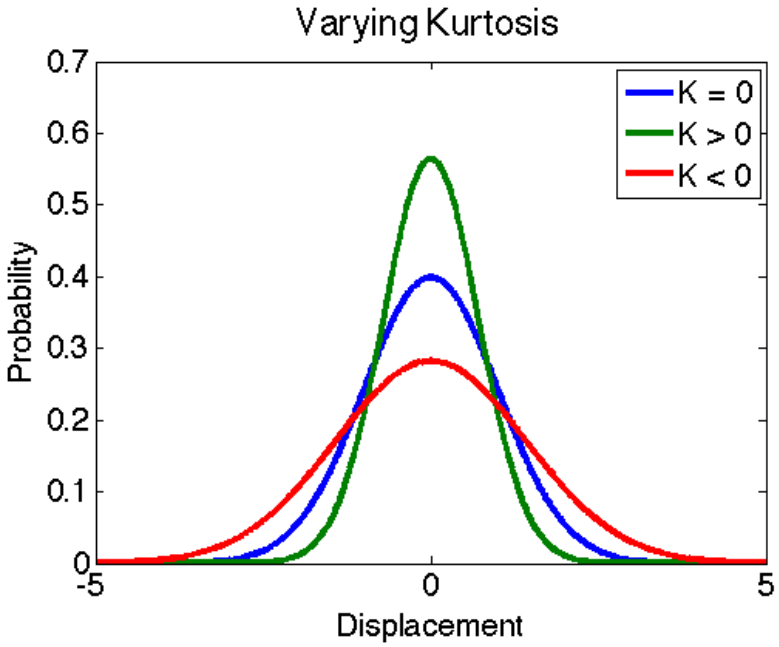

FIG 1.3. Distributions with different levels of kurtosis. Sample distributions are shown with K = 0 (blue), K < 0 (red), and K > 0 (green). The K = 0 distribution is a Gaussian distribution. The K < 0 distribution is platykurtic and less peaked than a Gaussian and the K > 0 distribution is leptokurtic and more peaked than a Gaussian. In biological tissue, K is almost always > 0 or more peaked than a Gaussian.

Gaussian. Measurement of the kurtosis of the water diffusion PDF could potentially provide useful information regarding the underlying tissue microstructure.

As stated before, Eq. 1.5 holds true in the case of unrestricted Gaussian diffusion. In biological tissue with its various compartments, membranes, etc., diffusion is restricted and Eq. 1.5 becomes an approximation:

$$S(b) \approx S_0 \exp(-bD), \qquad [1.16]$$

where $S(b)$ is now used to explicitly indicate that the acquired signal is a function of b. This equation can be re-written by taking the natural logarithm:

$$\ln[S(b)] \approx \ln(S_0) - bD. \qquad [1.17]$$

Defined by the cumulant expansion of the diffusion MRI signal (Frøhlich et al., 2006; Liu et al., 2004; Mitra and Sen, 1992; Tanner, 1978), an expanded form of Eq. 1.17 follows:

$$\ln [S(b)] \approx \ln (S_0) - bD + \frac{1}{6} b^2 D^2 K + O(b^3), \quad [1.18]$$

where K is the diffusion kurtosis coefficient. If the chosen b-values are small enough so that the $O(b^3)$ term is negligible, then Eq. 1.18 can be truncated:

$$\ln [S(b)] \approx \ln (S_0) - bD + \frac{1}{6} b^2 D^2 K. \quad [1.19]$$

Using this signal equation, the kurtosis of the water diffusion displacement PDF can be estimated from DWI acquisitions, known as diffusion kurtosis imaging (DKI). DKI is a clinically-applicable natural extension of DTI shown to provide additional sensitivity to tissue microstructure (Jensen et al., 2005). Since b is pre-determined by the gradient parameters and $S(b)$ is the acquired signal, there are three unknowns in Eq. 1.19: S_0, D, and K. Therefore, at least three total b-values are required in order to estimate D and K in a single direction.

1.6.2.2 Calculating the Kurtosis Tensor and Related Metrics

Similar to the anisotropic behavior of diffusivity in tissue, diffusion kurtosis has also been observed to be directionally dependent. However, instead of being described by a rank-2 tensor, the diffusion kurtosis tensor is a symmetric rank-4 tensor with 81 total components (3x3x3x3), 15 of which are unique. Therefore, without any assumptions, calculation of the kurtosis tensor requires measurements in at least 15 non-collinear, non-coplanar directions. The kurtosis tensor

(KT or **W**) can be estimated from directional diffusion and kurtosis coefficients using the equation (Jensen et al., 2005):

$$K(\boldsymbol{n}) = \frac{\overline{D}^2}{D(\boldsymbol{n})^2} \sum_{i,j,k,l=1}^{3} n_i n_j n_k n_l \, \boldsymbol{W}_{ijkl}, \qquad [1.20]$$

where $D(\boldsymbol{n})$ and $K(\boldsymbol{n})$ are the diffusion and kurtosis coefficients along a single direction, $\overline{D}$ (or MD) is the mean diffusivity, and n_i is a normalized diffusion gradient component for each direction. Only considering the 15 unique elements of the kurtosis tensor, Eq. 1.20 can be reduced to (Lu et al., 2006):

$$\begin{aligned} K(\boldsymbol{n}) = \frac{\overline{D}^2}{D(\boldsymbol{n})^2} [& n_1^4 \boldsymbol{W}_{1111} + n_2^4 \boldsymbol{W}_{2222} + n_3^4 \boldsymbol{W}_{3333} + 4(n_1^3 n_2 \boldsymbol{W}_{1112} + n_1^3 n_3 \boldsymbol{W}_{1113} \\ & + n_1 n_2^3 \boldsymbol{W}_{1222} + n_2^3 n_3 \boldsymbol{W}_{2223} + n_1 n_3^3 \boldsymbol{W}_{1333} + n_2 n_3^3 \boldsymbol{W}_{2333}) \\ & + 6(n_1^2 n_2^2 \boldsymbol{W}_{1122} + n_1^2 n_3^2 \boldsymbol{W}_{1133} + n_2^2 n_3^2 \boldsymbol{W}_{2233}) \\ & + 12(n_1^2 n_2 n_3 \boldsymbol{W}_{1123} + n_1 n_2^2 n_3 \boldsymbol{W}_{1223} + n_1 n_2 n_3^2 \boldsymbol{W}_{1233}). \end{aligned} \qquad [1.21]$$

Compared with the diffusion tensor, extracting useful measures from the kurtosis tensor is not necessarily as straightforward. However, one approach involves rotating the kurtosis tensor to the same reference frame as the diagonalized diffusion tensor:

$$\widetilde{\boldsymbol{W}}_{ijkl} = \sum_{i,j,k,l=1}^{3} R_{ii'} R_{jj'} R_{kk'} R_{ll'} \, \boldsymbol{W}_{i'j'k'l'}, \qquad [1.22]$$

where R_{ij} is the jth component of the DT eigenvector corresponding to the eigenvalue λ_i. From this, rotationally invariant metrics mean kurtosis (MK), axial kurtosis (AK), and radial kurtosis

(RK) can be extracted. Analogous to MD, MK is the diffusion kurtosis averaged over all gradient directions and can be calculated as (Tabesh et al., 2010):

$$MK = F_1(\lambda_1,\lambda_2,\lambda_3)\widetilde{\boldsymbol{W}}_{1111} + F_1(\lambda_2,\lambda_1,\lambda_3)\widetilde{\boldsymbol{W}}_{2222} + F_1(\lambda_3,\lambda_2,\lambda_1)\widetilde{\boldsymbol{W}}_{3333} + F_2(\lambda_1,\lambda_2,\lambda_3)\widetilde{\boldsymbol{W}}_{2233} + F_2(\lambda_2,\lambda_1,\lambda_3)\widetilde{\boldsymbol{W}}_{1133} + F_2(\lambda_3,\lambda_2,\lambda_1)\widetilde{\boldsymbol{W}}_{1122}, \quad [1.23]$$

where $\widetilde{\boldsymbol{W}}_{ijkl}$ are components of the rotated kurtosis tensor and

$$F_1(\lambda_1,\lambda_2,\lambda_3) \equiv \frac{(\lambda_1+\lambda_2+\lambda_3)^2}{18(\lambda_1-\lambda_2)(\lambda_1-\lambda_3)}\left[\frac{\sqrt{\lambda_2\lambda_3}}{\lambda_1}R_F\left(\frac{\lambda_1}{\lambda_2},\frac{\lambda_1}{\lambda_3},1\right) + \frac{3\lambda_1^2-\lambda_1\lambda_2-\lambda_1\lambda_3-\lambda_2\lambda_3}{3\lambda_1\sqrt{\lambda_2\lambda_3}}R_D\left(\frac{\lambda_1}{\lambda_2},\frac{\lambda_1}{\lambda_3},1\right)-1\right], \quad [1.24]$$

and

$$F_2(\lambda_1,\lambda_2,\lambda_3) \equiv \frac{(\lambda_1+\lambda_2+\lambda_3)^2}{3(\lambda_2-\lambda_3)^2}\left[\frac{\lambda_2+\lambda_3}{\sqrt{\lambda_2\lambda_3}}R_F\left(\frac{\lambda_1}{\lambda_2},\frac{\lambda_1}{\lambda_3},1\right) + \frac{2\lambda_1-\lambda_2-\lambda_3}{3\sqrt{\lambda_2\lambda_3}}R_D\left(\frac{\lambda_1}{\lambda_2},\frac{\lambda_1}{\lambda_3},1\right)-2\right], \quad [1.25]$$

where R_F and R_D represent Carlson's elliptic integrals (Carlson, 1979). Equation 1.23 is derived from the surface integral of the directional kurtoses across all directions. AK corresponds to the kurtosis along the principal diffusion direction (ε_1) and is given by:

$$AK = \frac{(\lambda_1+\lambda_2+\lambda_3)^2}{9\lambda_1^2}\widetilde{\boldsymbol{W}}_{1111}. \quad [1.26]$$

RK is the mean diffusion kurtosis across all directions orthogonal to the principal diffusion direction and can be calculated as:

$$RK = G_1(\lambda_1, \lambda_2, \lambda_3)\widetilde{\boldsymbol{W}}_{2222} + G_1(\lambda_1, \lambda_3, \lambda_2)\widetilde{\boldsymbol{W}}_{3333} + G_2(\lambda_1, \lambda_2, \lambda_3)\widetilde{\boldsymbol{W}}_{2233}, \quad [1.27]$$

where

$$G_1(\lambda_1, \lambda_2, \lambda_3) \equiv \frac{(\lambda_1 + \lambda_2 + \lambda_3)^2}{18\lambda_2(\lambda_2 - \lambda_3)^2}\left(2\lambda_2 + \frac{\lambda_3^2 - 3\lambda_2\lambda_3}{\sqrt{\lambda_2\lambda_3}}\right), \quad [1.28]$$

and

$$G_2(\lambda_1, \lambda_2, \lambda_3) \equiv \frac{(\lambda_1 + \lambda_2 + \lambda_3)^2}{3(\lambda_2 - \lambda_3)^2}\left(\frac{\lambda_2 + \lambda_3}{\sqrt{\lambda_2\lambda_3}} - 2\right). \quad [1.29]$$

Derivations of these equations are described in Tabesh et al. (Tabesh et al., 2010). Similar to DTI, AK is typically associated with axon structure and RK with myelination, although these metrics are not inherently specific. As shown above, the diffusion tensor is necessary for the calculation of the kurtosis tensor, therefore diffusion tensor metrics FA, MD, AD, and RD can also be determined.

1.6.2.3 Considerations for Diffusion Kurtosis Imaging Protocols

As previously described, DTI requires a minimum of 7 acquisitions: 1 b=0 image and 1 non-zero b-value for at least unique 6 directions. In most cases, more than 6 directions are used in order to obtain a more precise estimate of the diffusion tensor, and therefore, improve the precision of extracted indices such as FA. Additionally, choosing b-values suitable for the tissue being imaged and the applied DWI model is also important. If the non-zero b-value is too low, then the

variation in signal between the b=0 image and non-zero b-value image will be small and estimates of D will be more susceptible to noise. However, if the non-zero b-value is too high, then there will be greater contributions from the b^2 term (not accounted for in the DTI model) and the measured value of D will be biased. For *in vivo* brain DTI with D ≈ 1 $\mu m^2/ms$, the optimal b-value in order to maximize the precision and accuracy of the diffusion tensor is ≈ 1000 s/mm^2. A common *in vivo* brain DTI protocol includes at least 1 b=0 image and b = 1000 for 30 directions. With data collected along more than 6 directions, the diffusion tensor can be estimated using a least-squares approach.

Since DKI utilizes a higher order model than conventional DTI and is therefore more susceptible to noise, care must be taken in establishing an appropriate imaging protocol. As stated above, at higher b-values, the DTI approximation breaks down. In the DKI model however, higher b-values are necessary for a precise measurement of kurtosis, as its contribution to the DWI signal is dependent on b^2. Similar to the DTI model, if the maximum b-value is too high, then contributions from the b^3 term will become more significant and errors in the estimates of D and K will result. Fig. 1.4 shows the difference between fits based on the DTI and DKI signal equations for simulated data. If it is assumed that S(b) is a monotonically decreasing function (which is the case for biological tissue), then an upper bound for b can be obtained to ensure the validity of the DKI model (Lazar et al., 2008):

$$b \leq \frac{3}{DK}. \qquad [1.30]$$

For typical *in vivo* values in the brain of D ≈ 1 $\mu m^2/ms$ and K ≈ 1, the upper bound for b is 3000 s/mm^2. Empirical evidence suggests that the maximum b-value used for *in vivo* brain studies

should be between 2000 and 3000 s/mm^2 (Jensen and Helpern, 2010). If either D or K is different, such as in other regions of the body or in *ex vivo* tissue, then the b-values must be adjusted accordingly.

As previously indicated, estimation of the kurtosis tensor requires the sampling of a minimum of 15 directions and a minimum of two non-zero b-values per direction. In most cases, more than 15 directions are utilized to improve the precision of the kurtosis tensor. More than 2

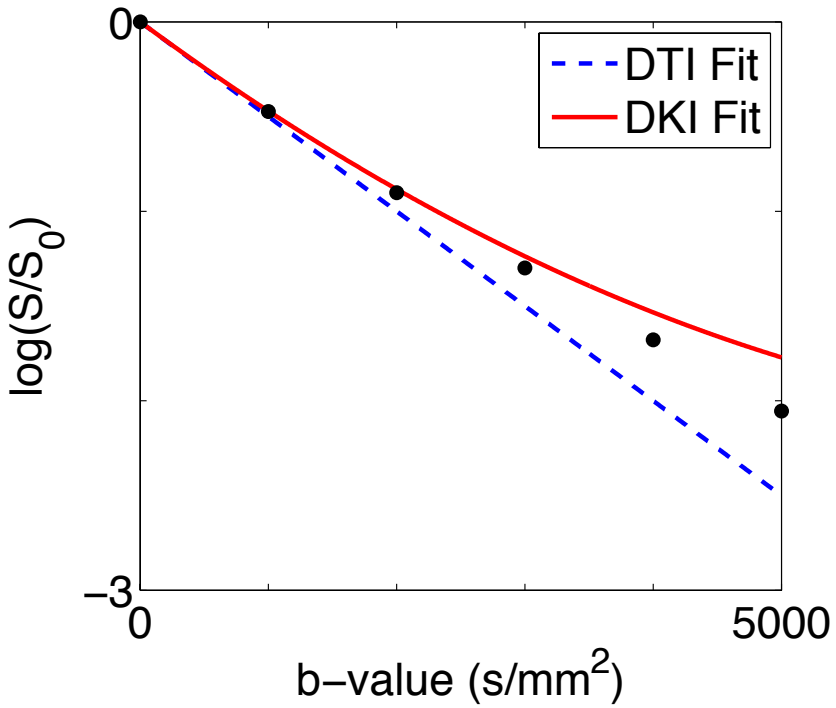

FIG 1.4. Comparison of signal fits for DTI and DKI models. Typical simulated in vivo data demonstrate the performance of the 1st and 2nd order signal models (or DTI and DKI models, respectively) as b-value increases. Notice that the DTI model performs well up to b-values of ≈ 1000 s/mm^2, but significantly worse as b-value increases. The DKI model performs better for b-values up to 2000-3000 s/mm^2.

non-zero b-values per direction may also be used to allow for assessment of goodness-of-fit as well as increased precision of D and K at the expense of much longer scan times. If more than 15

directions are sampled, the kurtosis tensor can be estimated using a least-squares method. A typical *in vivo* brain DKI protocol includes at least 1 b=0 image and b = 1000 and 2000 for 30 directions, for a total of 61 or more acquired images or volumes. As with most DWI methods, there are trade-offs between the number of directions, number of b-values, image resolution, and acquisition time that must be considered when forming a DKI protocol.

1.6.3 White Matter Tract Integrity Model

In recent years, in an attempt to improve specificity of DWI measurements to tissue components, a number of biophysical models of white matter have been proposed, including CHARMED (Assaf et al., 2004), AxCaliber (Assaf et al., 2008), ActiveAx (Alexander et al., 2010), and NODDI (Zhang et al., 2012). One of the more clinically-applicable models, termed the white matter tract integrity (WMTI) model, is based on the DKI framework and uses directional measurements of diffusivity and kurtosis to separate white matter into two compartments: the intra-axonal space and extra-axonal space (Fieremans et al., 2011). From this model, parameters including axonal water fraction (F_a), intra-axonal diffusivity (D_a), and axial and radial extra-axonal diffusivities ($D_{e,\parallel}$ and $D_{e,\perp}$) can be derived. Generally, previous studies have associated F_a with axon density, D_a and $D_{e,\parallel}$ with axon structure, and $D_{e,\perp}$ with myelination (Fieremans et al., 2013; Hui et al., 2012; Jelescu et al., 2016; Kelm et al., 2016). One primary assumption of the model is that axons within a given voxel are mostly oriented parallel to each other, limiting the application of WMTI to major white matter tracts with minimal presence of crossing fibers. Another assumption is that the intra- and extra-axonal compartments are non-exchanging and the signal from myelin is negligible, a reasonable assumption for the echo times used in most DWI experiments. Additionally, since WMTI uses the DKI framework, the DWI data requirements are

the same and can be acquired in clinically-relevant scan times. One advantage that WMTI has over other practical multi-compartment models of white matter (e.g. NODDI) is that it does not require any of the compartmental diffusivities to be fixed *a priori*.

Once the diffusion and kurtosis tensors are estimated, WMTI parameters can be computed. First, the axonal water fraction, F_a, is defined as:

$$F_a = \frac{K_{max}}{K_{max} + 3}, \quad [1.31]$$

where K_{max} is the maximum kurtosis over all directions derived from the kurtosis tensor. Then, compartmental diffusion coefficients for the intra- and extra-axonal spaces, $D_{a,i}$ and $D_{e,i}$ respectively, can be calculated as:

$$D_{a,i} = D_i \left[1 - \sqrt{\frac{K_i(1 - F_a)}{3F_a}} \right], \quad [1.32]$$

and

$$D_{e,i} = D_i \left[1 + \sqrt{\frac{K_i F_a}{3(1 - F_a)}} \right], \quad [1.33]$$

where D_i and K_i are the diffusion and kurtosis coefficients along the ith diffusion direction. Analogous to DTI, intra-axonal and extra-axonal diffusion tensors $\mathbf{D_a}$ and $\mathbf{D_e}$, respectively, can be computed from the corresponding diffusion coefficients. Using these compartmental diffusion tensors, WMTI metrics D_a, $D_{e,\parallel}$, and $D_{e,\perp}$ can be computed. D_a is defined as:

$$D_a = tr(\boldsymbol{D_a}), \quad [1.34]$$

where tr($\mathbf{D_a}$) is the trace of $\mathbf{D_a}$, and $D_{e,\|}$ and $D_{e,\perp}$ are calculated as:

$$D_{e,\|} = \lambda_{e,1}, \quad [1.35]$$

$$D_{e,\perp} = \frac{\lambda_{e,2} + \lambda_{e,3}}{2}, \quad [1.36]$$

where $\lambda_{e,1}$, $\lambda_{e,2}$, and $\lambda_{e,3}$ are the eigenvalues of $\mathbf{D_e}$ in descending order of size.

1.7 Diffusion-weighted Fast Spin-Echo

1.7.1 Conventional Fast Spin-Echo and the CPMG Conditions

Fast spin-echo (FSE) is an accelerated MRI sequence that utilizes an RF excitation pulse followed by multiple RF refocusing pulses to form multiple spin echoes (Hennig, 1988; Hennig et al., 1986). Using this method, multiple lines of k-space can be sampled after a single excitation, making it much faster than a conventional spin-echo acquisition with the acceleration determined by the length of the echo train. The potential length of the echo train is limited by T_2 relaxation of the transverse magnetization and the time between echoes or echo spacing (ESP). Although generally slower than other accelerated MRI sequences, such as echo-planar imaging (EPI) or gradient and spin-echo (GRASE), FSE is less sensitive to off-resonance effects and is therefore preferred for high-resolution imaging. However, as with most accelerated imaging sequences, FSE also comes with various artifacts, such as blurring and ghosting.

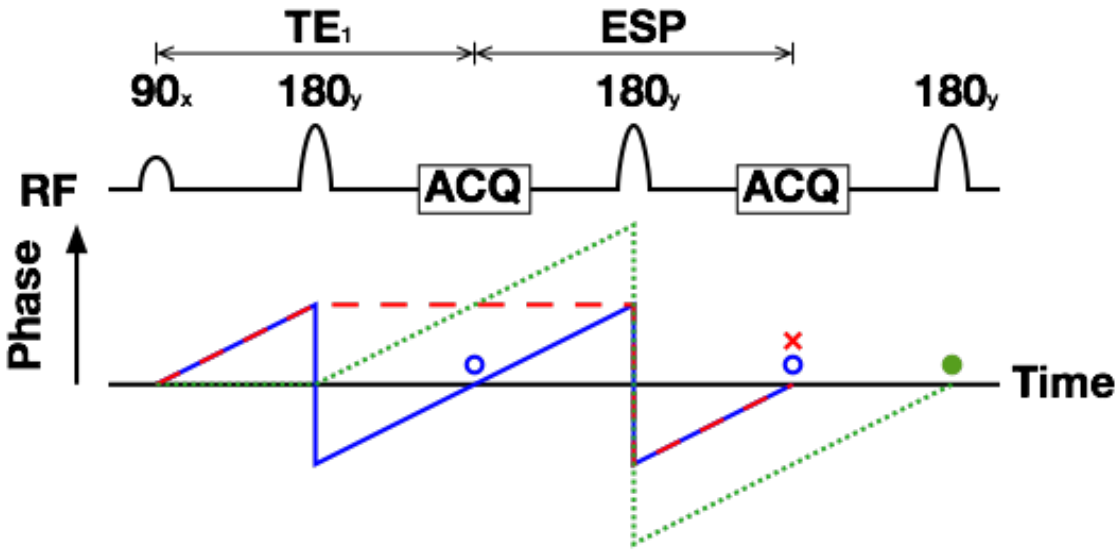

FIG 1.5. Signal coherence pathways of a typical fast spin-echo sequence. Primary spin-echo, stimulated echo, and secondary spin-echo pathways are represented by blue solid lines, red dashed lines, and green dotted lines, respectively. Temporal positions of primary spin echoes, stimulated echoes, and secondary spin echoes are denoted by blue circles, red x's, and green dots, respectively. In a CPMG fast spin-echo sequence, primary spin echoes and stimulated echoes will align temporally and have the same phase.

Imperfect excitation and refocusing pulses will produce echoes that are out of phase with each other, that when acquired, cause signal loss and ghosting artifacts. In pulse sequences with multiple refocusing pulses, there are three types of echoes generated: primary spin echoes, stimulated echoes, and secondary spin echoes. Primary spin echoes (or simply, spin echoes) consist of spins that are excited and then experience a phase reversal every refocusing pulse. Stimulated echo spins are excited to the transverse plane, stored on the longitudinal plane by an imperfect refocusing pulse, and re-excited by an additional imperfect refocusing pulse. Secondary spin echoes are formed from spins that are excited by imperfect refocusing pulses and then phase-reversed by subsequent refocusing pulses. Crusher gradients are conventionally utilized to cancel out secondary spin echoes, since they are typically out of phase with the

primary spin echoes. Figure 1.5 shows signal coherence pathways generated by a fast spin-echo pulse sequence.

To prevent signal loss and ghosting artifacts, echoes should occur at the desired time in the sequence and echoes that occur at the same time should have the same phase. A set of rules called the CPMG (Carr-Purcell-Meiboom-Gill) conditions (Carr and Purcell, 1954; Meiboom and Gill, 1958) ensures that this happens. The first condition is that the refocusing pulses should be 90° out of phase with the excitation pulse and be evenly spaced, meaning equal ESP throughout the echo train. The second condition is that the phase accumulated by a spin between consecutive refocusing pulses must be equal. This means that gradient pulses, such as crusher gradients and phase encoding gradients, must be equal in area on either side of the refocusing pulses, requiring phase encoding gradients to be rewound after each echo acquisition. If these two conditions are maintained, then the primary spin echoes and stimulated echoes coincide at the same time and have the same phase, minimizing signal loss and phase-induced artifacts.

1.7.2 DWI with non-CPMG Fast Spin-Echo

Due to the large amount of data acquired in typical diffusion-weighted scans, an accelerated sequence like FSE seems to be an optimal choice, yet combining DWI and FSE is not exactly trivial. There are two main problems with incorporating diffusion-weighting gradients into an FSE sequence. First, the pair of diffusion-weighting gradients surrounding the first refocusing pulse violates the CPMG conditions and will cause phase errors between the primary spin echoes and stimulated echoes. Second, inserting PGSE diffusion weighting greatly extends the minimum echo time of the first echo, so maintaining an equal ESP throughout the sequence would not be practical in most cases due to T_2 relaxation. Since diffusion-weighting

gradients inherently violate the CPMG conditions, other methods must be utilized for FSE to be suitable for diffusion-weighted imaging.

One solution to the problems that arise from diffusion-weighted FSE imaging is to mitigate contributions from the stimulated echoes and therefore minimize phase errors. This method still employs diffusion-weighting gradients straddling the first refocusing pulse, but also includes modulated crusher gradients to cancel out the signal from stimulated echoes (Beaulieu et al., 1993). Crusher gradient amplitudes must change with each refocusing pulse, otherwise stimulated echoes will be rephased by crusher gradients later in the echo train rather than being continually dephased. Using this technique, the CPMG conditions can be violated without introducing substantial artifacts or causing a major loss in signal. In this case, the pulse sequence is referred to as "non-CPMG fast spin-echo." Even though removal of the stimulated echoes results in a slight reduction in signal-to-noise ratio (SNR), the non-CPMG FSE sequence still maintains higher SNR efficiency than a conventional spin-echo sequence, as well as, allows for the collection of more data in a reduced scan time. Additionally, with cancellation of the stimulated echoes, the echo spacing can be shorter in duration than the first echo time as spin echoes and stimulated echoes no longer need to align in the temporal domain. Typically, in a diffusion-weighted FSE sequence, TE_1 (or TE in a centric phase-encoding scheme) will be much longer than ESP due to the inclusion of the diffusion-weighting gradients and diffusion time. With these modifications, diffusion-weighted FSE is a sequence especially useful for accelerated high-resolution diffusion-weighted imaging. Despite this, diffusion-weighted FSE has not seen widespread use, primarily due to increased sensitivity to motion artifacts compared with EPI. However, in studies conducted with *ex vivo* tissue at high field strength, as is the case for the

entirety of this work, motion is minimal and EPI distortions are aggravated, making diffusion-weighted FSE an optimal imaging solution.

1.8 Study Objectives

The purpose of this work is to evaluate and validate the DKI and WMTI models in a variety of animal models of neural tissue microstructure, since experimental assessment of these methods and histological validation have previously been limited. First, these models will be evaluated in adult hypomyelinated mouse brain. In order to accomplish this, protocols for 3D mouse brain DKI and EM histology measurement of axon and myelin morphology need to be established. After determining the relationship between DWI metrics and white matter microstructure in the hypomyelinated mouse brain, these methods will be applied to hypermyelinated mouse brain, with the expectation that DWI metrics will show changes opposing those observed in the hypomyelinated case. Next, these DWI methods will be evaluated in more complex models of normal and abnormal brain development in order to see whether the associations established in adult mice with abnormal myelination translate to other models of white matter microstructure. Finally, DKI and WMTI will be utilized to assess peripheral nerve injury and repair in rat sciatic nerve, neither of which have previously been applied to peripheral nerve imaging, in order to determine whether multi-compartment information from DWI can provide improved characterization of peripheral nerve injury.

1.9 References

Alexander, D.C., Hubbard, P.L., Hall, M.G., Moore, E.A., Ptito, M., Parker, G.J.M., Dyrby, T.B., 2010. Orientationally invariant indices of axon diameter and density from diffusion MRI. NeuroImage 52, 1374–1389. doi: 10.1016/j.neuroimage.2010.05.043

Assaf, Y., Blumenfeld-Katzir, T., Yovel, Y., Basser, P.J., 2008. AxCaliber: a method for measuring axon diameter distribution from diffusion MRI. Magn. Reson. Med. 59, 1347–1354. doi: 10.1002/mrm.21577

Assaf, Y., Freidlin, R.Z., Rohde, G.K., Basser, P.J., 2004. New modeling and experimental framework to characterize hindered and restricted water diffusion in brain white matter. Magn. Reson. Med. 52, 965–978.

Basser, P.J., 1995. Inferring microstructural features and the physiological state of tissues from diffusion-weighted images. NMR Biomed. 8, 333–344.

Basser, P.J., Mattiello, J., LeBihan, D., 1994. Estimation of the effective self-diffusion tensor from the NMR spin echo. J. Magn. Reson. Ser. B 103, 247–254.

Basser, P.J., Pajevic, S., Pierpaoli, C., Duda, J., Aldroubi, A., 2000. In vivo fiber tractography using DT-MRI data. Magn. Reson. Med. 44, 625–632.

Beaulieu, C.F., Zhou, X., Cofer, G.P., Johnson, G.A., 1993. Diffusion-weighted MR microscopy with fast spin-echo. Magn. Reson. Med. 30, 201–206.

Bendszus, M., Wessig, C., Solymosi, L., Reiners, K., Koltzenburg, M., 2004. MRI of peripheral nerve degeneration and regeneration: correlation with electrophysiology and histology. Exp. Neurol. 188, 171–177.

Carlson, B.C., 1979. Computing elliptic integrals by duplication. Numer. Math. 33, 1–16.

Carr, H.Y., Purcell, E.M., 1954. Effects of diffusion on free precession in nuclear magnetic resonance experiments. Phys. Rev. 94, 630.

Carson, R.P., Fu, C., Winzenburger, P., Ess, K.C., 2013. Deletion of Rictor in neural progenitor cells reveals contributions of mTORC2 signaling to tuberous sclerosis complex. Hum. Mol. Gen. 22, 140–152. doi: 10.1093/hmg/dds414

Carson, R.P., Kelm, N.D., West, K.L., Does, M.D., Fu, C., Weaver, G., McBrier, E., Parker, B., Grier, M.D., Ess, K.C., 2015. Hypomyelination following deletion of Tsc2 in oligodendrocyte precursors. Ann. Clin. Transl. Neurol. 12, 1041–1054. doi: 10.1002/acn3.254

Davis, K.L., Stewart, D.G., Friedman, J.I., Buchsbaum, M., Harvey, P.D., Hof, P.R., Buxbaum, J., Haroutunian, V., 2003. White matter changes in schizophrenia: evidence for myelin-related dysfunction. Arch. Gen. Psychiatry 60, 443–456. doi: 10.1001/archpsyc.60.5.443

DeCarlo, L.T., 1997. On the meaning and use of kurtosis. Psychol. Methods 2, 292.

Einstein, A., 1905. On the movement of small particles suspended in stationary liquids required by the molecular-kinetic theory of heat. Ann. Phys. (Berlin) 17, 16.

Faweett, J.W., Keynes, R.J., 1990. Peripheral nerve regeneration. Annu. Rev. Neurosci. 13, 43–60.

Fieremans, E., Benitez, A., Jensen, J.H., Falangola, M.F., Tabesh, A., Deardorff, R.L., Spampinato, M.V.S., Babb, J.S., Novikov, D.S., Ferris, S.H., Helpern, J.A., 2013. Novel white matter tract integrity metrics sensitive to Alzheimer disease progression. Am. J. Neuroradiol. 34, 2105–2112. doi: 10.3174/ajnr.A3553

Fieremans, E., Jensen, J.H., Helpern, J.A., 2011. White matter characterization with diffusional kurtosis imaging. NeuroImage 58, 177–188. doi: 10.1016/j.neuroimage.2011.06.006

Frøhlich, A.F., Østergaard, L., Kiselev, V.G., 2006. Effect of impermeable boundaries on diffusion-attenuated MR signal. J. Magn. Reson. 179, 223–233. doi: 10.1016/j.jmr.2005.12.005

Harrington, E.P., Zhao, C., Fancy, S.P.J., Kaing, S., Franklin, R.J.M., Rowitch, D.H., 2010. Oligodendrocyte PTEN is required for myelin and axonal integrity, not remyelination. Ann Neurol. 68, 703–716. doi:10.1002/ana.22090

Hennig, J., 1988. Multiecho imaging sequences with low refocusing flip angles. J. Magn. Reson. (1969) 78, 397–407.

Hennig, J., Nauerth, A., Friedburg, H., 1986. RARE imaging: a fast imaging method for clinical MR. Magn. Reson. Med. 3, 823–833.

Hui, E.S., Fieremans, E., Jensen, J.H., Tabesh, A., Feng, W., Bonilha, L., Spampinato, M.V., Adams, R., Helpern, J.A., 2012. Stroke assessment with diffusional kurtosis imaging. Stroke 43, 2968–2973. doi: 10.1161/STROKEAHA.112.657742

Hursh, J.B., 1939. Conduction velocity and diameter of nerve fibers. Am. J. Physiol. 127, 131–139.

Jelescu, I.O., Zurek, M., Winters, K.V., Veraart, J., Rajaratnam, A., Kim, N.S., Babb, J.S., Shepherd, T.M., Novikov, D.S., Kim, S.G., Fieremans, E., 2016. In vivo quantification of demyelination and recovery using compartment-specific diffusion MRI metrics validated by electron microscopy. NeuroImage 132, 104–114. doi: 10.1016/j.neuroimage.2016.02.004

Jensen, J.H., Helpern, J.A., 2010. MRI quantification of non-Gaussian water diffusion by kurtosis analysis. NMR Biomed. 23, 698–710. doi: 10.1002/nbm.1518

Jensen, J.H., Helpern, J.A., Ramani, A., Lu, H., Kaczynski, K., 2005. Diffusional kurtosis imaging: the quantification of non-gaussian water diffusion by means of magnetic resonance imaging. Magn. Reson. Med. 53, 1432–1440. doi: 10.1002/mrm.20508

Jones, D.K., Knösche, T.R., Turner, R., 2013. White matter integrity, fiber count, and other

fallacies: The do's and don'ts of diffusion MRI. NeuroImage 73, 239–254. doi: 10.1016/j.neuroimage.2012.06.081

Kelm, N.D., West, K.L., Carson, R.P., Gochberg, D.F., Ess, K.C., Does, M.D., 2016. Evaluation of diffusion kurtosis imaging in ex vivo hypomyelinated mouse brains. NeuroImage 124, 612–626. doi: 10.1016/j.neuroimage.2015.09.028

Kutzelnigg, A., 2005. Cortical demyelination and diffuse white matter injury in multiple sclerosis. Brain 128, 2705–2712. doi: 10.1093/brain/awh641

LaSarge, C.L., Danzer, S.C., 2014. Mechanisms regulating neuronal excitability and seizure development following mTOR pathway hyperactivation. Front. Mol. Neurosci. 7, 18.

Lazar, M., Jensen, J.H., Xuan, L., Helpern, J.A., 2008. Estimation of the orientation distribution function from diffusional kurtosis imaging. Magn. Reson. Med. 60, 774–781. doi: 10.1002/mrm.21725

Le Bihan, D., Breton, E., Lallemand, D., Grenier, P., Cabanis, E., Laval-Jeantet, M., 1986. MR imaging of intravoxel incoherent motions: application to diffusion and perfusion in neurologic disorders. Radiology 161, 401–407.

Liu, C., Bammer, R., Acar, B., Moseley, M.E., 2004. Characterizing non-gaussian diffusion by using generalized diffusion tensors. Magn. Reson. Med. 51, 924–937. doi: 10.1002/mrm.20071

Lu, H., Jensen, J.H., Ramani, A., Helpern, J.A., 2006. Three-dimensional characterization of non-gaussian water diffusion in humans using diffusion kurtosis imaging. NMR Biomed. 19, 236–247. doi: 10.1002/nbm.1020

Meiboom, S., Gill, D., 1958. Modified spin-echo method for measuring nuclear relaxation times. Rev. Sci. Instrum. 29, 688. doi: 10.1063/1.1716296

Mitra, P.P., Sen, P.N., 1992. Effects of microgeometry and surface relaxation on NMR pulsed-field-gradient experiments: simple pore geometries. Phys. Rev. B 45, 143.

Mori, S., Crain, B.J., Chacko, V.P., van Zijl, P.C.M., 1999. Three-dimensional tracking of axonal projections in the brain by magnetic resonance imaging. Ann. Neurol. 45, 265–269. doi: 10.1002/1531-8249(199902)45:2<265::AID-ANA21>3.0.CO;2-3

Peters, J.M., Sahin, M., Vogel-Farley, V.K., Jeste, S.S., Nelson, C.A., Gregas, M.C., Prabhu, S.P., Scherrer, B., Warfield, S.K., 2012. Loss of white matter microstructural integrity is associated with adverse neurological outcome in tuberous sclerosis complex. Acad. Radiol. 19, 17–25.

Song, S.-K., Sun, S.-W., Ju, W.-K., Lin, S.-J., Cross, A.H., Neufeld, A.H., 2003. Diffusion tensor imaging detects and differentiates axon and myelin degeneration in mouse optic nerve

after retinal ischemia. NeuroImage 20, 1714–1722. doi: 10.1016/j.neuroimage.2003.07.005

Stejskal, E.O., Tanner, J.E., 1965. Spin diffusion measurements: spin echoes in the presence of a time-dependent field gradient. J. Chem. Phys. 42, 288. doi: 10.1063/1.1695690

Tabesh, A., Jensen, J.H., Ardekani, B.A., Helpern, J.A., 2010. Estimation of tensors and tensor-derived measures in diffusional kurtosis imaging. Magn. Reson. Med. 65, 823–836. doi: 10.1002/mrm.22655

Tanner, J.E., 1978. Transient diffusion in a system partitioned by permeable barriers. Application to NMR measurements with a pulsed field gradient. J. Chem. Phys. 69, 1748. doi: 10.1063/1.436751

Waller, A., 1850. Experiments on the section of the glossopharyngeal and hypoglossal nerves of the frog, and observations of the alterations produced thereby in the structure of their primitive fibres. Philos. Trans. R. Soc. Lond. 140, 423–429.

Waxman, S.G., 1980. Determinants of conduction velocity in myelinated nerve fibers. Muscle Nerve 3, 141–150. doi: 10.1002/mus.880030207

Zhang, H., Schneider, T., Wheeler-Kingshott, C.A., Alexander, D.C., 2012. NODDI: practical in vivo neurite orientation dispersion and density imaging of the human brain. NeuroImage 61, 1000–1016.

CHAPTER 2

METHODS

This chapter provides a detailed description of the methods used for this entire work. Any alterations to these methods or any other procedures specific to each study are stated in the Materials and Methods section of each chapter (Chapters 3-6).

2.1 Mouse Brain

2.1.1 Animal Preparation

All animal studies were completed with the approval of the Vanderbilt University Institutional Animal Care and Use Committee. *Rictor* Olig2-Cre CKO (Rictor), *Tsc2* Olig2-Cre CKO (TSC), and *Pten* Olig2-Cre CKO (PTEN) mice were the product of crosses between *Rictor, Tsc2*, or *Pten* homozygous floxed animals with *Rictor, Tsc2*, or *Pten* floxed heterozygous; Olig2-Cre hemizygous mice. The resultant CKO genotypes were then: $Rictor^{F/F}$;Olig2-Cre, $Tsc2^{F/F}$;Olig2-Cre, or $Pten^{F/F}$;Olig2-Cre. Control, Rictor, TSC, and PTEN mice were euthanized and transcardially perfusion-fixed with 2.5% glutaraldehyde and 2% paraformaldehyde + 1mM Gd-DTPA (Magnevist, Bayer HealthCare, Wayne, NJ, USA) in phosphate-buffered saline (PBS) (Johnson et al., 2002; Karnovsky, 1965). Mouse brains were immediately excised and post-fixed in the fixative solution at 4°C for a period of 1 week to allow for complete penetration of the fixative. Then, mouse brains were placed in PBS + 1mM Gd-DTPA + 0.01% sodium azide at 4°C for at least 1 week before imaging, with the solution changed out a minimum of 3 times, in

order to wash out residual fixative that reduces the tissue T_2 and image SNR and ensure a uniform distribution of Gd-DTPA throughout the brain (Shepherd et al., 2009). The addition of 1 mM Gd-DTPA lowered the T_1 of mouse brain to ≈ 400 ms at 15.2T, increasing the SNR efficiency of the MRI acquisition. Although Gd-DTPA remains extracellular for *in vivo* experiments, previous studies have indicated that Gd-DTPA affects both the intra- and extracellular compartments in fixed *ex vivo* tissue, and that it has a similar effect on the T_2 of both the myelin water and intra/extra-axonal water pools (Dortch et al., 2010; Purea and Webb, 2006). For MR imaging, mouse brains were placed in MR-compatible plastic tubes filled with a perfluoropolyether liquid (Fomblin, Solvay Solexis, Thorofare, NJ, USA) for susceptibility matching, tissue hydration, and minimal background signal.

2.1.2 MRI

Ex vivo mouse brain imaging was performed at bore temperature (17±0.5 ºC) on a 15.2T 11-cm horizontal bore Bruker Biospec scanner (Bruker BioSpin, Billerica, MA, USA) using a Bruker 35-mm quadrature volume coil for RF transmission and reception. All three MRI protocols, DWI, MET_2, and qMT, were acquired in a single session with field of view (FOV) = 19.2 x 14.4 x 10.8 mm^3 and matrix size = 128 x 96 x 72 for a nominal isotropic resolution of 150 x 150 x 150 μm^3 in a total overall scan time of ≈ 24 hr.

2.1.2.1 Diffusion-weighted Imaging

Diffusion-weighted imaging data were acquired using a 3D diffusion-weighted fast spin-echo sequence with repetition time (TR) = 260 ms, echo time (TE) = 19.0 ms, echo spacing (ESP) = 7.1 ms, echo train length (ETL) = 4, number of excitations (NEX) = 1, and centric phase encoding (Beaulieu et al., 1993). The excitation and refocusing pulses were non-selective hard

pulses with durations of 125 and 250 μs, respectively, and the receiver bandwidth (BW) for signal acquisition = 75 kHz. Diffusion weighting was implemented using a pulsed gradient spin echo preparation with gradient pulse duration (δ) = 5 ms, diffusion time (Δ) = 12 ms, prescribed b-values = 3000, 6000, and 9000 s/mm^2, and 90 unique directions (30 per b-shell) optimized for a multi-shell acquisition (Caruyer et al., 2013). Six b=0 images were collected (evenly spaced throughout the scan duration) and averaged. For each brain, 96 3D volumes were collected in a total scan time of ≈ 12 hr.

2.1.2.2 Multi-exponential T_2

MET$_2$ data were acquired using a 3D multiple spin-echo sequence with TR = 520 ms, TE = 5.8 ms, 18 evenly spaced echoes with ESP = 5.8 ms, BW = 75 kHz, and NEX = 8 in a total scan time of ≈ 8 hr. For excitation and refocusing, non-selective hard pulses were utilized with durations of 160 and 100 μs, respectively. Crusher gradient pairs with amplitudes = 6 G/cm and durations = 428 μs surrounded each refocusing pulse. With the assumption that secondary echoes not excited by the excitation pulse were removed, the observed echo magnitudes were related to proton density and T_2 using the extended phase graph (EPG) algorithm (Hennig, 1991; Lebel and Wilman, 2010; Prasloski et al., 2012).

2.1.2.3 Quantitative Magnetization Transfer

qMT data were acquired using a 3D selective inversion-recovery prepared fast spin-echo sequence (Gochberg and Gore, 2007) with ETL = 8, ESP = 5 ms, and centric phase encoding. A 1-ms hard inversion preparation pulse was used to selectively invert the free water pool, while macromolecular spins remained mostly unaffected. The acquisition was repeated for 15 inversion times (TI) log-spaced from 3.5 to 2000 ms with a constant pre-delay (T_d) of 590 ms, resulting in a total scan time of ≈ 3.5 hr.

2.1.3 MRI Data Analysis

Image data were analyzed using in-house written code in MATLAB (Mathworks, Natick, MA, USA). For all analyses, 3D k-space data were zero-padded 2x in each direction before reconstruction, resulting in a working isotropic image resolution of 75 μm. DTI analysis was performed by first estimating diffusion tensors voxel-wise using a linear least squares approach and then calculating the DTI indices FA, MD, AD, and RD from these tensors. Since data acquired with too high of b-value can bias DTI metrics, only the b = 3000 s/mm^2 shell was used for DTI analysis. For DKI analysis, diffusion and kurtosis tensors were estimated voxel-wise using a constrained linear least-squares method (Tabesh et al., 2010) and DKI indices MK, AK, and RK were calculated. Using the kurtosis tensor, WMTI analysis was performed on a voxel-wise basis and WMTI metrics F_a, D_a, $D_{e,\parallel}$, and $D_{e,\perp}$ were computed (Fieremans et al., 2011). DWI data collected for the hypomyelination study, which included all adult control, Rictor, and TSC mice (see Chapter 3), only used b-values of 3000 and 6000 s/mm^2. Therefore, in order to make direct comparisons to these groups in other studies, DWI data with b = 9000 s/mm^2 were excluded from all analyses, since use of the higher b-value was observed to systematically alter both DKI and WMTI parameter values.

The MET$_2$ analysis was performed using the freely available multi-exponential relaxation analysis (MERA) toolbox for MATLAB (vuiis.vanderbilt.edu/~doesmd/MERA/MERA_Toolbox.html). Echo magnitudes from each image voxel were fitted via a conventional linear inverse approach (Whittall and MacKay, 1989) by non-negative least-squares (NNLS) (Lawson and Hanson, 1974) to the sum of signals from 100 logarithmically spaced T_2 components, as defined by the EPG algorithm and spanning TE/2 to 500 ms in the T_2 domain, similar to previous work (Prasloski et al., 2012). The spectra were

regularized using a minimum curvature constraint with a constant conservative regularization (μ = 0.002) across all voxels. For each voxel, the MWF was defined as the fraction of signal with T_2 < 17 ms, with the threshold empirically determined for this work. For qMT analysis, the 15 signal magnitudes acquired with varying TI were fitted voxel-wise to a five-parameter biexponential model as described previously (Gochberg and Gore, 2007), from which the ratio of macromolecular to free pool magnetization, or PSR, was calculated.

2.1.4 Histology

2.1.4.1 Tissue Preparation

After MRI was completed, a subset of mouse brains was sectioned for histology. Following a mid-sagittal cut, four sections of tissue each containing a desired white matter region of interest (ROI), the midbody of the corpus callosum (MidCC), genu (GCC), splenium (SCC), and anterior commissure (AC), were sectioned in the sagittal plane, as shown in Fig. 2.1a, and processed for EM at the Vanderbilt Cell Imaging Shared Resource - Research Electron Microscopy facility. Tissue sections were placed in osmium tetroxide in cacodylate buffer (1% for 1 hr, then 0.5% for 12 hr) and dehydrated in graded ethanol. Then, tissue sections were embedded in epoxy resin and 1 μm thick sections were cut and stained with 1% toluidine blue. From light microscopy images of the thick sections, a 500 x 500 μm^2 ROI was manually selected for each tissue block, as indicated in Fig. 2.1b, with the aid of a standard mouse brain atlas (Paxinos and Franklin, 2004) and 70 nm ultra-thin sections were cut from the ROI for EM. The MidCC ROI was chosen as the portion of the corpus callosum just superior to the section of the fornix where its fibers bend to travel inferiorly from the corpus callosum (Bregma -0.7 mm). The GCC and SCC ROIs were selected as the most anterior (Bregma 1 mm) and posterior (Bregma -2.5 mm) sections of the

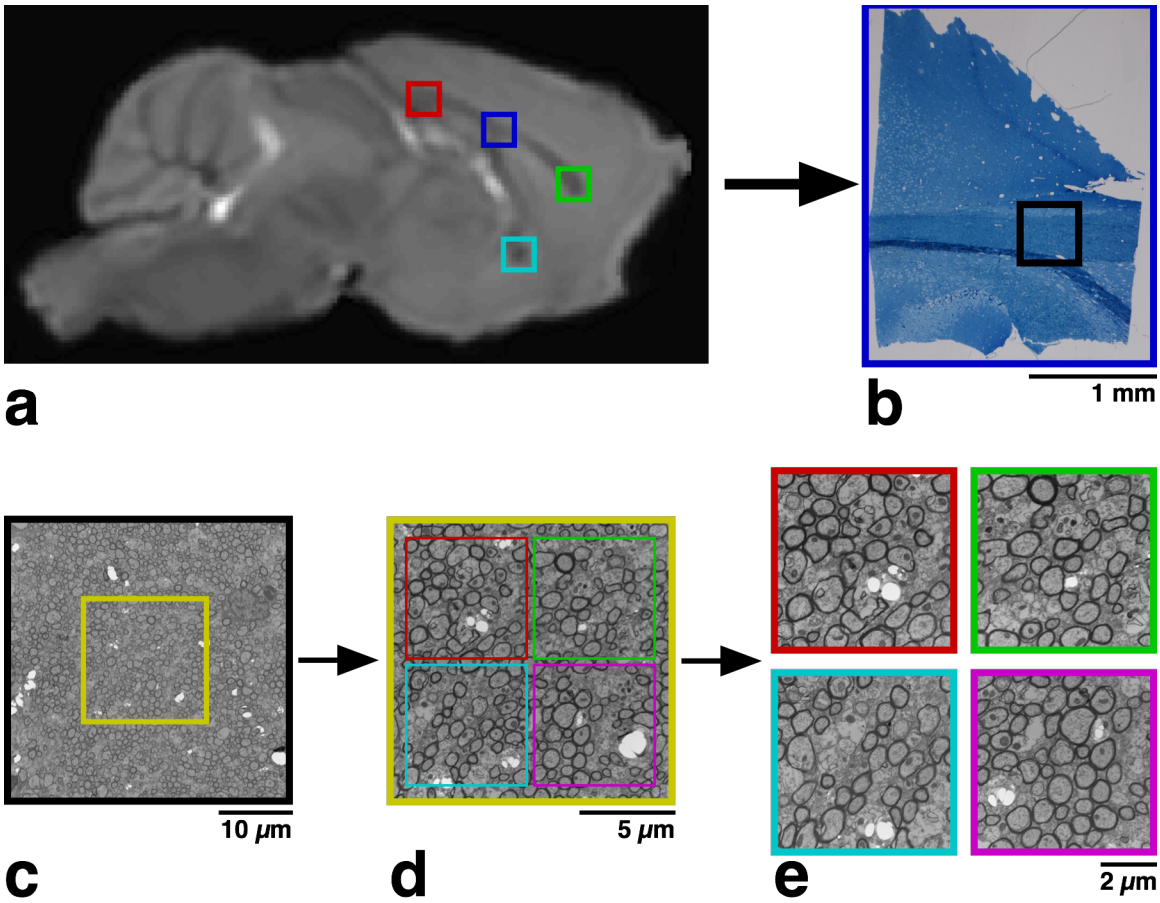

FIG. 2.1. EM sampling of white matter ROIs. (a) T_2-weighted sagittal cross-section showing the locations of the histology sections. (b) 1 µm thick section of the midbody of the corpus callosum stained with toluidine blue. The black box shows the location of the MidCC EM thin section. (c) 2700x EM image of the MidCC in a normal mouse brain. ~4 of these images were acquired for each histology section. (d) 6500x EM image used for axon density measurements. Colored boxes show locations of four 15000x images acquired for each 6500x image. (e) 15000x EM images used for measuring myelin fraction, axon fraction, axon diameter, myelin thickness, and g-ratio.

corpus callosum, respectively. The AC ROI encompassed the entirety of the anterior commissural tract crossing through the mid-sagittal plane and was located just anterior to the fornix at Bregma 0.2 mm.

2.1.4.2 Transmission Electron Microscopy

EM images of ultra-thin sections were collected with an FEI Tecnai T12 electron microscope (FEI, Hillsboro, OR, USA) at various magnifications. From these images, measurements of axon

diameter (inside the myelin) (d_a), myelin thickness (z_m), g-ratio (g), axon density (ρ_a), histologic myelin fraction (f_m), and histologic axon fraction (f_a) were performed in MATLAB (Mathworks, Natick, MA, USA). For improved clarity, histology measures are identified by lowercase variables and MR-derived metrics are reported as upper-case variables or acronyms.

Using images collected at 6500x (≈ 4 per white matter tract, Fig. 2.1d), axon density was measured by manual counting the number of myelinated axons within the given FOV. The other histology metrics were computed from 15000x images acquired from the same area as each 6500x image (4 per 6500x image or ≈ 16 total per brain, Fig. 2.1e). First, a local Otsu threshold was applied to distinguish between myelin (white) and non-myelin (black) pixels (Fig. 2.2b). Using this binary image, myelinated axons (≈ 300 per histology section, fewer for TSC mice due to much lower axon density) were manually selected and image pixels erroneously identified as myelin (e.g. intra-axonal mitochondria) were corrected. Next, using the manually defined seed

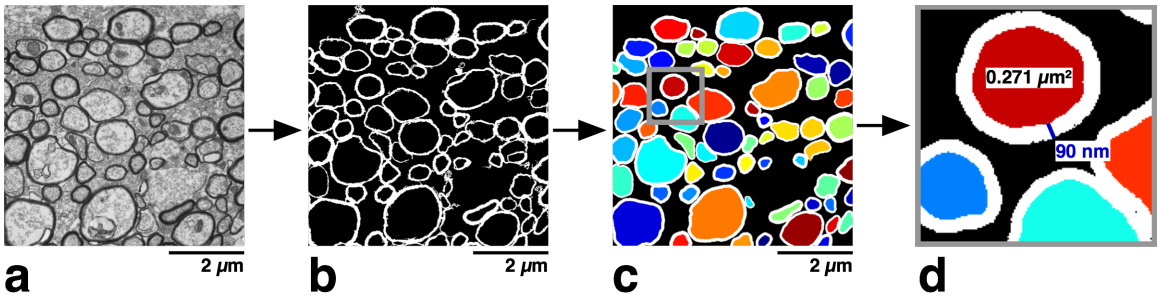

FIG. 2.2. EM histology processing. (a) Typical 15000x EM image of an adult mouse midbody of the corpus callosum. (b) EM image after segmentation with myelin pixels shown in white. (c) EM image showing axons after processing is performed to derive axon area, axon diameter, and myelin thickness. Axon color is randomized to indicate that each axon is measured independently. (d) Typical axon area and myelin thickness measurements.

point for each individual axon, an active contour algorithm (Kass et al., 1988) was implemented to determine the intra-axonal area for each (Fig. 2.2c). From these measures of axon area, axon diameter was computed for each axon assuming circular geometry and axon fraction was

determined by summing the cross-sectional areas of all myelinated axons. In order to maintain consistency with the axonal water fraction derived from WMTI (which excludes myelin), histologic axon fraction was adjusted to exclude contributions from myelin to the overall area (division by 1-f_m).

Since the local Otsu threshold failed to produce a uniform myelin thickness surrounding the axon, the myelin of each axon was independently segmented on the original EM image. Using the previously-derived axon boundary as the initial contour, each contour was expanded along its normal lines until they reached a pixel intensity greater than the average pixel intensity along the initial contour (i.e. the axon/myelin boundary). Lines that grew into the myelin of adjacent axons were rejected if: i) the line terminated within another axon boundary, or ii) the length was greater than 3 times the median absolute deviation (Leys et al., 2013). Myelin thickness was calculated as the median length of the remaining lines and the per-axon myelin area was computed by growing the initial contour a uniform distance equal to the myelin thickness. Myelin fraction was then determined by summing the per-axon myelin areas. Finally, the g-ratio was calculated as the ratio between the inner and outer diameter of each myelinated axon or $g = \frac{d_a}{d_a+2z_m}$. It is important to note that per-axon metrics were restricted to axons lying fully within the FOV, but axon and myelin fraction also included axons that were only partially visible.

For group analysis of histological measures, the mean and standard error of each measure was taken across all analyzed EM images for each group (15000x for d_a, z_m, g, f_m, and f_a, 6500x for ρ_a). For a conservative estimate of error, the standard error was based on the number of different brains in the group as opposed to the number of images used. Histological measures were then compared between the control and CKO groups using a Wilcoxon rank-sum test.

2.2 Rat Sciatic Nerve

2.2.1 Nerve Preparation

All animal studies were completed with the approval of the Vanderbilt University Institutional Animal Care and Use Committee. With adult female Sprague-Dawley rats anesthetized by 2% isoflurane inhalation, the left sciatic nerve was exposed, completely transected with microsurgical scissors, and then immediately repaired by suturing the epineurium of the proximal and distal nerve segments. Then, at various time points after surgery, animals were euthanized and sciatic nerves were immediately excised, straightened on a wooden dowel, and fixed in 4% glutaraldehyde and 0.5% paraformaldehyde in phosphate-buffered saline (PBS) at 4°C for a minimum of 24 hr. After fixation, nerves were placed in PBS + 1mM Gd-DTPA + 0.01% sodium azide at 4°C for at least 48 hr before imaging, with the solution changed out at least once, in order to wash out residual fixative (Shepherd et al., 2009). For imaging, nerves were trimmed to ≈ 14 mm in length, with the injury site centered, and placed in glass capillary tubes (2-mm outer diameter) filled with a perfluoropolyether liquid (Fomblin, Solvay Solexis, Thorofare, NJ, USA) for susceptibility matching, tissue hydration, and minimal background signal. For higher throughput, 6 nerves in a hexagonal arrangement were imaged simultaneously. Figure 2.3 shows a representative injured nerve and a T2-weighted image of 6 excised sciatic nerves in the transverse plane.

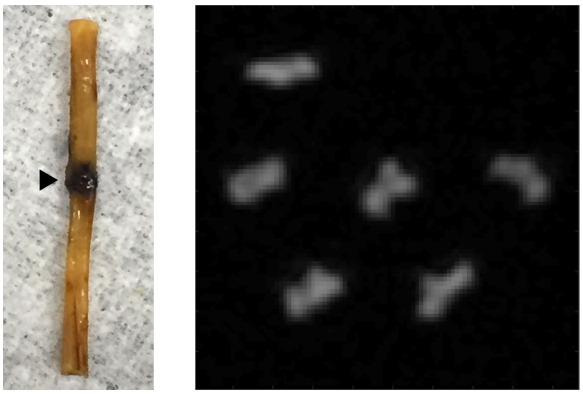

FIG. 2.3. Excised sciatic nerve imaging. (Left) Representative injured sciatic nerve with injury site indicated by a black arrow. (Right) T_2-weighted image of 6 sciatic nerves in the transverse plane, demonstrating the MR imaging setup.

2.2.2 MRI

Ex vivo sciatic nerve imaging was performed at bore temperature (17±0.5 ºC) on a 15.2T 11-cm horizontal bore Bruker Biospec scanner (Bruker BioSpin, Billerica, MA, USA) using a Bruker 35-mm quadrature volume coil for RF transmission and reception. DWI data were acquired using a 3D diffusion-weighted fast spin-echo sequence (Beaulieu et al., 1993) with TR = 595 ms, TE = 14.2 ms, ESP = 4.2 ms, ETL = 4, centric phase encoding, FOV = 16 x 6.4 x 6.4 mm^3 and matrix size = 48 x 48 x 48 for a resolution of 333 x 133 x 133 μm^3 (333 μm along the length of the nerve, 133 μm transverse to the nerve). The excitation and refocusing pulses were non-selective hard pulses with durations of 160 and 100 μs, respectively, and the receiver bandwidth for signal acquisition = 50 kHz. Diffusion weighting was performed using a pulsed gradient spin echo preparation with δ = 4.5 ms, Δ = 7.5 ms, prescribed b-values = 2000 and 5000 s/mm^2, 30 unique directions (15 per b-shell) optimized for a multi-shell acquisition (Caruyer et al., 2013), and NEX = 4 with gradient polarity reversal to mitigate background gradient cross-terms (Neeman et al., 1991). Three b=0 images, spaced evenly throughout the scan duration, were collected and averaged. For each nerve scan, 33 3D volumes were collected in a total scan time of ≈ 12 hr.

2.2.3 DWI Processing

Image data were analyzed using in-house written code in MATLAB (Mathworks, Natick, MA, USA). For all analyses, 3D k-space data were zero-padded 2x in each direction before reconstruction, resulting in a working image resolution of 167 x 67 x 67 μm^3. Additionally, a Gaussian smoothing filter with $\sigma = 1$ was applied to each volume. DTI analysis was performed by estimating diffusion tensors voxel-wise using a linear least squares approach and then calculating the DTI indices FA, MD, AD, and RD from these tensors. Since data acquired with too high of b-value can cause systematic errors in DTI metrics, only the b = 2000 s/mm^2 shell was used for DTI analysis. For DKI analysis, diffusion and kurtosis tensors were estimated voxel-wise using an iterative constrained weighted linear least-squares method (Tabesh et al., 2010; Veraart et al., 2013) and DKI indices MK, AK, and RK were calculated. Using the kurtosis tensor, WMTI analysis was performed on a voxel-wise basis and WMTI metrics F_a, D_a, $D_{e,\parallel}$, and $D_{e,\perp}$ were computed (Fieremans et al., 2011). In voxels where estimation of the kurtosis tensor was poor, defined as a minimum of 3 directions that violated the minimum directional kurtosis constraint, a median filter with a 3x3x3 voxel window was applied to all parameter maps for the purpose of outlier removal.

2.2.4 Group ROI Analysis

For group analysis, ROIs were manually delineated for each nerve on transverse cross-sections at the injury site, and 3 mm proximal and distal to the injury site. Additionally, a control group was formed across all injured nerves using ROIs located 5 mm proximal to the injury site, since nerve that is far proximal to the injury site is minimally affected and simulates normal nerve. Then,

ROI means of DWI parameters were computed for each nerve and each ROI. Lastly, group comparisons were made between the injured nerve groups and control group at each ROI location using a Wilcoxon rank-sum test (note that control group measures were made to be identical across ROI locations since they originate from a single 5-mm proximal ROI).

2.3 References

Beaulieu, C.F., Zhou, X., Cofer, G.P., Johnson, G.A., 1993. Diffusion-weighted MR microscopy with fast spin-echo. Magn. Reson. Med. 30, 201–206.

Caruyer, E., Lenglet, C., Sapiro, G., Deriche, R., 2013. Design of multishell sampling schemes with uniform coverage in diffusion MRI. Magn. Reson. Med. 69, 1534–1540.

Dortch, R.D., Apker, G.A., Valentine, W.M., Lai, B., Does, M.D., 2010. Compartment-specific enhancement of white matter and nerve ex vivo using chromium. Magn. Reson. Med. 64, 688–697. doi: 10.1002/mrm.22460

Fieremans, E., Jensen, J.H., Helpern, J.A., 2011. White matter characterization with diffusional kurtosis imaging. NeuroImage 58, 177–188. doi: 10.1016/j.neuroimage.2011.06.006

Gochberg, D.F., Gore, J.C., 2007. Quantitative magnetization transfer imaging via selective inversion recovery with short repetition times. Magn. Reson. Med. 57, 437–441.

Hennig, J., 1991. Echoes—how to generate, recognize, use or avoid them in MR-imaging sequences. Part II: Echoes in imaging sequences. Concepts Magn. Reson. 3, 179–192.

Johnson, G.A., Cofer, G.P., Gewalt, S.L., Hedlund, L.W., 2002. Morphologic phenotyping with MR microscopy: the visible mouse. Radiology 222, 789–793. doi: 10.1148/radiol.2223010531

Karnovsky, M.J., 1965. A formaldehyde-glutaraldehyde fixative of high osmolality for use in electron microscopy. J. Cell Biol. 27, 137A–138A.

Kass, M., Witkin, A., Terzopoulos, D., 1988. Snakes: active contour models. IJCV 1, 321–331.

Lawson, C.L., Hanson, R.J., 1974. Solving least squares problems. SIAM.

Lebel, R.M., Wilman, A.H., 2010. Transverse relaxometry with stimulated echo compensation. Magn. Reson. Med. 64, 1005–1014. doi: 10.1002/mrm.22487

Leys, C., Ley, C., Klein, O., Bernard, P., Licata, L., 2013. Detecting outliers: Do not use

standard deviation around the mean, use absolute deviation around the median. J. Exp. Soc. Psychol. 49, 764–766.

Neeman, M., Freyer, J.P., Sillerud, L.O., 1991. A simple method for obtaining cross-term-free images for diffusion anisotropy studies in NMR microimaging. Magn. Reson. Med. 21, 138–143.

Paxinos, G., Franklin, K.B., 2004. The mouse brain in stereotaxic coordinates. Gulf Professional Publishing.

Prasloski, T., Mädler, B., Xiang, Q.-S., MacKay, A., Jones, C., 2012. Applications of stimulated echo correction to multicomponent T2 analysis. Magn. Reson. Med. 67, 1803–1814.

Purea, A., Webb, A.G., 2006. Reversible and irreversible effects of chemical fixation on the NMR properties of single cells. Magn. Reson. Med. 56, 927–931. doi: 10.1002/mrm.21018

Shepherd, T.M., Thelwall, P.E., Stanisz, G.J., Blackband, S.J., 2009. Aldehyde fixative solutions alter the water relaxation and diffusion properties of nervous tissue. Magn. Reson. Med. 62, 26–34. doi: 10.1002/mrm.21977

Tabesh, A., Jensen, J.H., Ardekani, B.A., Helpern, J.A., 2010. Estimation of tensors and tensor-derived measures in diffusional kurtosis imaging. Magn. Reson. Med. 65, 823–836. doi: 10.1002/mrm.22655

Veraart, J., Sijbers, J., Sunaert, S., Leemans, A., Ben Jeurissen, 2013. Weighted linear least squares estimation of diffusion MRI parameters: strengths, limitations, and pitfalls. NeuroImage 81, 335–346. doi: 10.1016/j.neuroimage.2013.05.028

Whittall, K.P., MacKay, A.L., 1989. Quantitative interpretation of NMR relaxation data. J. Magn. Reson. (1969) 84, 134–152.

CHAPTER 3

DIFFUSION KURTOSIS IMAGING IN HYPOMYELINATED MOUSE BRAIN

3.1 Introduction

Abnormal brain myelination is present in many neurological diseases and disorders, such as multiple sclerosis (Allen and McKeown, 1979) and schizophrenia (Davis et al., 2003); therefore, non-invasive assessment of myelin may improve clinical diagnosis and/or insight into treatment of these conditions. At least two MRI methods are established as specific to myelin content—multi-exponential T_2 (MET_2) (MacKay et al., 1994; Menon et al., 1992) and quantitative magnetization transfer (qMT) (Gochberg and Gore, 2007; Koenig et al., 1990; Kucharcyzk et al., 1994; Sled and Pike, 2000)—but clinical application of these methods remains challenging, due to scan time requirements and precision limitations. In contrast, diffusion-weighted imaging is widely available and known to be sensitive to tissue microstructure, yet its ability to report on myelination remains an open question.

DWI is based on the sensitization of the acquired MR signal to the random displacement of water molecules, which is greatly influenced by tissue microstructure (e.g., cell membranes, myelin). In three dimensions, DWI can estimate a diffusion tensor, from which rotationally invariant parameters FA, MD, AD, and RD can be computed, making it especially applicable in the imaging of tissue with anisotropic microstructure such as white matter (Basser and Jones, 2002; Basser et al., 1994a; 1994b; Beaulieu, 2002; Le Bihan et al., 2001). Although DTI is sensitive to microstructural changes present in many neurological diseases and disorders, it utilizes a mathematical model of diffusion that lacks inherent specificity to any particular

component of neuronal microstructure. Additionally, DTI is based upon a Gaussian approximation of the water diffusion displacement probability distribution that assumes free, unrestricted diffusion. This limits the ability of the DTI model to characterize the heterogeneous microstructural environment that comprises brain white matter.

Diffusion kurtosis imaging (Hui et al., 2008; Jensen and Helpern, 2010; Jensen et al., 2005; Lu et al., 2006; Wu and Cheung, 2010) is a clinically-applicable extension of DTI with the potential of providing additional information regarding white matter microstructure, including its state of myelination (Cheung et al., 2009). Since its development, DKI has shown promising results in characterizing white matter changes in multiple diseases and disorders, including schizophrenia (Ramani et al., 2007), attention-deficit hyperactivity disorder (Helpern et al., 2011), and medial temporal lobe epilepsy (Lee et al., 2013). DKI is based upon the measurement of the kurtosis (i.e., a deviation from Gaussian) of the water diffusion displacement probability density function. Restrictions to water diffusion present in biological tissue cause the diffusion to become non-Gaussian, making DKI sensitive to heterogeneity in tissue microstructure. Similar to DTI, rotationally invariant metrics MK, AK, and RK can be derived from the kurtosis tensor. Also analogous to DTI, DKI is based upon a mathematical signal model of diffusion that does not explicitly model tissue microstructure and lacks inherent microstructural specificity. Additionally, both DTI and DKI utilize generic signal models that do not uniquely characterize multiple tissue compartments, such as intra- and extracellular spaces or crossing fibers. As an alternative to tensor models, biophysical models based on anatomy could provide improved characterization of white matter microstructure.

Fieremans and coworkers recently proposed a biophysical model of white matter based on the DKI framework with the goal of extracting metrics with a direct relationship to specific

components of white matter microstructure (Fieremans et al., 2011). This white matter tract integrity (WMTI) model utilizes measurements of apparent diffusion and kurtosis to separate white matter into two compartments: the intra-axonal space and extra-axonal space. From this model, potentially useful measures such as the axonal water fraction (F_a), intra-axonal diffusivity (D_a, assumed to be entirely parallel to the axon), and axial and radial extra-axonal diffusivities ($D_{e,\parallel}$ and $D_{e,\perp}$) can be computed. It has been hypothesized that D_a and $D_{e,\parallel}$ are associated with axonal integrity and F_a is a potential biomarker of axonal loss (Benitez et al., 2014; Falangola et al., 2014; Fieremans et al., 2013; Fieremans et al., 2012a; 2012b; Hui et al., 2012). Although myelin is not explicitly incorporated into the WMTI model, Fieremans et al. have postulated that $D_{e,\perp}$ (and the related extra-axonal tortuosity) is an indirect measure of myelination (Fieremans et al., 2012a).

The objective of this study was to evaluate the relationship of both DKI and the associated WMTI model with histological measure of white matter microstructure in two hypomyelinated mouse models related to the human genetic disease tuberous sclerosis complex. These conditional knockout models, *Tsc2* Olig2-Cre CKO (TSC) and *Rictor* Olig2-Cre CKO (Rictor), were chosen because they exhibit varied degrees of hypomyelination. Previously reported models related to tuberous sclerosis complex (*Tsc1* Emx1-Cre and *Rictor* Emx1-Cre) showed similar hypomyelination (Carson et al., 2013; Carson et al., 2012). The CKO mice in this study are viable into adulthood and capable of reproduction. High magnification transmission electron microscopy (EM) images of white matter tracts have shown that axon and myelin microstructure appear normal. Additionally, in contrast to the cuprizone mouse model of demyelination utilized in previous diffusion-weighted MRI studies (Song et al., 2005; Sun et al., 2006; Thiessen et al., 2013; J. Zhang et al., 2012), these genetic models are expected to exhibit

less or no inflammation or cellular damage and the hypomyelination is mostly uniform in white matter, making them better suited for a study focused on assessing the effects of hypomyelination on MRI contrast. In order to evaluate their relationship with myelin content, we compared DTI, DKI, and WMTI metrics with two established MR measures of myelin, myelin water fraction (MWF) from MET_2 and macromolecular pool-size ratio (PSR) from qMT, as well as quantitative measures of histology.

3.2 Materials and Methods

3.2.1 MRI and Histology Acquisition and Processing

For this study, normal (N = 8), TSC (N = 5), and Rictor (N=5) adult P60 mouse brains were excised and prepared for imaging as in Section 2.1.1. MRI acquisition methods were similar to those stated in Section 2.1.2 with minor adjustments. DWI was performed with TR = 200 ms, b = 3000 and 6000 s/mm^2, 30 directions (same directions for each shell), and NEX = 2 with gradient polarity reversal to mitigate background gradient cross-terms (Neeman et al., 1991). Additionally, 5 b=0 images were collected instead of 6. For the MET_2 scan, BW = 38.5 kHz, NEX = 6, and scan time ≈ 6 hr (instead of 75 kHz, NEX = 8, and 8 hr, respectively). The qMT acquisition was the same as defined in Section 2.1.2.3. All MRI parameters were estimated using the methods stated in Section 2.1.3.

After MRI was performed, normal (N = 6), TSC (N = 4), and Rictor (N = 3) mouse brains were sectioned for histology using the approach described in Section 2.1.4.1. A larger sample size was used for the control group due to greater intragroup variation in myelin content compared with the CKO groups. Additionally, data from 1 TSC MidCC section and 1 TSC GCC

section were removed from analysis due to corruption of these sections during histology processing, so a fourth TSC brain was added to ensure that there were at minimum 3 samples of each ROI. EM data were collected and analyzed as in Section 2.1.4.2, except myelin thickness for each axon was determined by taking the average of manual measurements along 2 different axes, and histologic axon fraction was not adjusted to exclude myelin contributions to the overall area (the true axon fraction is reported in this study).

3.2.2 Group ROI Analysis

For group analysis, b=0 images were registered to a representative normal mouse brain using an affine registration followed by a deformable demons registration (Thirion, 1998). DTI, DKI, WMTI, MWF, and PSR parameter maps were then registered using the same transformations derived from the b=0 registration. Referencing a standard mouse brain atlas (Paxinos and Franklin, 2004), ROIs were manually delineated on 2D cross-sections for 6 white matter regions: MidCC, GCC, SCC, AC, external capsule (EC), and internal capsule (IC). For direct comparison to the histology ROIs, the MidCC, GCC, SCC, and AC ROIs were drawn on a mid-sagittal cross-section at Bregma -0.7 mm, 1 mm, -2.5 mm, and 0.2 mm, respectively. The EC and IC ROIs were drawn on a coronal cross-section at Bregma -1.7 mm and were only included in analyses involving MR metrics alone. For the WMTI analysis, a small number of voxels (< 1% of all WM voxels used in this analysis) exhibited abnormally high $D_{e,\perp}$ (> 1 $\mu m^2/ms$; mean ± SD of remaining WM voxels $D_{e,\perp} = 0.27 \pm 0.07$ $\mu m^2/ms$) and were not included in subsequent analysis. Comparisons of DTI, DKI, and WMTI indices between the control group and knockout groups were then made for each ROI using a Wilcoxon rank-sum test. Using the ROI means for each individual mouse brain, linear correlations were determined between DTI, DKI, and WMTI

parameters and both MR measures of myelin and histologic measures with multiple comparisons correction performed using a simple Bonferroni correction.

3.3 Results

3.3.1 Histology

Figure 3.1 displays electron micrographs, along with their corresponding segmentations, of the splenium from normal, Rictor, and TSC brains. In comparison to the normal brain, the Rictor brain visually showed minor decreases in myelin thickness and myelinated axon density, while the TSC brain showed a much greater decrease in myelinated axon density. Table 3.1 displays

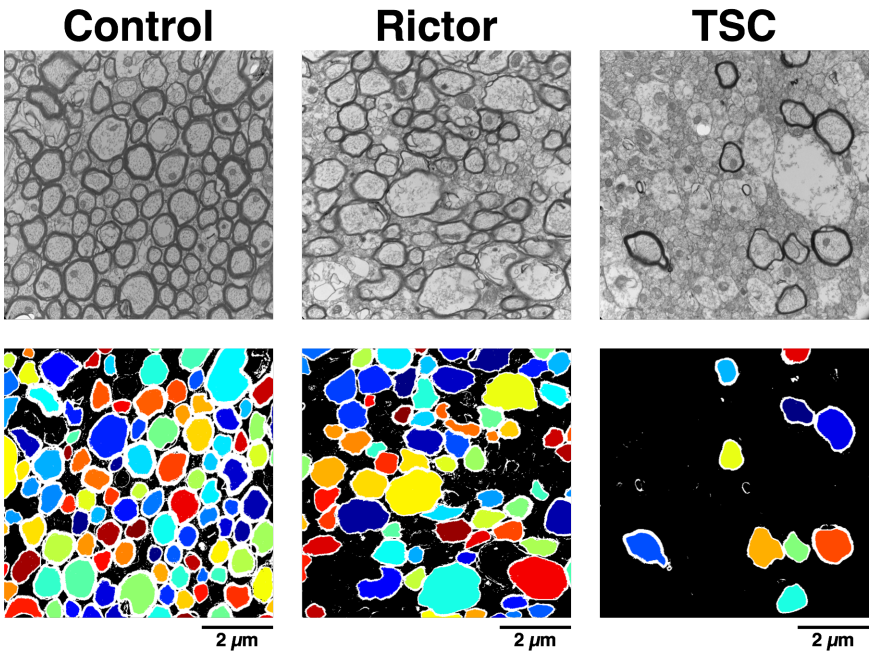

FIG. 3.1. Representative EM images of white matter. (Top row) EM images of the splenium from control, Rictor and TSC mouse brains. (Bottom row) Processed and segmented EM images corresponding to the images shown on the top row. Compared to the control brain, Rictor brain WM shows a slight decrease in myelin thickness and myelinated axon density. TSC brain WM shows a significant decrease in myelinated axon density.

group means and standard errors of all histology measures for each ROI. Significant differences compared to the control group are identified by * ($p < 0.05$), ** ($p < 0.01$), and *** ($p < 0.001$).

Table 3.1. Group mean ± SEM of quantitative histology measures for control, Rictor, and TSC groups.

		f_m	f_a	d_a (μm)	z_m (nm)	g	ρ_a (axons/μm^2)
MidCC	Control	0.167 ± 0.022	0.394 ± 0.029	0.558 ± 0.026	55.0 ± 3.1	0.815 ± 0.007	1.124 ± 0.079
	Rictor	0.124 ± 0.025***	0.374 ± 0.047	0.578 ± 0.033	45.2 ± 3.5***	0.844 ± 0.011***	0.945 ± 0.084*
	TSC	0.046 ± 0.011***	0.183 ± 0.049***	0.712 ± 0.134***	36.5 ± 5.1***	0.894 ± 0.014***	0.310 ± 0.113***
GCC	Control	0.196 ± 0.018	0.439 ± 0.023	0.588 ± 0.024	58.7 ± 2.7	0.811 ± 0.010	1.097 ± 0.076
	Rictor	0.103 ± 0.019***	0.380 ± 0.050**	0.671 ± 0.033***	44.5 ± 3.2***	0.863 ± 0.012***	0.738 ± 0.084***
	TSC	0.023 ± 0.007***	0.071 ± 0.029***	0.714 ± 0.160**	46.8 ± 5.8***	0.850 ± 0.039***	0.100 ± 0.027***
SCC	Control	0.187 ± 0.019	0.416 ± 0.025	0.560 ± 0.020	51.1 ± 2.4	0.830 ± 0.009	1.205 ± 0.074
	Rictor	0.138 ± 0.026**	0.398 ± 0.045	0.647 ± 0.031***	46.1 ± 3.2***	0.866 ± 0.009***	0.989 ± 0.098**
	TSC	0.049 ± 0.017***	0.145 ± 0.049***	0.894 ± 0.132***	56.9 ± 8.2	0.879 ± 0.012***	0.197 ± 0.054***
AC	Control	0.206 ± 0.023	0.384 ± 0.024	0.600 ± 0.032	60.0 ± 3.3	0.821 ± 0.011	1.094 ± 0.106
	Rictor	0.117 ± 0.020***	0.376 ± 0.041	0.748 ± 0.069***	52.2 ± 4.9***	0.868 ± 0.010***	0.695 ± 0.114**
	TSC	0.040 ± 0.013***	0.097 ± 0.033***	0.792 ± 0.044***	61.7 ± 7.9	0.862 ± 0.017***	0.152 ± 0.040***

Significant differences compared with the control group are indicated by * ($p \leq 0.05$), ** ($p \leq 0.01$), and *** ($p \leq 0.001$).

The g-ratios for the control group were similar to those reported in previous studies of normal mouse brain ($g \sim 0.8$) (Mason et al., 2001). Compared to the control group, the TSC group exhibited major decreases in f_m, f_a and ρ_a in all ROIs. There were also significant decreases in z_m in the MidCC and GCC. The TSC group showed significant increases in d_a and g for all ROIs. Compared to the control group, the Rictor group had significant decreases in f_m, z_m, and ρ_a and significant increases in g for all ROIs. Also, the Rictor group showed significant increases in d_a in the GCC, SCC, and AC and a significant decrease in f_a for the GCC. Overall, as anticipated,

the microstructural differences between the Rictor and control groups were fewer and less extreme than those observed between the TSC and control groups.

3.3.2 MRI

Typical white matter SNR of the DWI b=0 images was ≈ 150, calculated as the ratio of the signal amplitude to the standard deviation of the background noise. Approximate mean signal attenuations for the b = 3000 and 6000 s/mm^2 acquisitions were 44% and 57%, respectively (assuming a diffusivity of 0.25 μm^2/ms and a kurtosis of 1.75, taken from approximate MD and MK of white matter in this study). The high SNR of the DWI scan resulted in high-precision estimates of DTI parameters in white matter, with estimated standard deviations of < 0.01 and < 0.01 μm^2/ms for FA and MD, respectively (Landman et al., 2007). For the MET$_2$ acquisition, white matter SNR of the first echo image was ≈ 600, and for the qMT acquisition, SNR of the

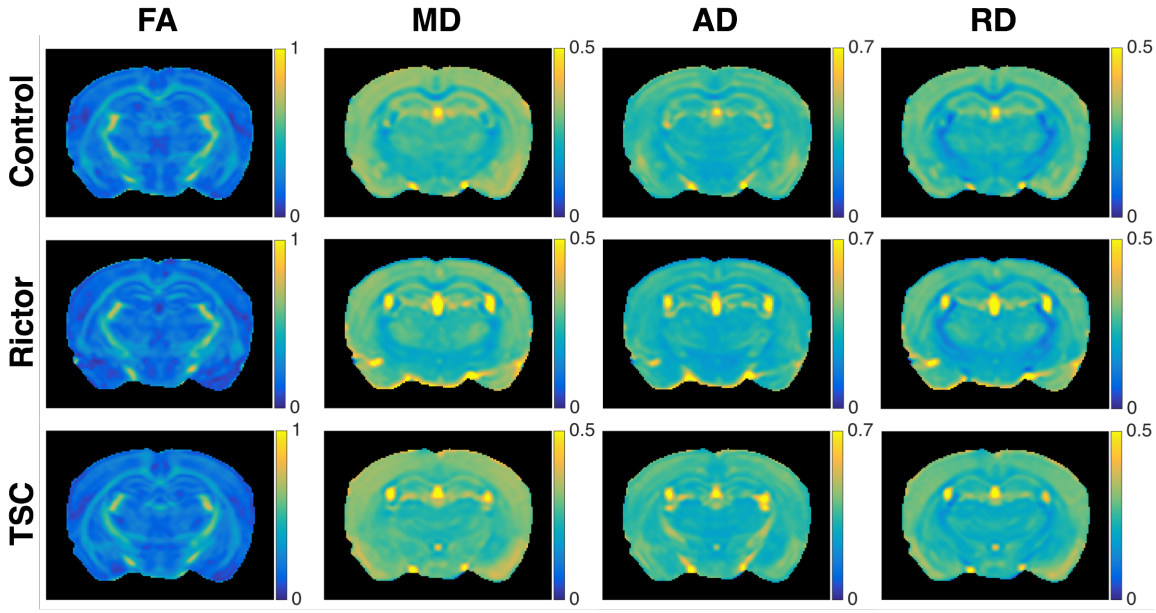

FIG. 3.2. Representative coronal DTI parameter maps. The rows represent the three groups: control (top), Rictor (middle), and TSC (bottom). The columns represent the DTI parameters FA, MD, AD, and RD. FA is unitless and diffusivities are in units of μm^2/ms.

longest inversion time image was ≈ 250. These high SNR acquisitions provided high-precision estimates of both MWF and PSR in white matter. Representative T_2 spectra from a single MidCC voxel for each group are shown in Fig. 3.14 (see Section 3.7). Intra/extra-axonal water T_2s in the MidCC for the control, Rictor, and TSC groups were 36.2 ± 0.4 ms, 39.4 ± 0.9 ms, and 40.6 ± 1.1 ms (mean ± SEM), respectively. Myelin water T_2s in the same region were 5.4 ± 0.3 ms, 5.0 ± 0.2 ms, and 5.8 ± 0.5 ms for the control, Rictor, and TSC groups, respectively.

3.3.3 DTI

Representative coronal parameter maps for the DTI indices FA, MD, AD, and RD from each of the three groups are shown in Fig. 3.2. Compared with the control group, the knockout groups had a decrease in FA and increase in MD and RD of white matter. As anticipated, these differences were more apparent for the TSC group compared with the Rictor group, due to more severe hypomyelination present in the TSC brains. Changes in white matter AD between the three groups were not visually apparent. DTI parameter maps for the sagittal and axial orientations can be seen in Figs. 3.15 and 3.16, respectively (see Section 3.7).

Figure 3.3 shows group comparisons of FA, MD, AD, and RD for 6 white matter ROIs. Compared to the control group, the Rictor group showed no significant differences in FA and AD and significant increases in MD for the anterior commissure and RD for 2 of the 6 ROIs (i.e., the splenium and anterior commissure). The TSC group exhibited significant decreases in FA for 5 of the 6 ROIs, significant increases in AD for 4 of the 6 ROIs, and significant increases in MD and RD for all 6 ROIs examined. There were more WM regions with significant differences in MD and RD than FA and AD, indicating that MD and RD were overall more sensitive than FA and AD to the hypomyelination present within the knockout models. Additionally, DTI

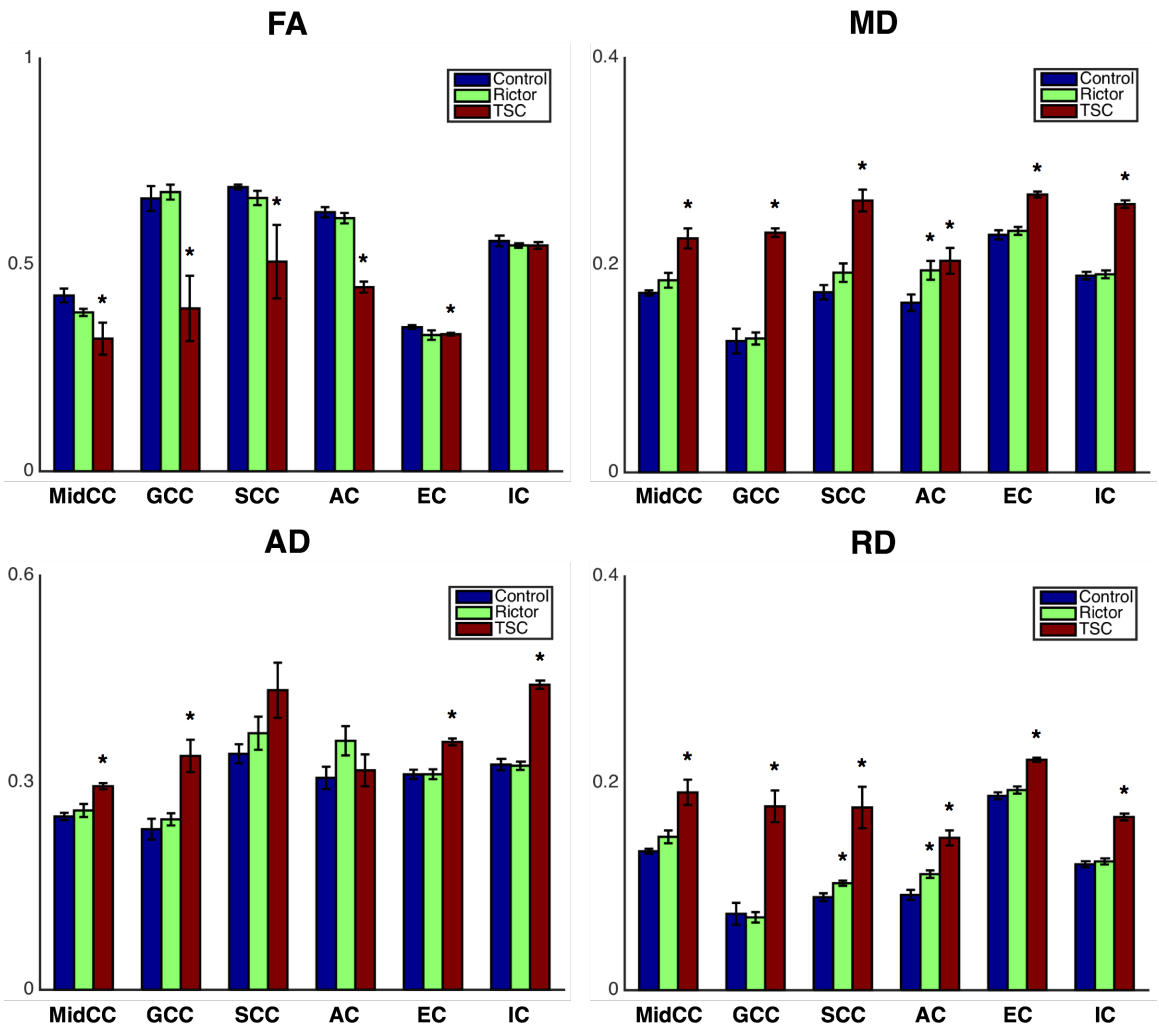

FIG. 3.3. ROI group comparison of DTI parameters FA, MD, AD, and RD. Bar heights represent the ROI parameter means across each group, with error bars spanning the mean ± SEM. The three groups are represented with different colors: control = blue, Rictor = green, and TSC = red. 6 WM ROIs are indicated on the x-axis: MidCC = midbody of the corpus callosum, GCC = genu, SCC = splenium, AC = anterior commissure, EC = external capsule, and IC = internal capsule. FA is unitless and diffusivities are in units of $\mu m^2/ms$. * denotes $p < 0.05$ for comparison between the control group and each CKO group.

parameters were unable to distinguish the Rictor group from the control group (significant differences in MD and RD for only 1 and 2 ROIs, respectively).

3.3.4 DKI

Representative coronal parameter maps for the DKI indices MK, AK, and RK from each of the three groups are shown in Fig. 3.4. Compared with the control group, the knockout groups showed a decrease in MK and RK of white matter. Similar to the DTI results, these differences were more apparent for the TSC group compared with the Rictor group. There were minimal changes in white matter AK between the three groups. Sagittal and axial DKI parameter maps are shown in Figs. 3.17 and 3.18, respectively (see Section 3.7).

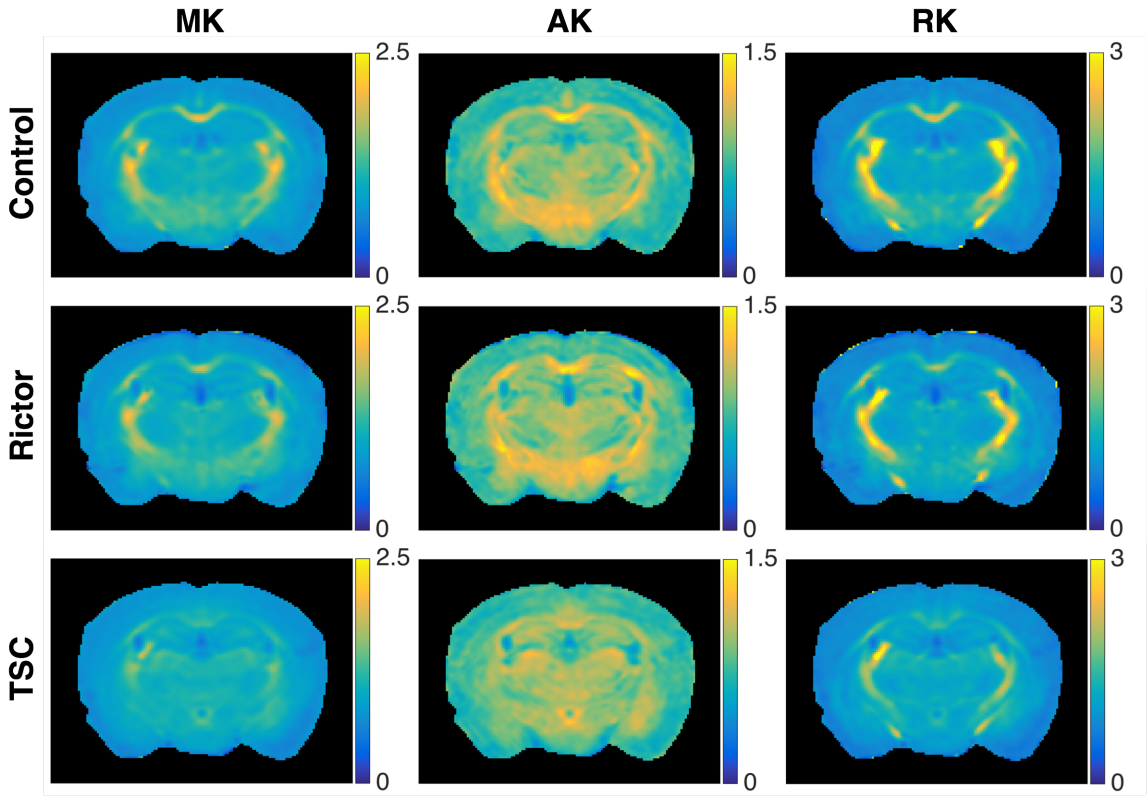

FIG. 3.4. Representative coronal DKI parameter maps. The rows represent the three groups: control (top), Rictor (middle), and TSC (bottom). The columns represent the DKI parameters MK, AK, and RK. Kurtosis is unitless.

Group comparisons of MK, AK, and RK for 6 white matter ROIs are described in Fig. 3.5. When compared to the control group, the Rictor group had significant decreases in MK for 4

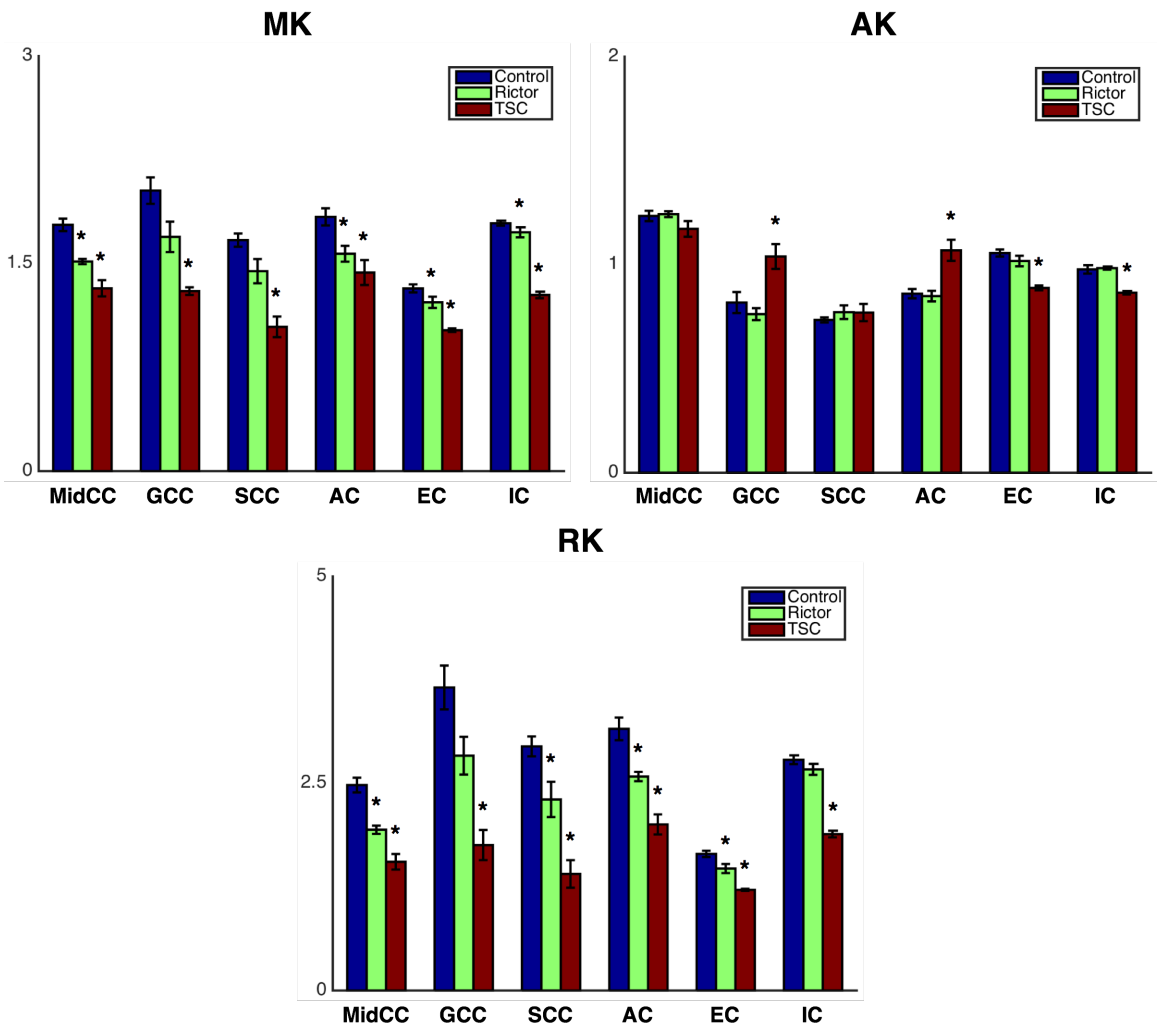

FIG. 3.5. ROI group comparison of DKI parameters MK, AK, and RK. Bar heights represent the ROI parameter means across each group, with error bars spanning the mean ± SEM. The three groups are represented with different colors: control = blue, Rictor = green, and TSC = red. 6 WM ROIs are indicated on the x-axis: MidCC = midbody of the corpus callosum, GCC = genu, SCC = splenium, AC = anterior commissure, EC = external capsule, and IC = internal capsule. Kurtosis is unitless. * denotes $p < 0.05$ for comparison between the control group and each CKO group.

of 6 ROIs and RK for 4 of 6 ROIs with no significant differences in AK. Significant decreases in MK and RK for all 6 ROIs were seen in the TSC group. For AK of the TSC group, there were significant increases in the GCC and AC and significant decreases in the EC and IC. Since most ROIs showed significant differences in MK and RK, this indicates that MK and RK were highly sensitive to changes in myelination present in the two knockout models. Additionally, significant

decreases in MK and RK for the Rictor group present in most white matter ROIs indicate an increased sensitivity of these metrics to myelination compared with DTI metrics.

3.3.5 WMTI

Figure 3.6 shows representative parameter maps for the WMTI metrics F_a, D_a, $D_{e,\parallel}$, and $D_{e,\perp}$ from each of the three groups. Since the WMTI model is only valid for white matter, WMTI parameter

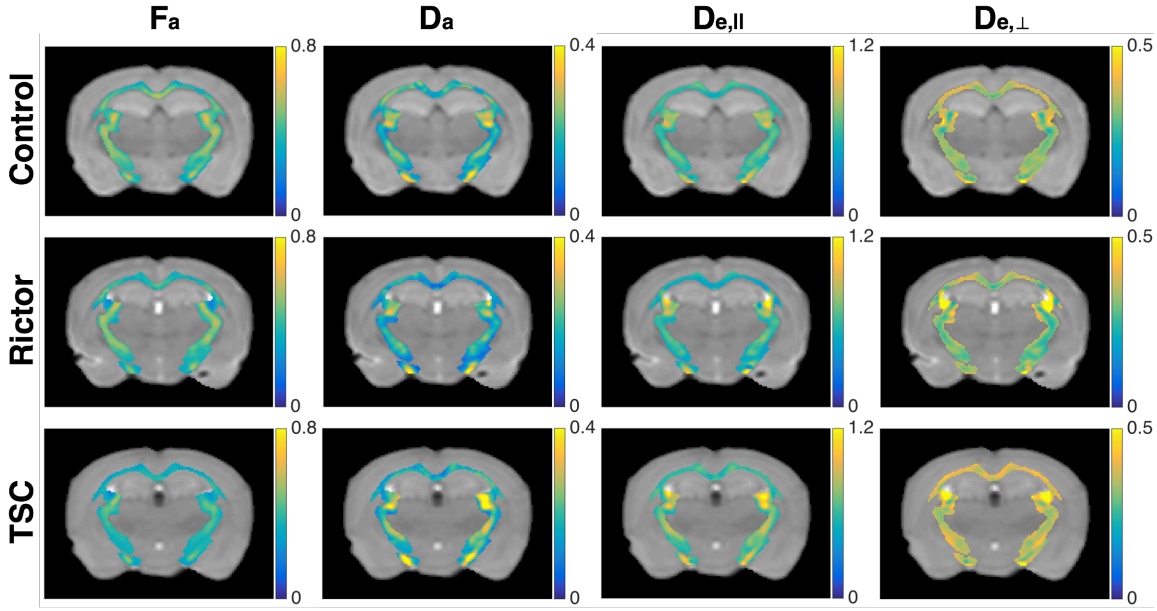

FIG. 3.6. Representative coronal WMTI parameter maps. WMTI parameter values for white matter voxels are overlaid on the b=0 image. The rows represent the three groups: control (top), Rictor (middle), and TSC (bottom). The columns represent the WMTI parameters F_a, D_a, $D_{e,\parallel}$, and $D_{e,\perp}$. F_a is unitless and diffusivities are in units of $\mu m^2/ms$.

values for white matter voxels (voxels with FA > 0.35 in a control brain) were overlaid on the b=0 image. Compared with the control group, the knockout groups exhibited a major decrease in F_a and a minor increase in $D_{e,\perp}$ of white matter. As expected, these differences were more apparent for the TSC group compared with the Rictor group. Changes in D_a and $D_{e,\parallel}$ between the

control and knockout groups were not visually apparent. Figs. 3.19 and 3.20 contain WMTI parameter maps in the sagittal and axial planes, respectively (see Section 3.7).

Group comparisons of F_a, D_a, $D_{e,\parallel}$, and $D_{e,\perp}$ for 6 different white matter ROIs are

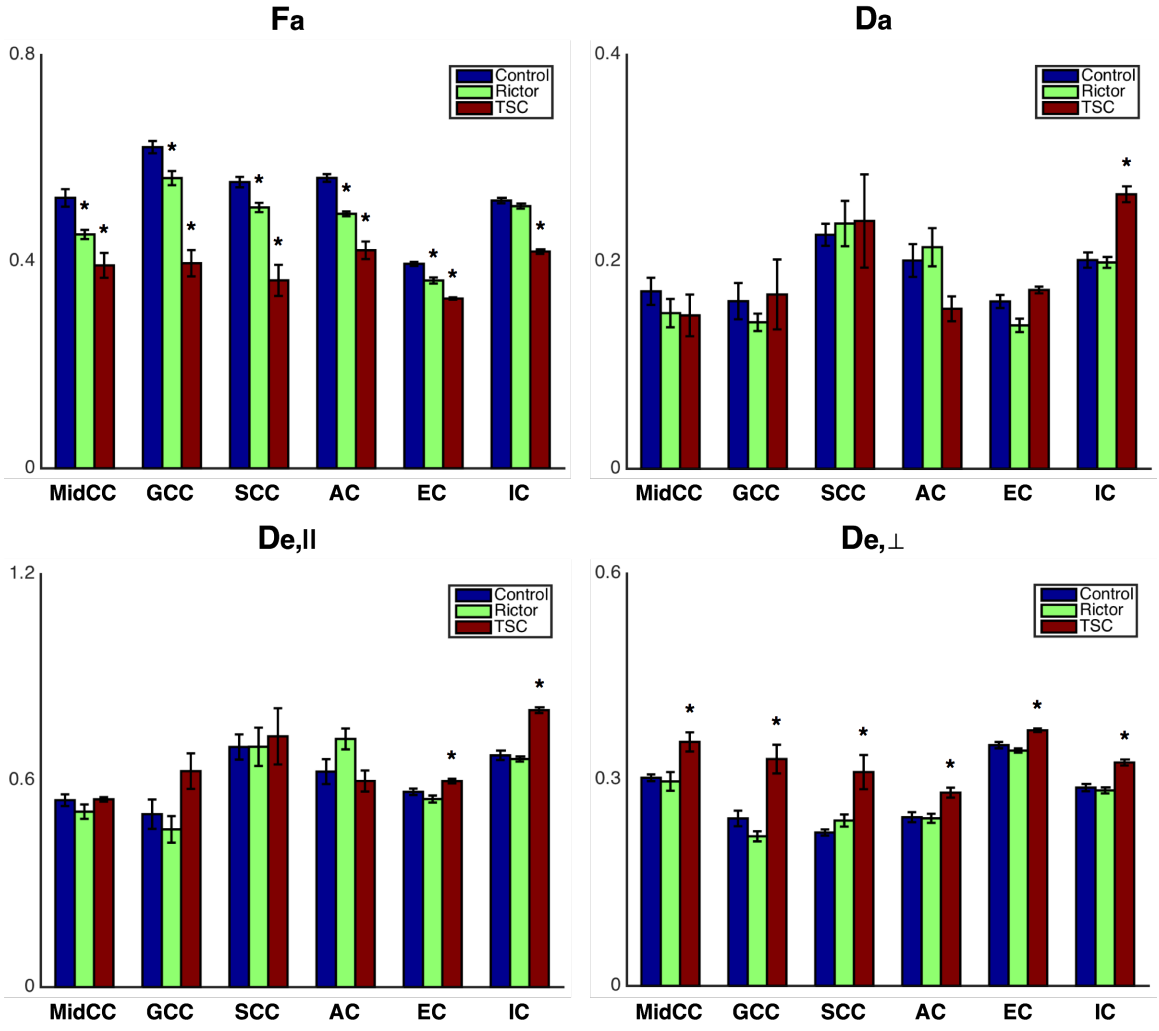

FIG. 3.7. ROI group comparison of WMTI parameters F_a, D_a, $D_{e,\parallel}$, and $D_{e,\perp}$. Bar heights represent the ROI parameter means across each group, with error bars spanning the mean ± SEM. The three groups are represented with different colors: control = blue, Rictor = green, and TSC = red. 6 WM ROIs are indicated on the x-axis: MidCC = midbody of the corpus callosum, GCC = genu, SCC = splenium, AC = anterior commissure, EC = external capsule, and IC = internal capsule. F_a is unitless and diffusivities are in units of $\mu m^2/ms$. * denotes $p < 0.05$ for comparison between the control group and each CKO group.

represented by bar plots in Fig. 3.7. The Rictor group showed significant decreases in F_a for 5 of 6 ROIs when compared to the control group. No significant differences in D_a, $D_{e,\parallel}$, and $D_{e,\perp}$ existed between the control and Rictor groups. For the TSC group, there were significant decreases in F_a and significant increases in $D_{e,\perp}$ for all 6 ROIs. Also, the TSC group had significant increases in D_a for 1 ROI (i.e., the internal capsule) and in $D_{e,\parallel}$ for 2 ROIs (i.e., the external and internal capsules). With significant differences in F_a present in most ROIs, these results indicate that F_a was highly sensitive to microstructural changes present within the CKO models. In comparison, $D_{e,\perp}$ was less sensitive and unable to distinguish between the control and Rictor groups.

3.3.6 Linear Correlation Analysis

Linear correlation analysis was performed across all individual animals and all ROIs. Figure 3.8 contains scatter plots displaying linear correlations between DTI metrics and 3 different measures of myelin, with each point representing an ROI mean from a single animal. None of the DTI parameters correlated with MWF. FA and RD showed significant correlations with PSR, but these were weak with the strongest being between RD and PSR ($r^2 = 0.14$). There were moderate correlations between DTI parameters and histologic myelin fraction, with $r^2 = 0.35$ and 0.37 for correlations MD-f_m and RD-f_m, respectively.

Similar to Fig. 3.8, Fig. 3.9 shows linear correlations between DTI metrics and histologic measures of axon diameter, myelinated axon density, histologic axon fraction, and g-ratio. FA did not have any significant correlations, while MD and RD showed moderate to strong correlations with all four histology measures, the strongest being between MD and f_a ($r^2 = 0.44$). For Figs. 3.8 and 3.9, AD is not shown due to it not showing any significant correlations.

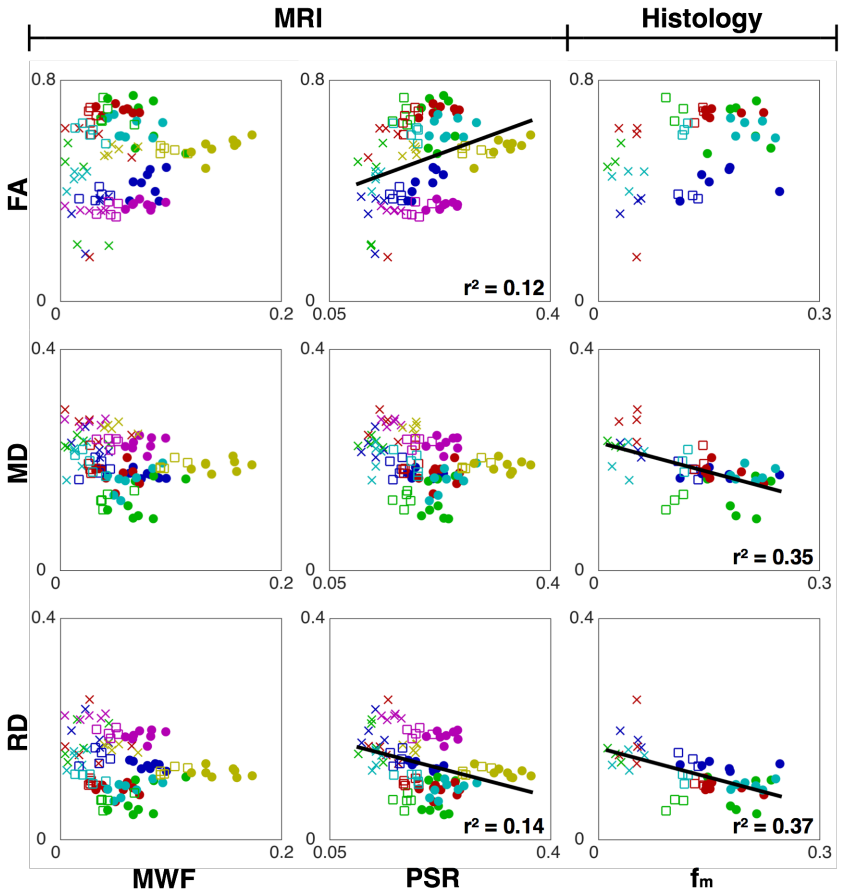

FIG. 3.8. Linear correlation plots between DTI metrics FA, MD, and RD (y-axis) and myelin measures MWF, PSR, and f_m (x-axis). Each point is an ROI mean from an individual mouse brain. The shape represents the group: control = circle, Rictor = square, and TSC = x and the color represents the WM region: MidCC = blue, GCC = green, SCC = red, AC = cyan, EC = magenta, IC = yellow. For significant correlations, r^2 is shown in the lower right-hand corner of each plot. FA, MWF, PSR, and f_m are unitless, MD and RD are in units of $\mu m^2/ms$.

Linear correlations between DKI metrics and 3 unique measures of myelin are shown in Fig. 3.10. Both MK and RK correlated significantly with MWF and PSR, with the strongest correlations being MK and RK with PSR (r^2 = 0.27 and 0.25, respectively). Also, MK and RK correlated strongly with f_m (r^2 = 0.48 and 0.49, respectively). All correlations between DKI metrics MK and RK and the myelin measures were stronger than the corresponding correlations between DTI metrics MD and RD and the same myelin measures.

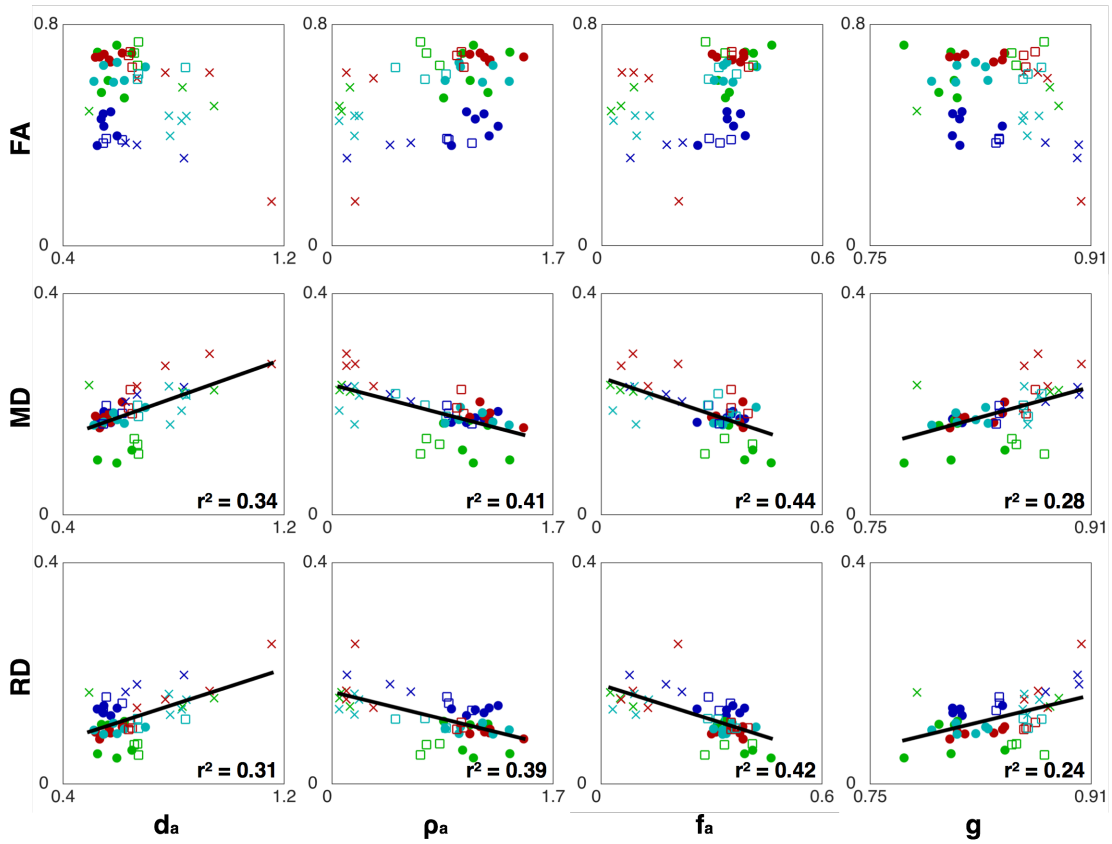

FIG. 3.9. Linear correlation plots between DTI metrics FA, MD, and RD (y-axis) and the histologic measures d_a, ρ_a, f_a, and g (x-axis). Each point is an ROI mean from an individual mouse brain. The shape represents the group: control = circle, Rictor = square, and TSC = x and the color represents the WM region: MidCC = blue, GCC = green, SCC = red, AC = cyan. For significant correlations, r^2 is shown in the lower right-hand corner of each plot. FA, f_a, and g are unitless, MD and RD are in units of $\mu m^2/ms$, d_a is in units of μm, and ρ_a is in units of axons/μm^2.

Scatter plots displaying linear correlations between DKI metrics and the histologic measures of axon diameter, myelinated axon density, axon fraction, and g-ratio are shown in Fig. 3.11. MK and RK had strong correlations with all four histologic measures, the strongest being between MK and g-ratio ($r^2 = 0.46$). Correlation strengths between DKI metrics and d_a, ρ_a, and f_a were similar to those observed with DTI metrics. However, correlations with g-ratio for MK and RK were much stronger than those observed for MD and RD. For Figs. 3.10 and 3.11, AK is not shown because there were no significant correlations observed with this metric.

Linear correlations between WMTI metrics and 3 different measures of myelin are shown in Fig. 3.12. F_a correlated significantly with MWF and PSR ($r^2 = 0.14$ and 0.23, respectively). A strong correlation existed between F_a and histologic myelin fraction ($r^2 = 0.58$). $D_{e,\perp}$ did not correlate with any of the 3 myelin measures. Figure 3.13 shows scatter plots with linear

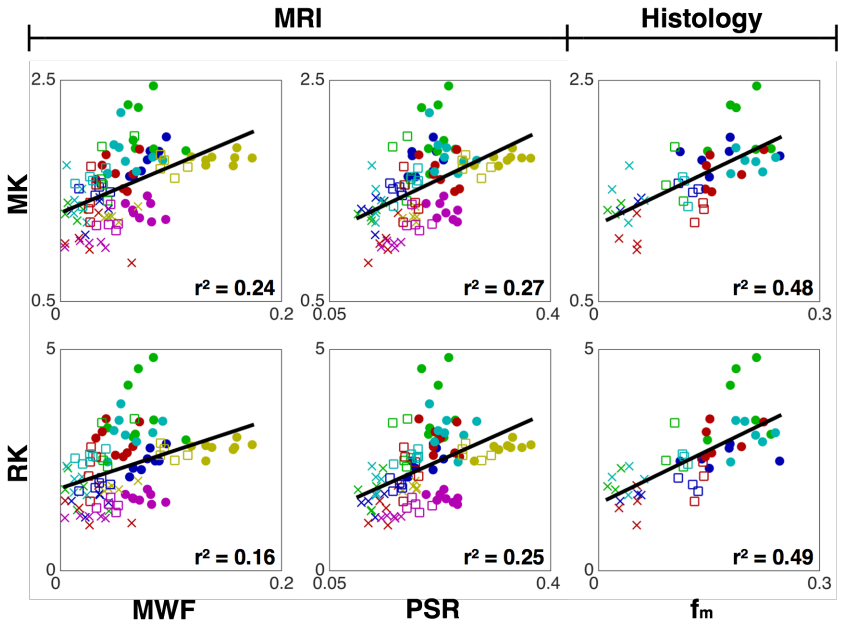

FIG. 3.10. Linear correlation plots between DKI metrics MK and RK (y-axis) and myelin measures MWF, PSR, and f_m (x-axis). Each point is an ROI mean from an individual mouse brain. The shape represents the group: control = circle, Rictor = square, and TSC = x and the color represents the WM region: MidCC = blue, GCC = green, SCC = red, AC = cyan, EC = magenta, IC = yellow. For significant correlations, r^2 is shown in the lower right-hand corner of each plot. MK, RK, MWF, PSR, and f_m are unitless.

correlations between WMTI indices and histologic measures of axon diameter, myelinated axon density, axon fraction, and g-ratio. F_a exhibited strong correlations with all four histology measures, the strongest being between F_a and ρ_a ($r^2 = 0.55$). $D_{e,\perp}$ did not exhibit any significant correlations with these histology metrics. For Figs. 3.12 and 3.13, D_a and $D_{e,\parallel}$ are not shown

because there were no significant correlations observed with these metrics. Table 3.2 summarizes the results of the correlation analysis, showing the r^2 values for all significant correlations of DTI, DKI, and WMTI metrics with myelin and histology measures.

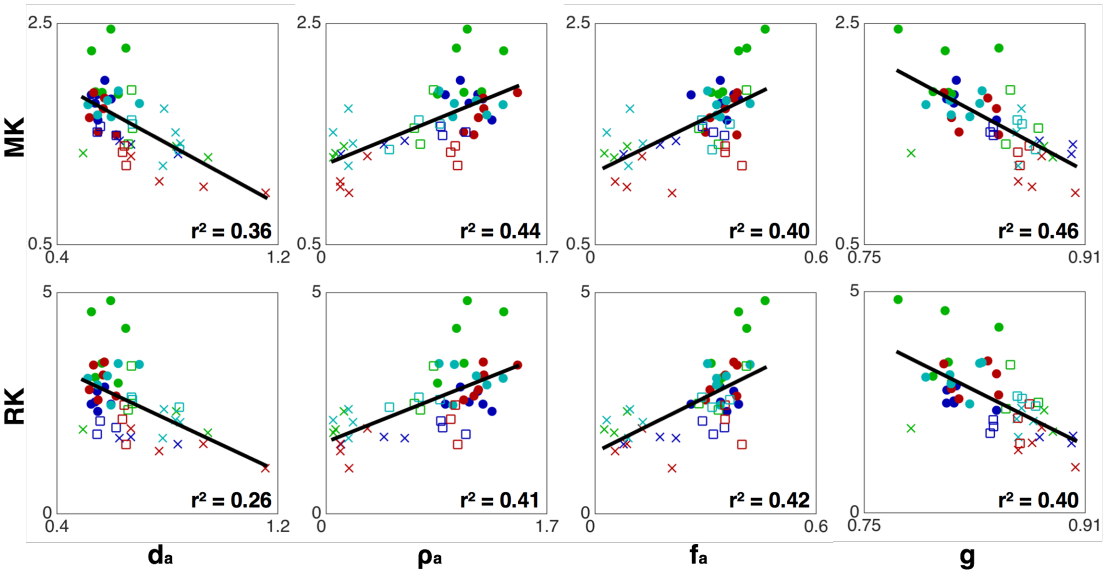

FIG. 3.11. Linear correlation plots between DKI metrics MK and RK (y-axis) and the histologic measures d_a, ρ_a, f_a, and g (x-axis). Each point is an ROI mean from an individual mouse brain. The shape represents the group: control = circle, Rictor = square, and TSC = x and the color represents the WM region: MidCC = blue, GCC = green, SCC = red, AC = cyan. For significant correlations, r^2 is shown in the lower right-hand corner of each plot. MK, RK, f_a, and g are unitless, d_a is in units of μm, and ρ_a is in units of axons/μm^2.

3.4 Discussion

The quantitative histology data shown in Table 3.1 indicate that both the Rictor and TSC knockout models show hypomyelination, with the TSC model exhibiting an almost complete lack of myelinated axons. The more subtle change in myelination present in the Rictor model (in contrast to the TSC and cuprizone models) is beneficial in evaluating MRI methods and their ability to report on varied levels of myelination that may occur during development or

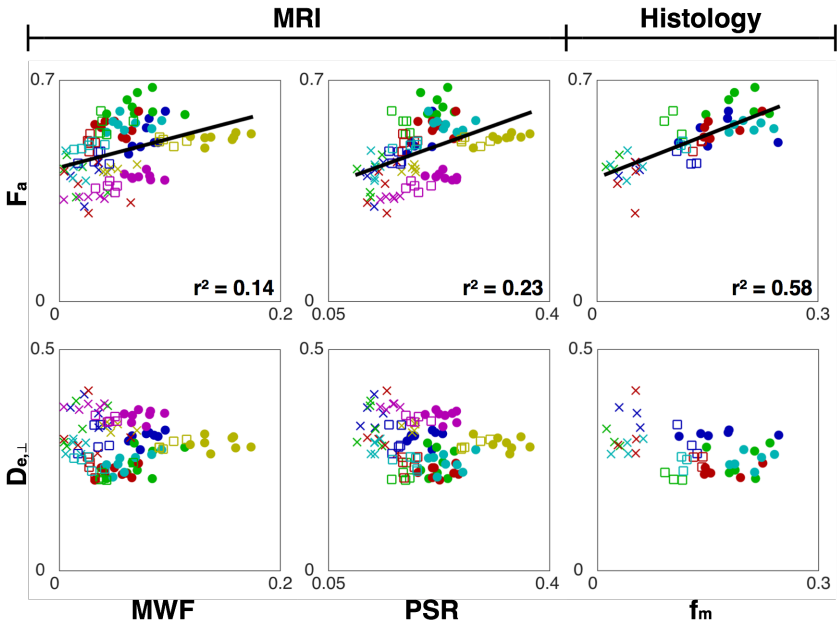

FIG. 3.12. Linear correlation plots between WMTI metrics F_a and $D_{e,\perp}$ (y-axis) and myelin measures MWF, PSR, and f_m (x-axis). Each point is an ROI mean from an individual mouse brain. The shape represents the group: control = circle, Rictor = square, and TSC = x and the color represents the WM region: MidCC = blue, GCC = green, SCC = red, AC = cyan, EC = magenta, IC = yellow. For significant correlations, r^2 is shown in the lower right-hand corner of each plot. F_a, MWF, PSR, and f_m are unitless, $D_{e,\perp}$ is in units of $\mu m^2/ms$.

de/remyelinating pathologies. These results agree with previous studies showing that TSC and Rictor knockouts exhibit abnormal myelination, with the TSC mice portraying a more severe abnormal phenotype (Carson et al., 2013; Carson et al., 2012). However, this study is the first to report quantitative histological measures of axons and myelin content (e.g., axon diameter, myelin thickness, histologic myelin fraction) for these specific mouse models.

The DTI results in Figs. 3.2 and 3.3 showed that hypomyelination resulted in decreases in white matter FA and increases in MD and RD, with fewer changes in AD. These results agree with previous studies stating that a decrease in myelination causes an increase in radial diffusivity but minimal changes in axial diffusivity (Song et al., 2005; Song et al., 2002). However, DTI metrics mostly did not detect differences between the control and Rictor groups,

indicating an inability of DTI to distinguish subtle changes in myelin thickness and myelinated axon density. The DKI results in Figs. 3.4 and 3.5 showed that hypomyelination caused decreases in MK and RK with minimal changes in AK. This is similar to the DTI results in that

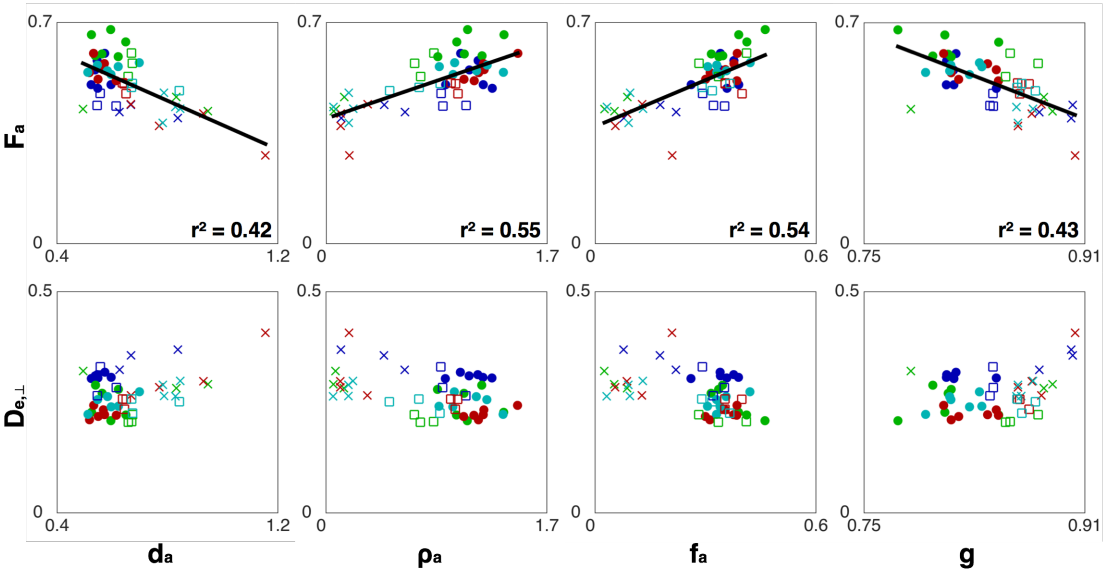

FIG. 3.13. Linear correlation plots between WMTI metrics F_a and $D_{e,\perp}$ (y-axis) and the histologic measures d_a, ρ_a, f_a, and g (x-axis). Each point is an ROI mean from an individual mouse brain. The shape represents the group: control = circle, Rictor = square, and TSC = x and the color represents the WM region: MidCC = blue, GCC = green, SCC = red, AC = cyan. For significant correlations, r^2 is shown in the lower right-hand corner of each plot. F_a, f_a, and g are unitless, $D_{e,\perp}$ is in units of $\mu m^2/ms$, d_a is in units of μm, and ρ_a is in units of axons/μm^2.

changes in myelination caused changes in radial kurtosis but not axial kurtosis. In contrast to DTI metrics, significant differences in MK and RK between the control and Rictor groups were present in most ROIs, indicating higher sensitivity to changes in myelin thickness and myelinated axon density compared with DTI.

Because inter-animal variability within each group was approximately an order of magnitude greater than the variability of the DTI metrics themselves, increasing the image SNR in this case would have little effect on the group-wise comparisons. In other words, in the

Table 3.2. r^2 values from linear correlation analysis of DTI, DKI, and WMTI metrics.

		DTI				DKI			WMTI			
		FA	MD	AD	RD	MK	AK	RK	F_a	D_a	$D_{e,\parallel}$	$D_{e,\perp}$
MRI	MWF					0.24		0.16	0.14			
	PSR	0.12			0.14	0.27		0.25	0.23			
Histology	f_m		0.35		0.37	0.48		0.49	0.58			
	f_a		0.44		0.42	0.40		0.42	0.54			
	d_a		0.34		0.31	0.36		0.26	0.42			
	z_m											
	ρ_a		0.41		0.39	0.44		0.41	0.55			
	g		0.28		0.24	0.46		0.40	0.43			

Only r^2 values for significant correlations ($p < 0.05$) are shown.

hypothetical case that twice as many acquisitions of a single b-value shell were utilized instead of two shells, the DTI metrics would still prove to be less sensitive to the changes in tissue microstructure than the DKI metrics. These results agree with a previous study that showed that DKI was more sensitive than DTI to changes present in a rat brain maturation model (Cheung et al., 2009). Also, these results make intuitive sense because the assessment of non-Gaussian diffusion in DKI provides more information about the effects that tissue microstructure have on water diffusion and therefore is more sensitive to microstructural changes. This emphasizes the utility of moving towards a higher order diffusion signal model, such as the DKI model, for microstructural assessment.

The WMTI results in Figs. 3.6 and 3.7 showed that hypomyelination caused decreases in F_a, increases in $D_{e,\perp}$, and minimal changes in D_a and $D_{e,\parallel}$. These results agree with previous hypotheses stating that F_a is sensitive to axonal loss, $D_{e,\perp}$ increases with reduced myelination, and

D_a and $D_{e,||}$ are mostly unaffected by changes in myelination (Fieremans et al., 2012a). Similar to the DKI results, F_a was significantly different between the control and Rictor groups in most ROIs. This was expected since the estimation of F_a is closely related to radial kurtosis. However, even though significant increases in $D_{e,\perp}$ between the control and TSC groups were found for all ROIs, there were no significant differences in $D_{e,\perp}$ between the control and Rictor groups. This result indicates that $D_{e,\perp}$ was not as sensitive to less extreme changes in myelin thickness and myelinated axon density as conventional DKI metrics.

The linear correlation analysis was performed across all individual mouse brains from the 3 groups and all of the WM ROIs analyzed. The two different hypomyelinated mouse models were utilized to create variation in white matter microstructure for the purpose of evaluating DWI metrics and to allow for meaningful correlations. There was not enough variation within an ROI and within each group to provide any correlation. Figures 3.8 and 3.9 showed that DTI metrics MD and RD did have some correlation with myelin content and other histologic parameters, including axon density. Some level of correlation is expected since MD and RD were shown to be sensitive to changes in myelination and other microstructural changes. Figures 3.10 and 3.11 showed that DKI parameters MK and RK exhibited strong correlations with myelin content and other histologic measures, such as axon density and g-ratio. Not only were DKI metrics more sensitive to changes in myelination compared with DTI as shown by the ROI analysis, but they also exhibited stronger correlations to myelin content than conventional DTI. MK and RK showed significant correlations with each metric examined except for myelin thickness, indicating the limited specificity of these DKI measures. However, their correlations with myelin-related metrics (e.g., myelin fraction, g-ratio) were stronger than those shown with axon diameter, a measure that is mostly independent of myelin content.

Myelin is not explicitly modeled by the DKI framework, yet these results indicate that a strong relationship exists between DKI metrics and myelin content. This is not to say that DKI metrics are or should be more specific to myelin compared with other MR measures that explicitly model myelin, such as MWF and PSR. However, reporting on myelin content is just one potential use for DKI among others due to its high microstructural sensitivity and relative ease of acquisition.

Figures 3.12 and 3.13 showed that WMTI metric F_a correlated strongly with myelin content and other histologic measures, such as axon density, axon fraction, and g-ratio. The correlation with axon density and fraction is in agreement with previous work stating that F_a reports on axonal loss (Fieremans et al., 2012a). Whereas the correlations with axon density and axon fraction are intuitive, the correlation with myelin fraction is not straightforward. In this study, a decrease in myelinated axon density is the main component of both decreased axon fraction and myelin fraction, which explains the close relationship between F_a and f_m. Although Fig. 3.13 suggests that F_a overestimated the true axon fraction by ~50%, note that F_a in the WMTI model is axon water fraction and the myelin water is presumed silent in DWI due to its short T_2. Comparing F_a to $f_a/(1-f_m)$ (not shown), we see that F_a overestimated axon water fraction by only ~10% in control and Rictor mice, making it a reasonably accurate model parameter for small variations from normal. For TSC mice, which histology showed to have near zero myelinated axons, F_a clearly overestimates the water fraction of myelinated axons; however, if unmyelinated axons were also included in this analysis, the correspondence might be closer.

In contrast, $D_{e,\perp}$ did not correlate with the other myelin measures utilized in this study (Fig. 3.12). Previous work by Fieremans and coworkers (Fieremans et al., 2012a) suggested that $D_{e,\perp}$ reports on changes in myelin thickness, even in the presence of axonal loss. Even though the

main difference between the control and CKO groups was a decrease in myelinated axon density, significant decreases in myelin thickness were also present and should have caused increases in $D_{e,\perp}$ in both the Rictor and TSC groups based on this previous hypothesis. However, $D_{e,\perp}$ did not correlate with myelin thickness and was not especially sensitive to microstructural changes between the control and CKO groups. Also, from the correlation plots in Figs. 3.8-3.13, it was shown that there were some deviations in DWI metrics between WM regions (e.g., higher MK and RK in the genu of the control mouse brains, represented by the green dots) that were not explained by any one histological parameter used in this study, suggesting other microstructural contributions to these measures.

Although potentially useful for elucidating the relationship between DKI and tissue microstructure, previous comparisons of DKI and associated metrics with histological measures have been limited. One study compared DKI metrics to myelin basic protein immunohistochemistry in a Huntington's disease rat model at two different developmental ages, observing that increases in myelin basic protein stain intensity corresponded with decreases in MD and RD and increases in MK and RK (Blockx et al., 2012). Another study examined the relationship between both DKI and WMTI with immunohistochemistry metrics in a cuprizone mouse model of demyelination, finding that solochrome staining (a stain for myelin) correlated with MK, AK, RK, F_a, D_a, and $D_{e,\perp}$ in the cuprizone group (Falangola et al., 2014). However, there have been no previous comparisons of DKI or WMTI to direct quantitative histologic measures of axons and myelin content, such as axon diameter, myelin thickness, and histologic myelin fraction. Similar to this work, previous studies have compared DTI metrics FA and RD with myelin measures derived from MET_2 and qMT and found modest correlations between these measures (Mädler et al., 2008; Stikov et al., 2011; Thiessen et al., 2013). However, there

have been no prior studies assessing DKI or WMTI metrics in white matter through comparisons with other MR metrics specific to myelin, such as myelin water fraction and macromolecular pool-size ratio. Although histological analysis is difficult and can be susceptible to a variety of error sources, general agreement between the comparisons of DWI metrics with histology, MWF, and PSR support the histological analysis in this study.

In addition to increased sensitivity to changes in WM microstructure, DKI has the potential for improved tractography compared with conventional DTI. Recent work by Jensen and coworkers (Jensen et al., 2013) demonstrated that tractography based on the kurtosis diffusion orientation distribution function (kurtosis dODF) derived from the kurtosis tensor has enhanced ability to resolve crossing fibers over tractography based on the diffusion tensor alone. Using this approach, various DWI metrics could feasibly be computed for different fiber populations within the same voxel. Additionally, DKI-based tractography could possibly enable the application of the WMTI model in regions with crossing fibers. Although crossing fibers are not as prevalent in this mouse brain study, they remain a significant issue in DWI of the human brain, making DKI-based tractography another significant advantage of DKI over DTI in white matter assessment.

There are certain limitations to using diffusion signal models such as DTI and DKI to describe white matter microstructure. Although DKI is sensitive to tissue heterogeneity within a voxel, particularly the mixture of restricted and unrestricted water compartments; the DKI model does not specifically characterize multiple tissue compartments present within white matter. On the other hand, multi-compartment tissue models of diffusion, such as CHARMED (Assaf et al., 2004), AxCaliber (Assaf et al., 2008), ActiveAx (Alexander et al., 2010), NODDI (H. Zhang et al., 2012), and WMTI, seek to derive specific information about tissue components such as intra-

and extracellular spaces, axon diameter, axon alignment, axon density, and myelin content. However, these biophysical tissue models each come with their own limitations and biases because they require assumptions about the underlying tissue composition and generally result in lower precision parameters resulting from fitting data to nonlinear models. It remains an open question as to whether signal-based or tissue-based diffusion models provide better assessment of tissue microstructure from a practical standpoint. For this study, application of the biophysical WMTI model provided good estimates of axonal water fraction for control and Rictor mice, but did not provide additional specificity to myelination.

Although the WMTI model does not explicitly incorporate myelin, previous studies have hypothesized its relationship to myelin content (Benitez et al., 2014; Falangola et al., 2014; Fieremans et al., 2012a). This hypothesis is formed on the idea that the presence of myelin will have an effect on the tortuosity of the extra-axonal space or more specifically, the diffusion of extra-axonal water perpendicular to the axons ($D_{e,\perp}$). Other multi-compartment diffusion models, including CHARMED, AxCaliber, ActiveAx, and NODDI (Alexander et al., 2010; Assaf et al., 2008; Assaf et al., 2004; H. Zhang et al., 2012), do not explicitly model myelin, yet they also measure or incorporate the extracellular tortuosity as a part of the model. However, the WMTI model is the first of these used to make inferences concerning myelin content. Unexpectedly, in this study, $D_{e,\perp}$ did not demonstrate correlations with myelin content, bringing into question its utility as a biomarker of myelination.

For this study, the histology measures collected were primarily focused on changes in myelin due to the expected changes observed in the CKO mice. It was shown that axial DWI metrics remained mostly unchanged in these models, as expected. Therefore, a different animal model demonstrating changes in axon microstructure would be more appropriate for the

assessment of axial DWI measures. One microstructural feature not measured in this study that is potentially important in determining DWI contrast is the extra-axonal space fraction. This metric is difficult to measure from EM because it is small and not easily discriminated from unmyelinated axon space. For this study we postulate that it is not a critical factor in determining differences in the DWI measures because neither the TSC nor Rictor model is expected to involve much inflammation.

It is also important to recognize that this MR study was performed on *ex vivo* mouse brain. *Ex vivo* tissue has been shown to exhibit decreased diffusivity and increased kurtosis due to chemical fixation (Hui et al., 2008; Sun et al., 2003). Additionally, the choice of fixative has been shown to have an effect on the relaxation and diffusion properties of tissue (Shepherd et al., 2009), and tissue preparation may result in shrinking or distortion that can influence the derived histological measures (Fox et al., 1985). Thus, one should be cautious about using the findings here to interpret *in vivo* measures of diffusion and kurtosis in white matter.

Comparison between MR metrics and EM-derived histology metrics also has inherent limitations. Matching up ROIs between the two imaging modalities is a difficult process, so utilizing anatomical landmarks that are clearly visible from both the MR image and the histology thick section is important. Even if the ROI is matched with high accuracy, the thickness of the histology section is still much smaller than the MR imaging resolution, which prevents an exact correspondence of the microstructure morphology present in the EM data with that contained in an MR voxel. Also, it is important to note that, for this study, the total FOV sampled for each EM section is still a small fraction of the size of a single MR voxel, so the intra-tract variability must be considered when choosing the amount of EM data required for comparison to MR data.

Selection of appropriate b-values is especially important for DKI studies. Higher b-values than those used in conventional *in vivo* DTI are necessary in this study both due to the use of *ex vivo* tissue and to increase sensitivity of the DWI signal to kurtosis. However, the maximum b-value used must also be carefully determined, as using too high of b-values can cause systematic errors in DKI metrics (Jensen and Helpern, 2010). The wide range of diffusivity and kurtosis values present in *ex vivo* mouse brain make b-value optimization difficult, and in this study for example, there were still some voxels in the genu that needed even larger b-values for more accurate assessment of DKI and WMTI metrics.

3.5 Conclusions

DKI was demonstrated to have greater sensitivity to changes in myelination compared with conventional DTI. Additionally, through comparisons with other MR measures of myelin and quantitative histology, DKI metrics MK and RK were shown to have stronger correlations with myelin content compared with DTI metrics. Thus, if sufficient time is available for the acquisition of two shells of DWI data, then DKI is preferred over DTI because it provides greater sensitivity to changes in tissue microstructure. Application of the biophysical WMTI model provided reasonably accurate estimates of axon water fraction for near normal microstructure, but the associated extra-axonal diffusion characteristics did not report on any measure of myelination.

3.6 Acknowledgements

Portions of this chapter were previously published in NeuroImage (Kelm et al., 2016). The author thanks Brittany Parker for technical assistance with animal husbandry, Sophia Swago for

assistance with EM measurements, and Janice Williams, Ph.D., of the VUMC Cell Imaging Shared Resource for assistance with microscopy. Processing of EM sections and EM image collection were performed through the use of the VUMC Cell Imaging Shared Resource, supported by NIH grants CA68485, DK20593, DK58404, HD15052, DK59637, and EY008126. This work was also supported by NIH grants R01 EB001744, T32 EB014841, 5K08 NS050484, and S10 RR029523.

3.7 Appendix: Supplemental Figures

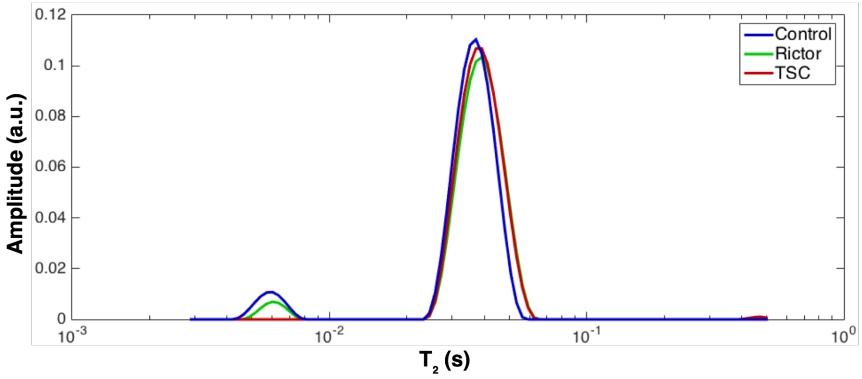

FIG. 3.14. Representative white matter T_2 spectra. T_2 spectra from a single MidCC voxel for the control (blue), Rictor (green), and TSC (red) groups. For this voxel, the TSC T_2 spectrum does not have a short T_2 component, indicating a negligible MWF.

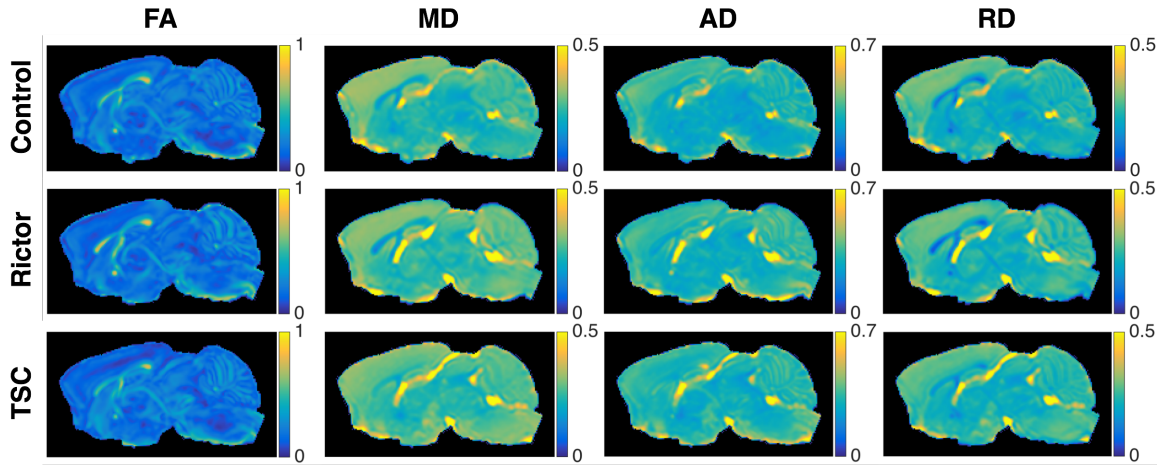

FIG. 3.15. Representative sagittal DTI parameter maps. The rows represent the three groups: control (top), Rictor (middle), and TSC (bottom). The columns represent the DTI parameters FA, MD, AD, and RD. FA is unitless and diffusivities are in units of $\mu m^2/ms$.

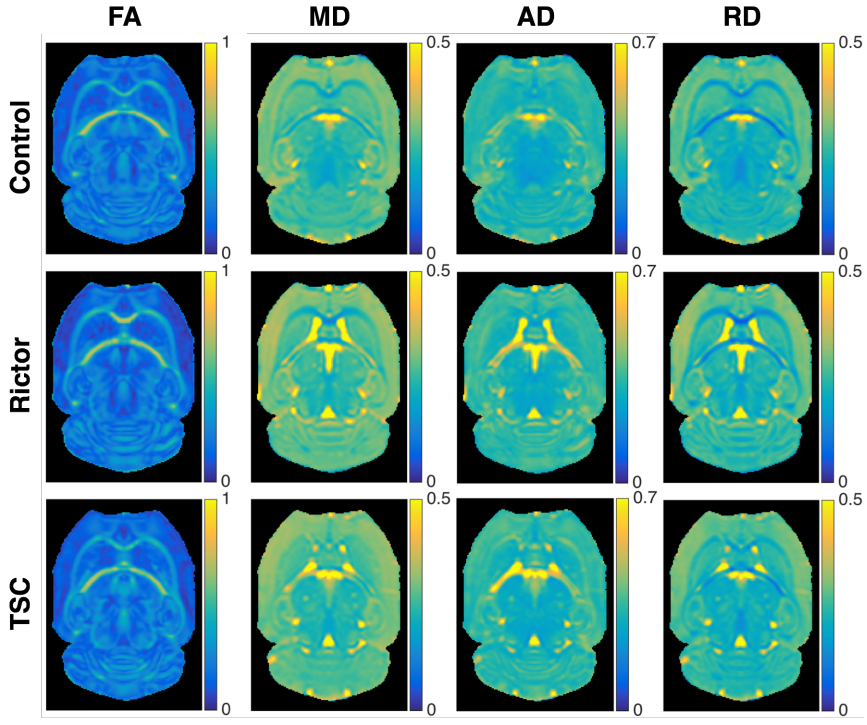

FIG. 3.16. Representative axial DTI parameter maps. The rows represent the three groups: control (top), Rictor (middle), and TSC (bottom). The columns represent the DTI parameters FA, MD, AD, and RD. FA is unitless and diffusivities are in units of $\mu m^2/ms$.

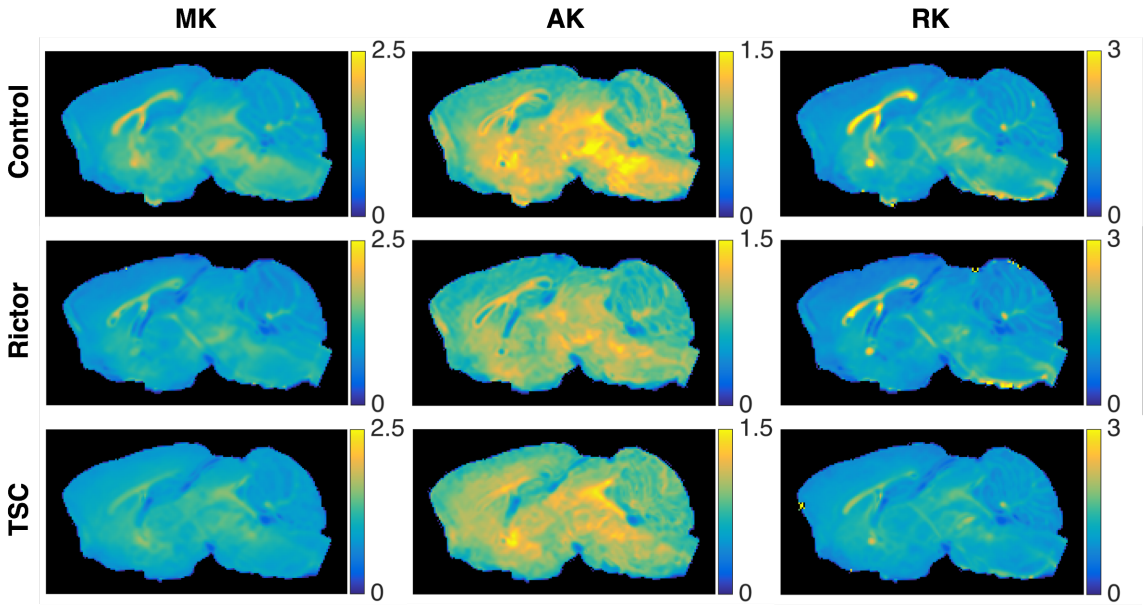

FIG. 3.17. Representative sagittal DKI parameter maps. The rows represent the three groups: control (top), Rictor (middle), and TSC (bottom). The columns represent the DKI parameters MK, AK, and RK. Kurtosis is unitless.

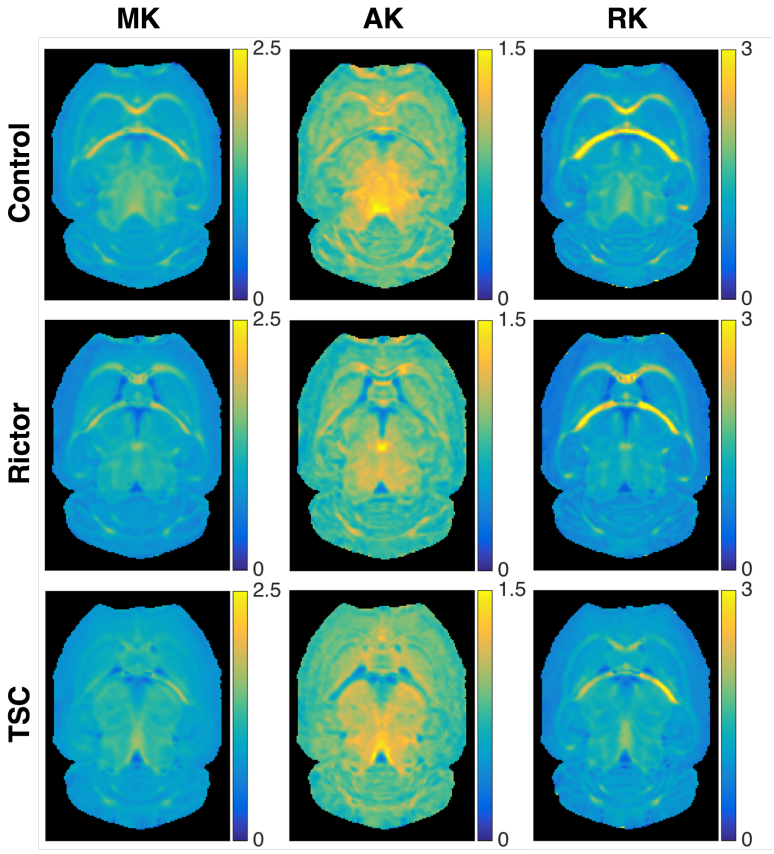

FIG. 3.18. Representative axial DKI parameter maps. The rows represent the three groups: control (top), Rictor (middle), and TSC (bottom). The columns represent the DKI parameters MK, AK, and RK. Kurtosis is unitless.

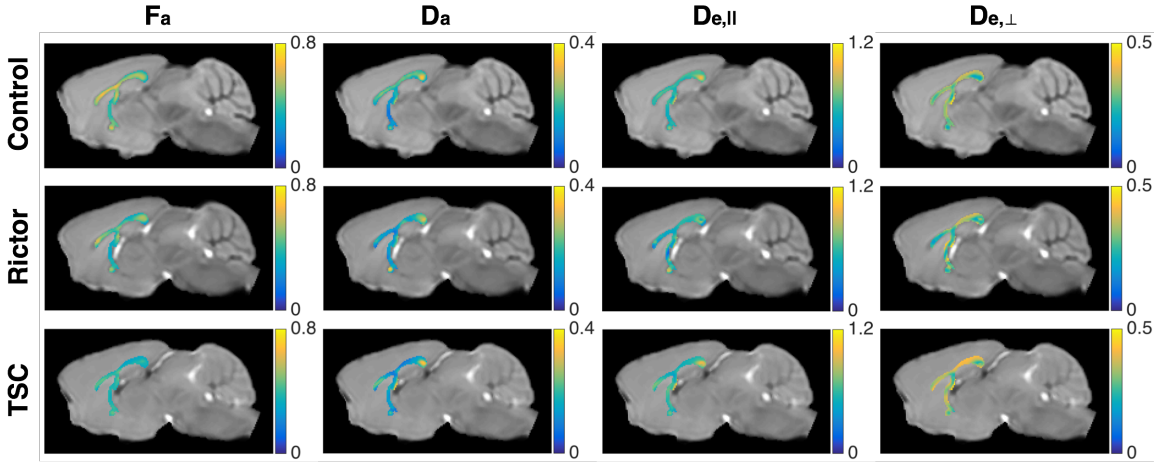

FIG. 3.19. Representative sagittal WMTI parameter maps. WMTI parameter values for white matter voxels are overlaid on the b=0 image. The rows represent the three groups: control (top), Rictor (middle), and TSC (bottom). The columns represent the WMTI parameters F_a, D_a, $D_{e,\parallel}$, and $D_{e,\perp}$. F_a is unitless and diffusivities are in units of $\mu m^2/ms$.

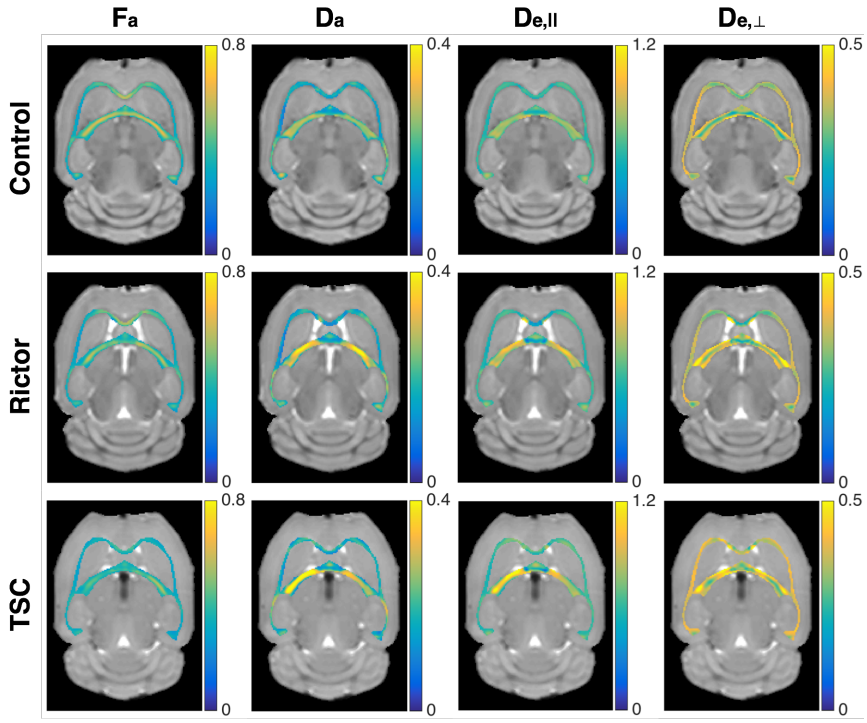

FIG. 3.20. Representative axial WMTI parameter maps. WMTI parameter values for white matter voxels are overlaid on the b=0 image. The rows represent the three groups: control (top), Rictor (middle), and TSC (bottom). The columns represent the WMTI parameters F_a, D_a, $D_{e,||}$, and $D_{e,\perp}$. F_a is unitless and diffusivities are in units of $\mu m^2/ms$.

3.8 References

Alexander, D.C., Hubbard, P.L., Hall, M.G., Moore, E.A., Ptito, M., Parker, G.J.M., Dyrby, T.B., 2010. Orientationally invariant indices of axon diameter and density from diffusion MRI. NeuroImage 52, 1374–1389. doi: 10.1016/j.neuroimage.2010.05.043

Allen, I.V., McKeown, S.R., 1979. A histological, histochemical and biochemical study of the macroscopically normal white matter in multiple sclerosis. J. Neurol. Sci. 41, 81–91.

Assaf, Y., Blumenfeld-Katzir, T., Yovel, Y., Basser, P.J., 2008. AxCaliber: a method for measuring axon diameter distribution from diffusion MRI. Magn. Reson. Med. 59, 1347–1354. doi: 10.1002/mrm.21577

Assaf, Y., Freidlin, R.Z., Rohde, G.K., Basser, P.J., 2004. New modeling and experimental framework to characterize hindered and restricted water diffusion in brain white matter. Magn. Reson. Med. 52, 965–978.

Basser, P.J., Jones, D.K., 2002. Diffusion-tensor MRI: theory, experimental design and data

analysis–a technical review. NMR Biomed. 15, 456–467.

Basser, P.J., Mattiello, J., LeBihan, D., 1994a. Estimation of the effective self-diffusion tensor from the NMR spin echo. J. Magn. Reson. Ser. B 103, 247–254.

Basser, P.J., Mattiello, J., LeBihan, D., 1994b. MR diffusion tensor spectroscopy and imaging. Biophys. J. 66, 259–267.

Beaulieu, C., 2002. The basis of anisotropic water diffusion in the nervous system–a technical review. NMR Biomed. 15, 435–455. doi: 10.1002/nbm.782

Benitez, A., Fieremans, E., Jensen, J.H., Falangola, M.F., Tabesh, A., Ferris, S.H., Helpern, J.A., 2014. White matter tract integrity metrics reflect the vulnerability of late-myelinating tracts in Alzheimer's disease. NeuroImage Clin. 4, 64–71. doi: 10.1016/j.nicl.2013.11.001

Blockx, I., De Groof, G., Verhoye, M., Van Audekerke, J., Raber, K., Poot, D., Sijbers, J., Osmand, A.P., Von Hörsten, S., Van der Linden, A., 2012. Microstructural changes observed with DKI in a transgenic Huntington rat model: evidence for abnormal neurodevelopment. NeuroImage 59, 957–967.

Carson, R.P., Fu, C., Winzenburger, P., Ess, K.C., 2013. Deletion of Rictor in neural progenitor cells reveals contributions of mTORC2 signaling to tuberous sclerosis complex. Hum. Mol. Gen. 22, 140–152. doi: 10.1093/hmg/dds414

Carson, R.P., Van Nielen, D.L., Winzenburger, P.A., Ess, K.C., 2012. Neuronal and glia abnormalities in Tsc1-deficient forebrain and partial rescue by rapamycin. Neurobiol. Dis. 45, 369–380. doi: 10.1016/j.nbd.2011.08.024

Cheung, M.M., Hui, E.S., Chan, K.C., Helpern, J.A., Qi, L., Wu, E.X., 2009. Does diffusion kurtosis imaging lead to better neural tissue characterization? A rodent brain maturation study. NeuroImage 45, 386–392. doi: 10.1016/j.neuroimage.2008.12.018

Davis, K.L., Stewart, D.G., Friedman, J.I., Buchsbaum, M., Harvey, P.D., Hof, P.R., Buxbaum, J., Haroutunian, V., 2003. White matter changes in schizophrenia: evidence for myelin-related dysfunction. Arch. Gen. Psychiat. 60, 443–456. doi: 10.1001/archpsyc.60.5.443

Falangola, M.F., Guilfoyle, D.N., Tabesh, A., Hui, E.S., Nie, X., Jensen, J.H., Gerum, S.V., Hu, C., LaFrancois, J., Collins, H.R., Helpern, J.A., 2014. Histological correlation of diffusional kurtosis and white matter modeling metrics in cuprizone-induced corpus callosum demyelination. NMR Biomed. 27, 948–957. doi: 10.1002/nbm.3140

Fieremans, E., Benitez, A., Jensen, J.H., Falangola, M.F., Tabesh, A., Deardorff, R.L., Spampinato, M.V.S., Babb, J.S., Novikov, D.S., Ferris, S.H., Helpern, J.A., 2013. Novel white matter tract integrity metrics sensitive to Alzheimer disease progression. AJNR Am. J. Neuroradiol. 34, 2105–2112. doi: 10.3174/ajnr.A3553

Fieremans, E., Jensen, J.H., Helpern, J.A., Kim, S., Grossman, R., Inglese, M., 2012a. Diffusion distinguishes between axonal loss and demyelination in brain white matter. 20th Annual Meeting of the International Society for Magnetic Resonance in Medicine. Melbourne, Australia. 465.

Fieremans, E., Jensen, J.H., Hui, E.S., Novikov, D.S., Tabesh, A., Bonilha, L., 2012b. Direct evidence for decreased intra-axonal diffusivity in ischemic human stroke. 20th Annual Meeting of the International Society for Magnetic Resonance in Medicine. Melbourne, Australia. 3600.

Fieremans, E., Jensen, J.H., Helpern, J.A., 2011. White matter characterization with diffusional kurtosis imaging. NeuroImage 58, 177–188. doi: 10.1016/j.neuroimage.2011.06.006

Fox, C.H., Johnson, F.B., Whiting, J., Roller, P.P., 1985. Formaldehyde fixation. J. Histochem. Cytochem. 33, 845–853.

Gochberg, D.F., Gore, J.C., 2007. Quantitative magnetization transfer imaging via selective inversion recovery with short repetition times. Magn. Reson. Med. 57, 437–441.

Helpern, J.A., Adisetiyo, V., Falangola, M.F., Hu, C., Di Martino, A., Williams, K., Castellanos, F.X., Jensen, J.H., 2011. Preliminary evidence of altered gray and white matter microstructural development in the frontal lobe of adolescents with attention-deficit hyperactivity disorder: a diffusional kurtosis imaging study. J. Magn. Reson. Imaging 33, 17–23. doi: 10.1002/jmri.22397

Hui, E.S., Fieremans, E., Jensen, J.H., Tabesh, A., Feng, W., Bonilha, L., Spampinato, M.V., Adams, R., Helpern, J.A., 2012. Stroke assessment with diffusional kurtosis imaging. Stroke 43, 2968–2973. doi: 10.1161/STROKEAHA.112.657742

Hui E.S., Cheung M.M., Qi L, Wu E.X., 2008. Towards better MR characterization of neural tissues using directional diffusion kurtosis analysis. NeuroImage 42, 122-134.

Jensen, J.H., Helpern, J.A., Tabesh, A., 2013. Leading non-Gaussian corrections for diffusion orientation distribution function. NMR Biomed. 27, 202–211. doi: 10.1002/nbm.3053

Jensen, J.H., Helpern, J.A., 2010. MRI quantification of non-Gaussian water diffusion by kurtosis analysis. NMR Biomed. 23, 698–710. doi: 10.1002/nbm.1518

Jensen, J.H., Helpern, J.A., Ramani, A., Lu, H., Kaczynski, K., 2005. Diffusional kurtosis imaging: The quantification of non-gaussian water diffusion by means of magnetic resonance imaging. Magn. Reson. Med. 53, 1432–1440. doi: 10.1002/mrm.20508

Kelm, N.D., West, K.L., Carson, R.P., Gochberg, D.F., Ess, K.C., Does, M.D., 2016. Evaluation of diffusion kurtosis imaging in ex vivo hypomyelinated mouse brains. NeuroImage 124, 612–626. doi: 10.1016/j.neuroimage.2015.09.028

Koenig, S.H., Brown, R.D., Spiller, M., Lundbom, N., 1990. Relaxometry of brain: why white matter appears bright in MRI. Magn. Reson. Med. 14, 482–495.

Kucharczyk, W., Macdonald, P.M., Stanisz, G.J., Henkelman, R.M., 1994. Relaxivity and magnetization transfer of white matter lipids at MR imaging: importance of cerebrosides and pH. Radiology 192, 521–529.

Landman, B.A., Farrell, J.A., Jones, C.K., Smith, S.A., Prince, J.L., Mori, S., 2007. Effects of diffusion weighting schemes on the reproducibility of DTI-derived fractional anisotropy, mean diffusivity, and principal eigenvector measurements at 1.5 T. NeuroImage 36, 1123–1138.

Le Bihan, D., Mangin, J.F., Poupon, C., Clark, C.A., Pappata, S., Molko, N., Chabriat, H., 2001. Diffusion tensor imaging: concepts and applications. J. Magn. Reson. Imaging. 13, 534–546.

Lee, C.-Y., Tabesh, A., Benitez, A., Helpern, J.A., Jensen, J.H., Bonilha, L., 2013. Microstructural integrity of early-versus late-myelinating white matter tracts in medial temporal lobe epilepsy. Epilepsia 54, 1801–1809.

Lu, H., Jensen, J.H., Ramani, A., Helpern, J.A., 2006. Three-dimensional characterization of non-gaussian water diffusion in humans using diffusion kurtosis imaging. NMR Biomed. 19, 236–247. doi: 10.1002/nbm.1020

MacKay, A., Whittall, K., Adler, J., Li, D., Paty, D., Graeb, D., 1994. In vivo visualization of myelin water in brain by magnetic resonance. Magn. Reson. Med. 31, 673–677.

Mädler, B., Drabycz, S.A., Kolind, S.H., Whittall, K.P., MacKay, A.L., 2008. Is diffusion anisotropy an accurate monitor of myelination?: Correlation of multicomponent T2 relaxation and diffusion tensor anisotropy in human brain. Magn. Reson. Imaging 26, 874–888.

Mason, J.L., Langaman, C., Morell, P., Suzuki, K., Matsushima, G.K., 2001. Episodic demyelination and subsequent remyelination within the murine central nervous system: changes in axonal calibre. Neuropath. Appl. Neuro. 27, 50–58.

Menon, R.S., Rusinko, M.S., Allen, P.S., 1992. Proton relaxation studies of water compartmentalization in a model neurological system. Magn. Reson. Med. 28, 264–274.

Neeman, M., Freyer, J.P., Sillerud, L.O., 1991. A simple method for obtaining cross-term-free images for diffusion anisotropy studies in NMR microimaging. Magn. Reson. Med. 21, 138–143.

Paxinos, G., Franklin, K.B., 2004. The mouse brain in stereotaxic coordinates. Gulf Professional Publishing.

Ramani, A., Jensen, J.H., Szulc, K.U., Ali, O., Hu, C., Lu, H., Brodle, J.D., Helpern, J.A., 2007.

Assessment of abormalities in the cerebral microstructure of schizophrenia patients: a diffusional kurtosis imaging study. 15th Annual Meeting of the International Society for Magnetic Resonance in Medicine. Berlin, Germany. 648.

Shepherd, T.M., Thelwall, P.E., Stanisz, G.J., Blackband, S.J., 2009. Aldehyde fixative solutions alter the water relaxation and diffusion properties of nervous tissue. Magn. Reson. Med. 62, 26–34. doi: 10.1002/mrm.21977

Sled, J.G., Pike, G.B., 2000. Quantitative interpretation of magnetization transfer in spoiled gradient echo MRI sequences. J. Magn. Reson. 145, 24–36. doi: 10.1006/jmre.2000.2059

Song, S.-K., Sun, S.-W., Ramsbottom, M.J., Chang, C., Russell, J., Cross, A.H., 2002. Dysmyelination revealed through MRI as increased radial (but unchanged axial) diffusion of water. NeuroImage 17, 1429–1436. doi: 10.1006/nimg.2002.1267

Song, S.-K., Yoshino, J., Le, T.Q., Lin, S.-J., Sun, S.-W., Cross, A.H., Armstrong, R.C., 2005. Demyelination increases radial diffusivity in corpus callosum of mouse brain. NeuroImage 26, 132–140. doi: 10.1016/j.neuroimage.2005.01.028

Stikov, N., Perry, L.M., Mezer, A., Rykhlevskaia, E., Wandell, B.A., Pauly, J.M., Dougherty, R.F., 2011. Bound pool fractions complement diffusion measures to describe white matter micro and macrostructure. NeuroImage 54, 1112–1121.

Sun, S.-W., Neil, J.J., Song, S.-K., 2003. Relative indices of water diffusion anisotropy are equivalent in live and formalin-fixed mouse brains. Magn. Reson. Med. 50, 743–748.

Sun, S.-W., Liang, H.F., Trinkaus, K., Cross, A.H., Armstrong, R.C., Song, S.-K., 2006. Noninvasive detection of cuprizone induced axonal damage and demyelination in the mouse corpus callosum. Magn. Reson. Med. 55, 302-308.

Thiessen, J.D., Zhang, Y., Zhang, H., Wang, L., Buist, R., Del Bigio, M.R., Kong, J., Li, X.-M., Martin, M., 2013. Quantitative MRI and ultrastructural examination of the cuprizone mouse model of demyelination. NMR Biomed. 26, 1562–1581. doi: 10.1002/nbm.2992

Thirion, J.P., 1998. Image matching as a diffusion process: an analogy with Maxwell's demons. Med. Image Anal. 2, 243–260.

Wu, E.X., Cheung, M.M., 2010. MR diffusion kurtosis imaging for neural tissue characterization. NMR Biomed. 23, 836–848. doi: 10.1002/nbm.1506

Zhang, H., Schneider, T., Wheeler-Kingshott, C.A., Alexander, D.C., 2012. NODDI: practical in vivo neurite orientation dispersion and density imaging of the human brain. NeuroImage 61, 1000–1016.

Zhang, J., Jones, M.V., McMahon, M.T., Mori, S., Calabresi, P.A., 2012. In vivo and ex vivo diffusion tensor imaging of cuprizone-induced demyelination in the mouse corpus callosum.

Magn. Reson. Med. 67, 750–759. doi: 10.1002/mrm.23032

CHAPTER 4

DIFFUSION KURTOSIS IMAGING IN HYPERMYELINATED MOUSE BRAIN

4.1 Introduction

This chapter presents a brief extension to the work described in Chapter 3, and portions of these data are also shown as part of a larger study on brain development in Chapter 5. The objective of this work was to evaluate DTI, DKI, and WMTI metrics in a transgenic hypermyelinated CKO mouse model, in contrast to the hypomyelinated mouse models utilized in the previous chapter, to determine whether an increase in myelination would have an opposite effect on DWI parameters than that observed in the hypomyelinated mice. The mouse model, *Pten* Olig2-Cre CKO (PTEN), is related to PI3K signaling and has been previously shown to exhibit hypermyelination (Harrington et al., 2010). Examining these DWI metrics in this case of hypermyelination may lead to improved understanding of the relationship between DWI and myelination.

4.2 Materials and Methods

For this study, 8 control and 7 PTEN adult female P60 mice were used. Animal preparation and MR imaging and analysis procedures were exactly as stated in section 2.1. Again, it should be noted that DWI data with b = 9000 s/mm^2 were not included in any analyses so that direct comparisons could be made with the previously acquired control group data. For histological evaluation, normal (N = 6) and PTEN (N = 3) mouse brains were sectioned and four white matter regions were analyzed: midbody of the corpus callosum (MidCC), genu (GCC), splenium

(SCC), and anterior commissure (AC), matching the ROIs used in the hypomyelination study (see Section 2.1.4.1). Acquisition and analysis of EM data were performed using the methods described in Section 2.1.4.2. It is important to note that the histologic axon fraction reported in this study is computed with the exclusion of myelin, in order to provide direct comparison with the axonal water fraction derived from WMTI.

For DWI group analysis, b=0 images were registered to a representative control mouse brain using FSL's (FMRIB Analysis Group, Oxford, UK) linear (FLIRT) and non-linear (FNIRT) registration tools (Andersson et al., 2007; Jenkinson et al., 2002; Jenkinson and Smith, 2001; Smith et al., 2004). DTI, DKI, and WMTI parameter maps were then registered using the same transformations derived from the b=0 registration. Referencing a standard mouse brain atlas (Paxinos and Franklin, 2004), ROIs were drawn in the MidCC, GCC, SCC, AC, as well as the external and internal capsules (EC and IC, respectively), again matching the ROIs used in Chapter 3.

Table 4.1. Group mean ± SEM of quantitative EM histology measures for control and PTEN groups at age P60.

		f_m	f_a	d_a (μm)	z_m (nm)	g	ρ_a (axons/μm)
MidCC	Control	0.204 ± 0.012	0.443 ± 0.038	0.522 ± 0.026	87.0 ± 2.9	0.721 ± 0.008	1.124 ± 0.079
	PTEN	0.213 ± 0.031	0.365 ± 0.068	0.526 ± 0.050	109.7 ± 10.9*	0.674 ± 0.017*	0.860 ± 0.128*
GCC	Control	0.226 ± 0.013	0.510 ± 0.034	0.550 ± 0.024	89.9 ± 2.2	0.723 ± 0.011	1.097 ± 0.076
	PTEN	0.217 ± 0.028	0.443 ± 0.069	0.585 ± 0.046	102.1 ± 4.8*	0.710 ± 0.016	0.839 ± 0.114*
SCC	Control	0.225 ± 0.015	0.476 ± 0.040	0.518 ± 0.019	87.5 ± 1.9	0.724 ± 0.010	1.210 ± 0.072
	PTEN	0.264 ± 0.035	0.451 ± 0.078	0.528 ± 0.039	109.4 ± 6.4*	0.687 ± 0.015*	1.038 ± 0.110
AC	Control	0.232 ± 0.016	0.447 ± 0.035	0.566 ± 0.031	94.9 ± 2.7	0.730 ± 0.011	1.078 ± 0.098
	PTEN	0.275 ± 0.019*	0.471 ± 0.039	0.651 ± 0.035*	120.5 ± 7.2*	0.718 ± 0.009	0.803 ± 0.059*

Significant differences compared with the control group are indicated by * ($p \leq 0.05$).

4.3 Results

Table 4.1 shows the group means and standard errors of histology measures for each ROI, with significant differences identified by * ($p < 0.05$, with Bonferroni correction). The PTEN model showed significant increases in myelin thickness, along with decreases in g-ratio and myelinated axon density. Despite the large increase in myelin thickness, the PTEN only showed a slightly increased histologic myelin fraction, due to the lower axon density. Generally, axon fraction in the PTEN model was slightly decreased as well, although these changes were not significant. The PTEN group exhibited similar mean axon diameter compared to the control group, although it was significantly greater in the AC.

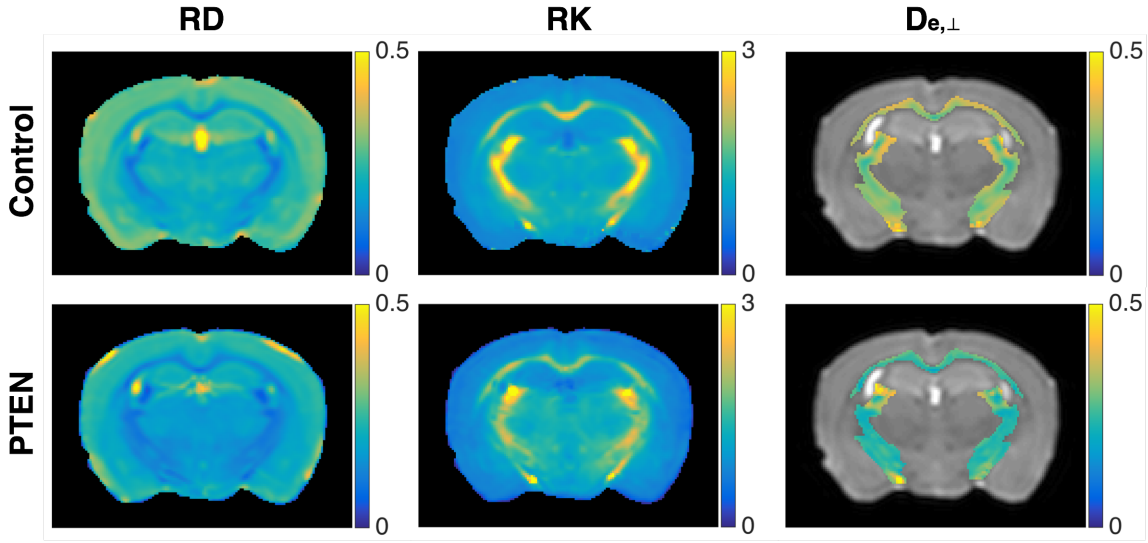

FIG. 4.1. Group-averaged DWI parameter maps. The rows represent the two groups: control (top) and PTEN (bottom). The columns represent the DWI parameters RD, RK, and $D_{e,\perp}$. RK is unitless and diffusivities are in units of $\mu m^2/ms$.

Group-averaged parameter maps for radial-based measures RD, RK, and $D_{e,\perp}$, due to their previous associations with myelination, are displayed in Fig. 4.1. Based on these maps, there was an apparent decrease in RD present in both gray matter and white matter for the PTEN group

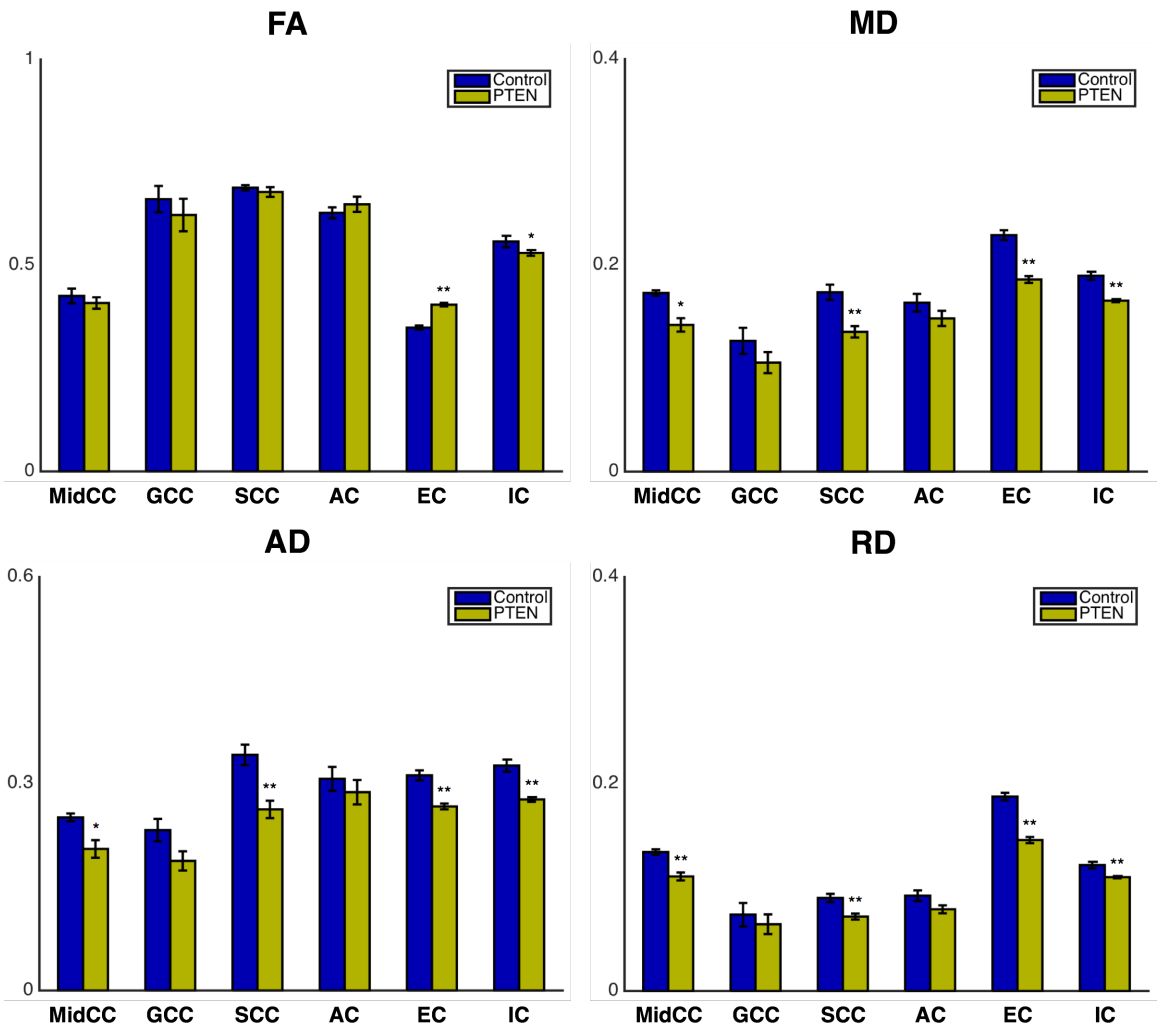

FIG. 4.2. ROI group comparison of DTI parameters FA, MD, AD, and RD. Bar heights represent the ROI parameter means across each group, with error bars spanning the mean ± SEM. The two groups are represented with different colors: control = blue and PTEN = yellow. 6 WM ROIs are indicated on the x-axis: MidCC = midbody of the corpus callosum, GCC = genu, SCC = splenium, AC = anterior commissure, EC = external capsule, and IC = internal capsule. FA is unitless and diffusivities are in units of $\mu m^2/ms$. * denotes $p < 0.05$ and ** denotes $p < 0.01$ for comparison between the control group and the PTEN group.

compared with the control brains. However, RK seems to be slightly decreased as well, therefore not exhibiting the usually opposing trend compared to RD. Visually, the PTEN model also exhibits lower $D_{e,\perp}$ compared to the control group.

The results of the group ROI analysis for DTI metrics FA, MD, AD, and RD are shown in Fig. 4.2. Generally, there were minimal differences in FA between the two groups. However, significant decreases in MD, AD, and RD were observed in the MidCC, SCC, EC, and IC for the PTEN model compared with the control group. Decreases in each of these metrics were also seen

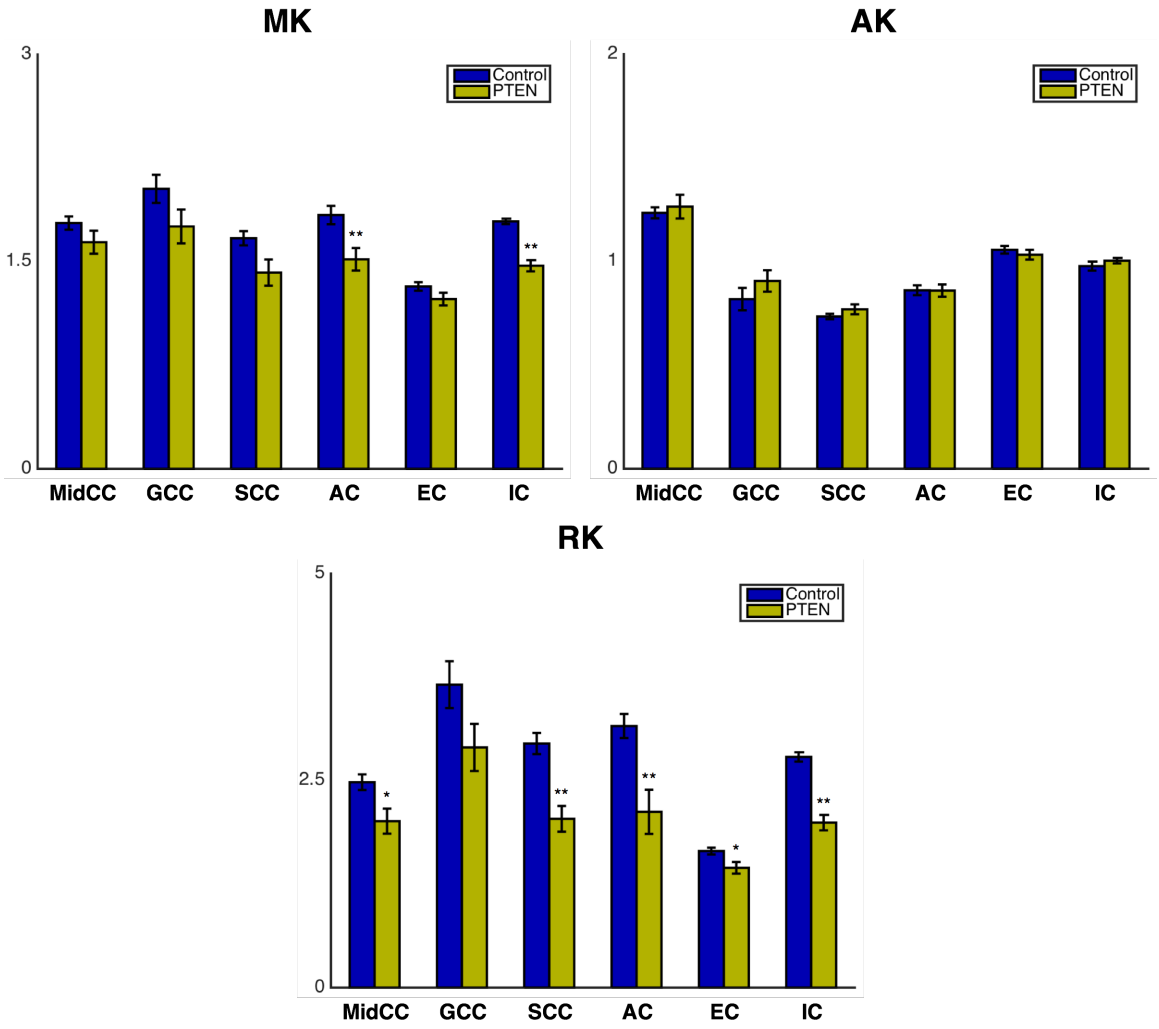

FIG. 4.3. ROI group comparison of DKI parameters MK, AK, and RK. Bar heights represent the ROI parameter means across each group, with error bars spanning the mean ± SEM. The two groups are represented with different colors: control = blue and PTEN = yellow. 6 WM ROIs are indicated on the x-axis: MidCC = midbody of the corpus callosum, GCC = genu, SCC = splenium, AC = anterior commissure, EC = external capsule, and IC = internal capsule. Kurtosis is unitless. * denotes $p < 0.05$ and ** denotes $p < 0.01$ for comparison between the control group and the PTEN group.

in the GCC and AC, yet these changes were not significant.

Fig. 4.3 shows bar graphs representing the group ROI means for DKI parameters MK, AK, and RK. Reduced MK for the PTEN model was shown in all white matter regions, although these changes were only significant in the AC and IC. Both groups exhibited similar AK across

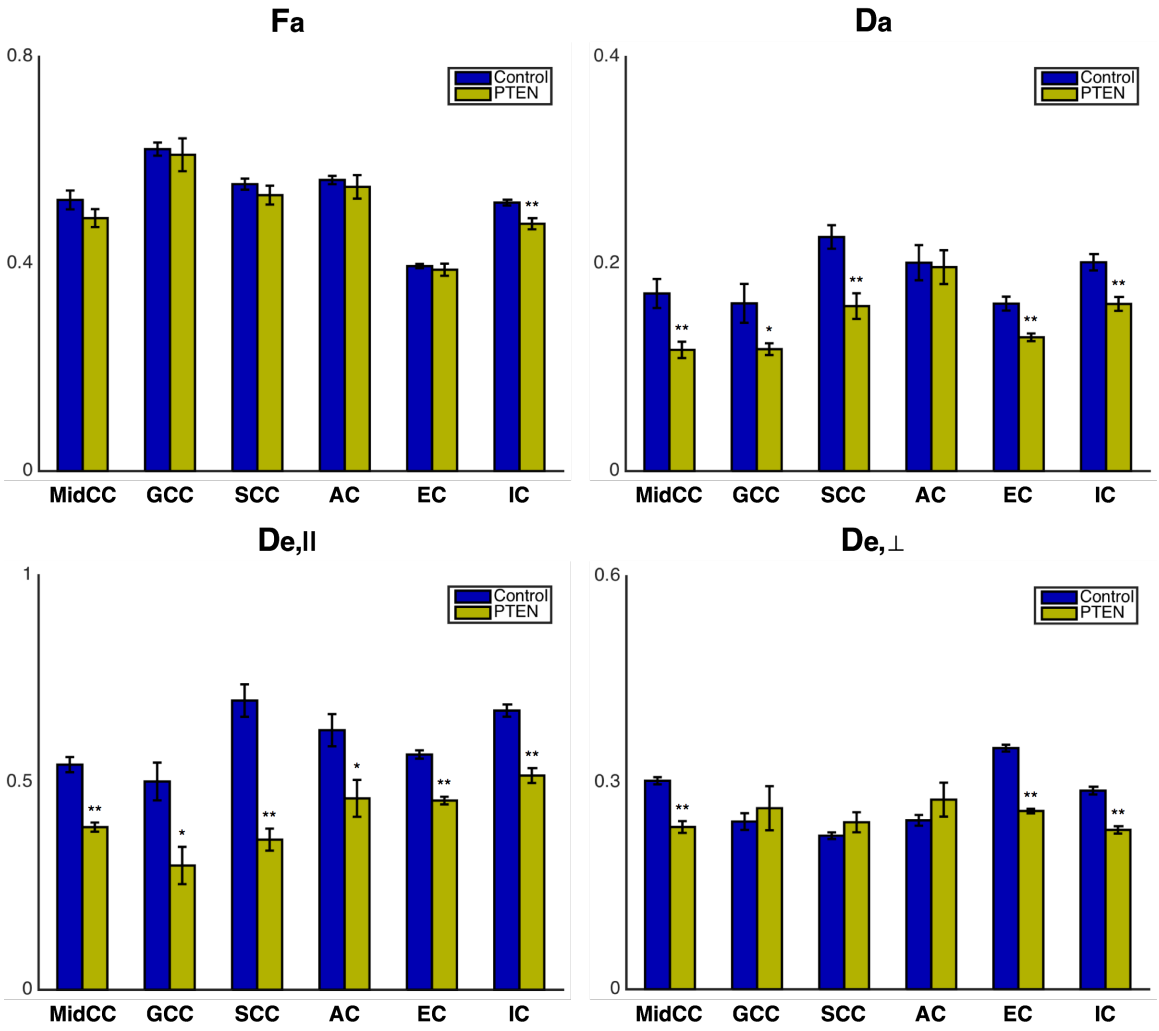

FIG. 4.4. ROI group comparison of WMTI parameters F_a, D_a, $D_{e,\|}$, and $D_{e,\perp}$. Bar heights represent the ROI parameter means across each group, with error bars spanning the mean ± SEM. The two groups are represented with different colors: control = blue and PTEN = yellow. 6 WM ROIs are indicated on the x-axis: MidCC = midbody of the corpus callosum, GCC = genu, SCC = splenium, AC = anterior commissure, EC = external capsule, and IC = internal capsule. F_a is unitless and diffusivities are in units of $\mu m^2/ms$.. * denotes $p < 0.05$ and ** denotes $p < 0.01$ for comparison between the control group and the PTEN group.

all ROIs, with no significant differences present between the two groups. Regarding kurtosis, RK showed the greatest changes, with significantly lower RK in the PTEN group for all white matter tracts except the genu.

Group ROI means of WMTI metrics for the control group and PTEN group are displayed in Fig. 4.4. First, F_a was slightly reduced in the PTEN model, although only significantly different in the internal capsule. Both D_a and $D_{e,\parallel}$ were decreased in the PTEN group for all ROIs, significantly different in all cases except for D_a in the anterior commissure. Lastly, $D_{e,\perp}$ was significantly lower in the MidCC, EC, and IC for the PTEN model compared to control brains.

4.4 Discussion

The quantitative histology measures of axon and myelin microstructure reported in Table 4.1 do confirm a slightly hypermyelinated phenotype in the PTEN model at age P60. The primary difference between the two groups is an increased myelin thickness exhibited by the PTEN model, in agreement with previous work (Flores et al., 2008; Harrington et al., 2010). Another difference observed was a decrease in myelinated axon density. Considering that a reduced oligodendrocyte density (although similar overall count) has been reported (Harrington et al., 2010), it makes sense that the density of axons that are myelinated would also be reduced. Because of this decrease in myelinated axon density, the overall myelin content observed in the PTEN model was only slightly greater than that in the control group. Due to switching from a manual to an automated approach in the EM image analysis, measures of myelin thickness for control mice reported here are significantly greater than those reported in Chapter 3.

Typically, a decrease in WM radial diffusivity is accompanied by an increase in radial kurtosis (Cheung et al., 2009; Kelm et al., 2016). However, in this study, both RD and RK were reduced when compared to the control group. Previous work indicated that RD and RK were sensitive to overall myelin content, but not necessarily myelin thickness (Kelm et al., 2016). Since total myelination was relatively unchanged, this may explain why RK did not increase with increased myelin thickness present in the PTEN model. Additionally, both MD and AD were decreased in the PTEN model, potentially signifying increased cellularity (e.g., astrocytes) and a more restricted extra-axonal space, or a change in the axon structure. Deletion of *Pten* has been previously associated with cell proliferation, and although an increase in oligodendrocytes was not observed, proliferation of astrocytes could possibly occur. Under the assumption that extra-axonal diffusion is greatly reduced, the difference, or heterogeneity, in diffusivities between the intra- and extra-axonal compartments would also be reduced, providing an additional explanation for the observed decrease in radial kurtosis. Improved characterization of the PTEN model would be necessary to appropriately test this hypothesis regarding increased cellularity.

WMTI metrics also provided improved insight into the microstructural changes exhibited by the PTEN model. Axonal water fraction remained mostly unchanged, in agreement with the histologically-derived axon fraction. Also, intra-axonal diffusivity decreased, providing more evidence that something may be different about the axon structure. Gross differences in axons were not observed with EM acquired perpendicular to the nerve fibers, yet histological evaluation parallel to the fibers could reveal axonal changes. Both $D_{e,\parallel}$ and $D_{e,\perp}$ decreased in white matter of the PTEN model, providing additional support for a significant decrease in diffusivity of the extra-axonal space. Previous work has proposed $D_{e,\perp}$ as a specific measure of

myelination (Jelescu et al., 2016), although this was not evident in the hypomyelination study (Kelm et al., 2016). In this work, decreases in $D_{e,\perp}$ were observed with increased myelin thickness, indicating that $D_{e,\perp}$ may be more specific particularly to myelin thickness rather than total myelin content.

4.5. Conclusions

Changes in DWI metrics in the adult PTEN hypermyelinated mouse model were observed, with DKI providing complementary information compared with DTI. Generally, changes in DWI metrics did not oppose those observed in the hypomyelinated mouse models, since overall myelin content remained mostly unchanged. Although the primary difference in the model was increased myelin thickness, changes in axial diffusivity were observed as well, potentially due to increased restrictions in the extra-axonal space. WMTI provided accurate assessment of axon fraction and offered improved specificity to diffusivity changes in the extra-axonal space. Overall, the addition of the PTEN hypermyelinated mouse model provided additional information regarding the relationship between these DWI models and brain myelination.

4.6 Acknowledgements

The author thanks Brittany Parker for technical assistance with animal husbandry and Janice Williams, Ph.D., of the VUMC Cell Imaging Shared Resource for assistance with microscopy. Processing of EM sections and EM image collection were performed through the use of the VUMC Cell Imaging Shared Resource, supported by NIH grants CA68485, DK20593, DK58404, HD15052, DK59637, and EY008126. This work was also supported by NIH grants R01 EB001744, R01 EB019980, 5K08 NS050484, and S10 RR029523.

4.7 References

Andersson, J.L., Jenkinson, M., Smith, S., 2007. Non-linear registration, aka Spatial normalisation FMRIB technical report TR07JA2. FMRIB Analysis Group of the University of Oxford 2.

Cheung, M.M., Hui, E.S., Chan, K.C., Helpern, J.A., Qi, L., Wu, E.X., 2009. Does diffusion kurtosis imaging lead to better neural tissue characterization? A rodent brain maturation study. NeuroImage 45, 386–392. doi: 10.1016/j.neuroimage.2008.12.018

Flores, A.I., Narayanan, S.P., Morse, E.N., Shick, H.E., Yin, X., Kidd, G., Avila, R.L., Kirschner, D.A., Macklin, W.B., 2008. Constitutively active Akt induces enhanced myelination in the CNS. J. Neurosci. 28, 7174–7183.

Harrington, E.P., Zhao, C., Fancy, S.P.J., Kaing, S., Franklin, R.J.M., Rowitch, D.H., 2010. Oligodendrocyte PTEN is required for myelin and axonal integrity, not remyelination. Ann. Neurol. 68, 703–716. doi: 10.1002/ana.22090

Jelescu, I.O., Zurek, M., Winters, K.V., Veraart, J., Rajaratnam, A., Kim, N.S., Babb, J.S., Shepherd, T.M., Novikov, D.S., Kim, S.G., 2016. In vivo quantification of demyelination and recovery using compartment-specific diffusion MRI metrics validated by electron microscopy. NeuroImage 132, 104–114.

Jenkinson, M., Bannister, P., Brady, M., Smith, S., 2002. Improved optimization for the robust and accurate linear registration and motion correction of brain images. NeuroImage 17, 825–841.

Jenkinson, M., Smith, S., 2001. A global optimisation method for robust affine registration of brain images. Med. Image Anal. 5, 143–156.

Kelm, N.D., West, K.L., Carson, R.P., Gochberg, D.F., Ess, K.C., Does, M.D., 2016. Evaluation of diffusion kurtosis imaging in ex vivo hypomyelinated mouse brains. NeuroImage 124, 612–626. doi: 10.1016/j.neuroimage.2015.09.028

Paxinos, G., Franklin, K.B., 2004. The mouse brain in stereotaxic coordinates. Gulf Professional Publishing.

Smith, S.M., Jenkinson, M., Woolrich, M.W., Beckmann, C.F., Behrens, T.E., Johansen-Berg, H., Bannister, P.R., De Luca, M., Drobnjak, I., Flitney, D.E., 2004. Advances in functional and structural MR image analysis and implementation as FSL. NeuroImage 23, S208–S219.

CHAPTER 5

DIFFUSION KURTOSIS IMAGING IN NORMALLY AND ABNORMALLY DEVELOPING MOUSE BRAIN

5.1 Introduction

Although the majority of structural brain development occurs during gestation and infancy, brain white matter continues to mature throughout childhood and adolescence into adulthood, primarily in the form of myelination (Benes et al., 1994; Brody et al., 1987; Yakovlev and Lecours, 1967). Myelination abnormalities during this crucial period of brain development contribute to neurological deficits in a variety of disorders, including autism (Barnea-Goraly et al., 2004) and schizophrenia (Davis et al., 2003; Flynn et al., 2003). Therefore, non-invasive assessment of white matter during development has the potential to improve diagnosis and treatment of these conditions. Various MRI methods have shown promise in white matter characterization, including multi-exponential T_2 (MET_2) (MacKay et al., 1994; Menon et al., 1992), quantitative magnetization transfer (qMT) (Gochberg and Gore, 2007; Koenig et al., 1990; Kucharcyzk et al., 1994; Sled and Pike, 2000) and diffusion-weighted imaging (DWI) (Basser et al., 1994; Beaulieu, 2002). MET_2 and qMT have demonstrated high specificity to myelin content, yet clinical application of these methods has been limited due to lengthy scan times and high signal-to-noise ratio (SNR) requirements. On the other hand, DWI is regularly applied in the clinical setting and has shown to be highly sensitive to both axon and myelin microstructure, making it a favorable approach for the assessment of brain development.

DWI has been used extensively for the study of various stages of brain development, yet questions still remain about the relationship between DWI metrics and the underlying microstructure during development. Many studies have examined white matter development with DTI, generally reporting increases in FA and decreases in MD and RD from birth to adulthood (Lebel et al., 2008; Neil et al., 2002). DKI has been used to evaluate normal rat brain development (Cheung et al., 2009), mouse brain development in a Huntington's disease model (Blockx et al., 2012), and normal brain development in early childhood (Paydar et al., 2014), observing increases in MK, AK, and RK, with RK exhibiting the greatest changes. One prior study used WMTI to evaluate human white matter development from birth to 3 years of age, observing an increase in F_a as age increased (Jelescu et al., 2015). Although these studies have demonstrated the utility of DTI, DKI, and WMTI metrics in monitoring white matter development, direct comparisons of these DWI measures with histology, particularly morphological measurements of axon/myelin microstructure through electron microscopy (EM), have been limited and could provide improved insight into the relationship between DWI and brain development.

The objective of this work was to investigate the relationship between DTI, DKI, and WMTI metrics and white matter microstructure during normal and abnormal mouse brain development through comparisons with histologic measures derived from EM. Also, this study seeks to determine whether the associations between DWI and WM microstructure described in Chapters 3 and 4 are also applicable to the complex process of brain development. Three conditional knockout mouse models associated with the human genetic developmental disorder tuberous sclerosis complex, *Rictor* Olig2-Cre CKO (Rictor), *Tsc2* Olig2-Cre CKO (TSC), and *Pten* Olig2-Cre CKO (PTEN), were utilized due to their varying degrees of myelin development.

The Rictor and TSC models have been shown to exhibit moderate and severe hypomyelination, respectively, in adult mice (Carson et al., 2013; 2015; Kelm et al., 2016), whereas the PTEN model is characterized by hypermyelination (Harrington et al., 2010). These CKO mice are viable into adulthood and capable of reproduction, and EM images of white matter ultrastructure indicate that axons and myelin appear normal. In order to elucidate the relationship between DWI and white matter microstructure during development, we evaluated DTI, DKI, and WMTI metrics, as well as MWF and PSR, and compared them to quantitative EM measures of axon and myelin morphology at ages P20, P30, and P60 in both normally-developing and abnormally-developing mouse brain.

5.2 Materials and Methods

5.2.1 MRI and Histology Acquisition and Processing

In this study, a total of 67 mice—control, Rictor, TSC, and PTEN mice at ages P20, P30, and P60 (Table 5.1)—were perfusion-fixed and their brains were excised and prepared for imaging using the methods stated in Section 2.1.1. MRI acquisition and analysis were performed for each brain as in Section 2.1, except for the P60 control, Rictor, and TSC brains (see Section 3.2). After MRI was completed, a subset of mouse brains was sectioned for histology (Table 5.1) using the approach detailed in Section 2.1.4.1. A larger sample size was used for the control groups (N = 6) due to greater intragroup variation in myelin content compared with the CKO groups. Due to the large number of brains examined in this study, only the midbody of the corpus callosum (MidCC) section for each brain was processed for histological evaluation. EM data were acquired and analyzed using the methods stated in Section 2.1.4.2. Histological

measures were compared between the control and CKO groups at each age using a Wilcoxon rank-sum test, with multiple comparisons correction performed using a Bonferroni correction.

Table 5.1. MRI and histology sample size for each model and age. Histology brains are a subset of those imaged with MRI.

	MRI			Histology		
	P20	P30	P60	P20	P30	P60
Control	9	10	8	6	6	6
Rictor	5	5	5	3	3	3
TSC	4	0	5	3	0	3
PTEN	5	4	7	3	3	3

5.2.2 Group ROI Analysis

For group analysis, b=0 images were registered to a representative control mouse brain at each age using FSL's (FMRIB Analysis Group, Oxford, UK) linear (FLIRT) and non-linear (FNIRT) registration tools (Andersson et al., 2007; Jenkinson et al., 2002; Jenkinson and Smith, 2001; Smith et al., 2004). DTI, DKI, WMTI, MWF, and PSR parameter maps were then registered using the same transformations derived from the b=0 registration. Referencing a standard mouse brain atlas (Paxinos and Franklin, 2004), an ROI was manually delineated in the MidCC on a mid-sagittal slice at Bregma -0.7 mm. Using the ROI means for each individual mouse brain, linear correlations were determined between DTI, DKI, and WMTI parameters, as well as MWF and PSR, and histologic measures, with multiple comparisons correction performed using a simple Bonferroni correction.

5.2.3 Tractography

Using the DWI data, deterministic tractography was performed on a representative control brain at each age with ExploreDTI (Leemans et al., 2009). Utilizing a standard mouse brain atlas

(Paxinos and Franklin, 2004), seed ROIs were manually drawn for six major white matter tracts: MidCC, genu (GCC), splenium (SCC), anterior limb of the anterior commissure (AC), fornix/fimbria of the hippocampus (F), and internal capsule (IC). The seed voxels were sampled such that there were 3 seed points per voxel in each dimension (3^3 or 27 total per voxel). The FA threshold to initiate and continue tracking was set at 0.25, to restrict tracking to major white matter pathways, and the maximum angle was set to 30°. Additionally, target and exclusion ROIs were manually drawn to select a specified segment of each white matter tract and to prevent the inclusion of spurious tracts. Once white matter tracts were defined on the template brain at each age, the age-appropriate tract masks were extracted and applied to the rest of the brains so that tract-based measurements of DTI, DKI, and WMTI parameters, as well as MWF and PSR, could be computed. In order to ensure that only white matter voxels were included in these measurements, voxels with FA < 0.25 (the tractography threshold) were excluded from further analyses. In addition, a small number of voxels (< 0.5%) with unreasonable parameter values (RK < 0 or RK > 10, $D_{e,\perp} > 1$, MWF > 0.5, PSR = 0 or PSR > 0.5) were excluded from subsequent analyses. Group comparisons of all MR metrics were then made for each tract using a Wilcoxon rank-sum test.

5.3 Results

5.3.1 Histology

Figure 5.1 shows representative 15000x EM images, and their processed forms, of the midbody of the corpus callosum from P20, P30, and P60 control mouse brains. Looking at these examples, there is an obvious increase in the number of myelinated axons as age increases. Furthermore, it

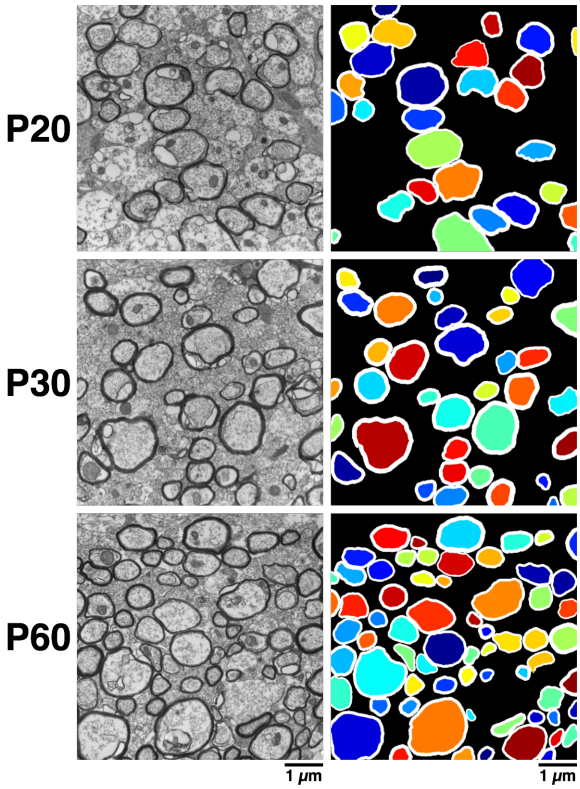

FIG. 5.1. EM images of white matter across normal brain development. Representative original (left) and processed (right) 15000x EM images of the midbody of the corpus callosum from normal P20, P30, and P60 mouse brains. There is a noticeable increase in the number of myelinated axons as a function of age.

appears that this increase is primarily driven by an increase in smaller axons, potentially due to smaller axons being myelinated at a later time point than large axons.

Figure 5.2 shows plots of group mean histology measures in the MidCC for each model as a function of age. First considering the control brains across age, there were increases in myelin fraction, axon fraction, and myelinated axon density and decreases in axon diameter and g-ratio from P20 to P60. Mean myelin thickness remained mostly unaffected, indicating that decreases in g-ratio were due to decreases in mean axon diameter. Despite the unchanged myelin thickness and decreased axon diameter, both f_m, and f_a increased, meaning that these changes can be attributed to the increase in myelinated axon density. Next, comparing the Rictor group with the control group, f_m, f_a, and ρ_a were lower for the Rictor group at P20 and P30, but at P60, only

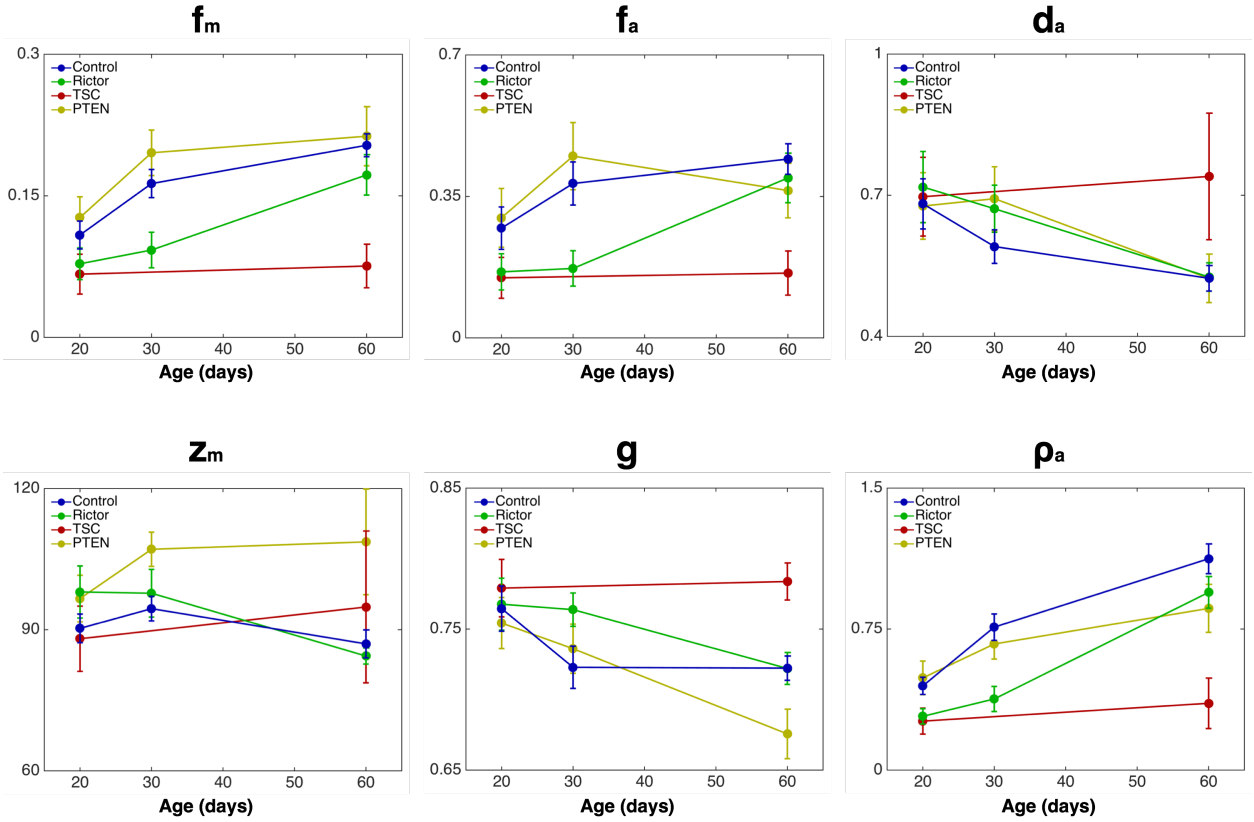

FIG. 5.2. EM histology measures across normal and abnormal brain development. Group mean ± SEM of quantitative EM histology measures, f_m, f_a, d_a, z_m, g, and ρ_a (y-axis), of the MidCC for control, Rictor, TSC, and PTEN groups as a function of age (x-axis). f_m, f_a, and g are unitless, d_a is in units of μm, z_m is in units of nm, and ρ_a is in units of axons/μm^2.

f_m was significantly decreased ($p < 0.05$, with Bonferroni correction). Additionally, the disparity in f_m at P30 is much larger than at P60, possibly signifying a delay in myelination during development. The other hypomyelination model, TSC, exhibited significantly lower f_m, f_a, and ρ_a ($p < 0.05$) at both P20 and P60, indicative of severe hypomyelination. In fact, changes in EM measures between P20 and P60 for the TSC group were minimal, showing a lack of WM maturation during this period of development. Finally, comparing the PTEN and control groups, PTEN exhibited significantly higher z_m ($p < 0.05$) at all ages. Additionally, PTEN showed higher f_m at all ages and lower ρ_a at P30 and P60, although from these, only the change in f_m at P30 was significant ($p < 0.05$). Generally, the PTEN model exhibited increases in myelin thickness and

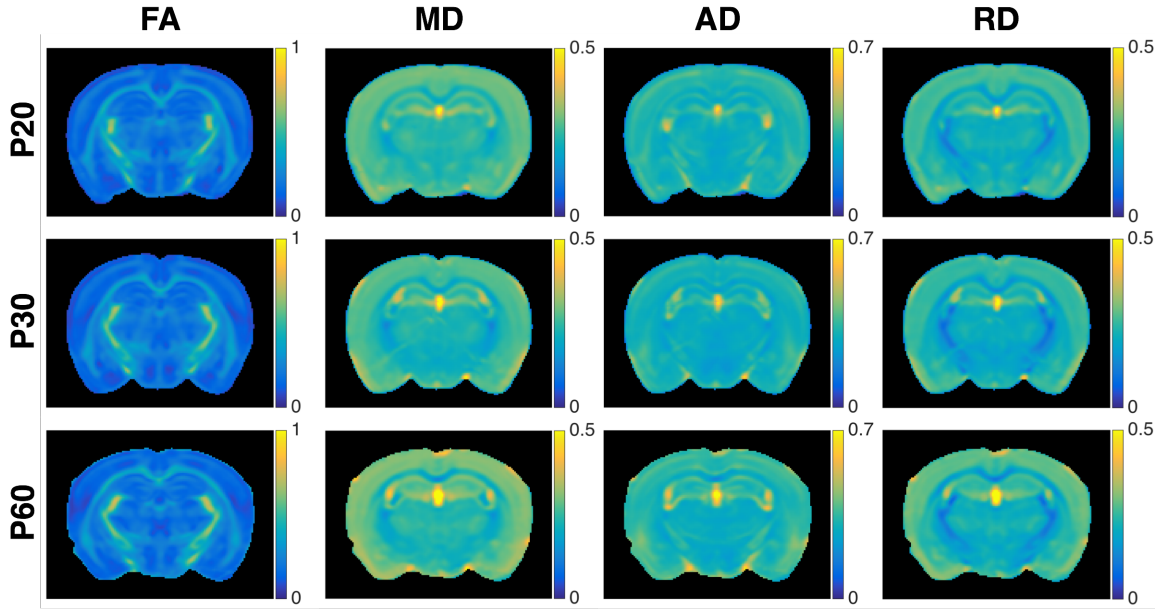

FIG. 5.3. Group-averaged coronal DTI parameter maps of normally-developing mouse brain. The rows represent the three ages: P20, P30, and P60 (top to bottom). The columns represent the DTI parameters FA, MD, AD, and RD (left to right). FA is unitless and diffusivities are in units of $\mu m^2/ms$.

decreases in myelinated axon density, resulting in slightly higher myelin fraction compared with controls.

5.3.2 DWI Parameter Maps

Figure 5.3 contains group-averaged parameter maps of control brains at each age for the DTI metrics FA, MD, AD, and RD. There are noticeable decreases in white matter MD and RD as age increases. On the other hand, FA and AD appear to be mostly similar across age, with a minor increase in FA visually observed in the fimbria of the hippocampus and a slight decrease in AD in the corpus callosum. Group-averaged maps of control brains for DKI parameters MK, AK, and RK are shown in Fig. 5.4. There are apparent increases in white matter MK, AK, and RK as a function of age, although the changes in MK and RK are more obvious than those seen

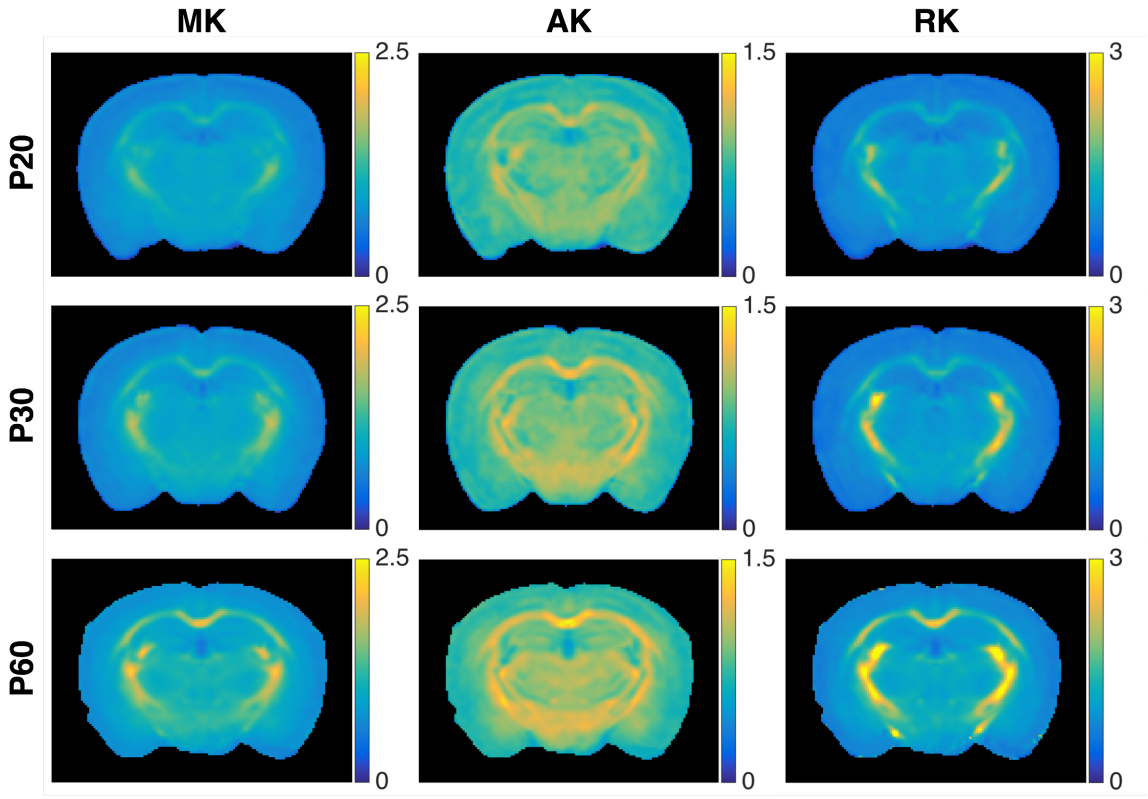

FIG. 5.4. Group-averaged coronal DKI parameter maps of normally-developing mouse brain. The rows represent the three ages: P20, P30, and P60 (top to bottom). The columns represent the DKI parameters MK, AK, and RK. Kurtosis is unitless.

in AK. Lastly, Fig. 5.5 shows group-averaged parameter maps of control brains at P20, P30, and P60 for WMTI measures F_a, D_a, $D_{e,\parallel}$, and $D_{e,\perp}$. WMTI parameter values for white matter (determined as FA > 0.35 in the template brain) were overlaid on the template b=0 image for each age. There are noticeable increases in F_a as age increases and a slight increase in $D_{e,\perp}$ at P60. Changes in D_a and $D_{e,\parallel}$ across age are not visually apparent.

5.3.3 Tract-based MRI Metrics

Figure 5.6 displays the six white matter tracts defined for this study: MidCC, GCC, SCC, AC, F, and IC, along with gamma distributions fitted to tract-based measures of FA, RD, MK, RK, and F_a for control mouse brains. Regarding FA, noticeable increases in FA can be observed in the

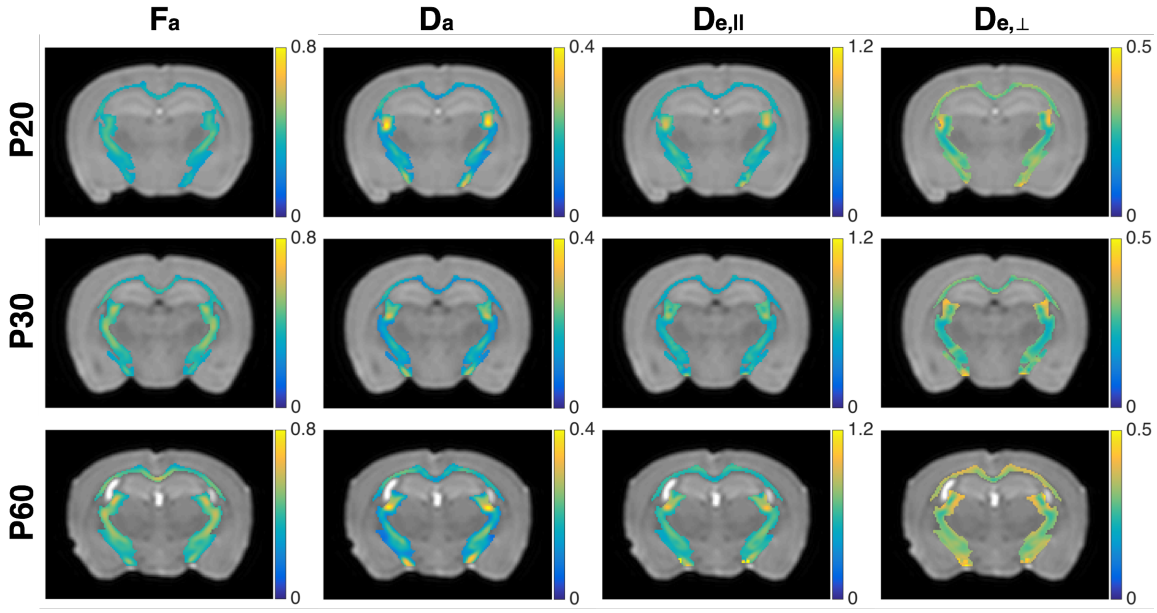

FIG. 5.5. Group-averaged coronal WMTI parameter maps of normally-developing mouse brain. WMTI parameter values for white matter voxels are overlaid on the template b=0 image for each age. The rows represent the three ages: P20, P30, and P60 (top to bottom). The columns represent the WMTI parameters F_a, D_a, $D_{e,||}$, and $D_{e,\perp}$. F_a is unitless and diffusivities are in units of $\mu m^2/ms$.

corpus callosum and fornix as age increases, yet the distributions are mostly similar for the anterior commissure and internal capsule. Furthermore, for the tracts that showed increases, the distributions become broader as age increases from P20 to P30 to P60. Although decreases in mean RD are apparent in most tracts between P20 and P60, changes in the distributions are not as distinguishable as those observed with FA. The distributions for MK, RK, and F_a show obvious increases in these metrics as a function of age, with changes in RK being the most visually apparent. Similar to FA, their distributions become broader as age increases, possibly indicating more heterogeneous tract myelination as the brain develops.

Bar graphs representing the tract-based group means of DTI parameters FA and RD are displayed in Fig. 5.7. There were significant increases ($p < 0.05$) in FA from P20 to P60 in the corpus callosum and fornix for the control group, the GCC, AC, and F for the Rictor group, the

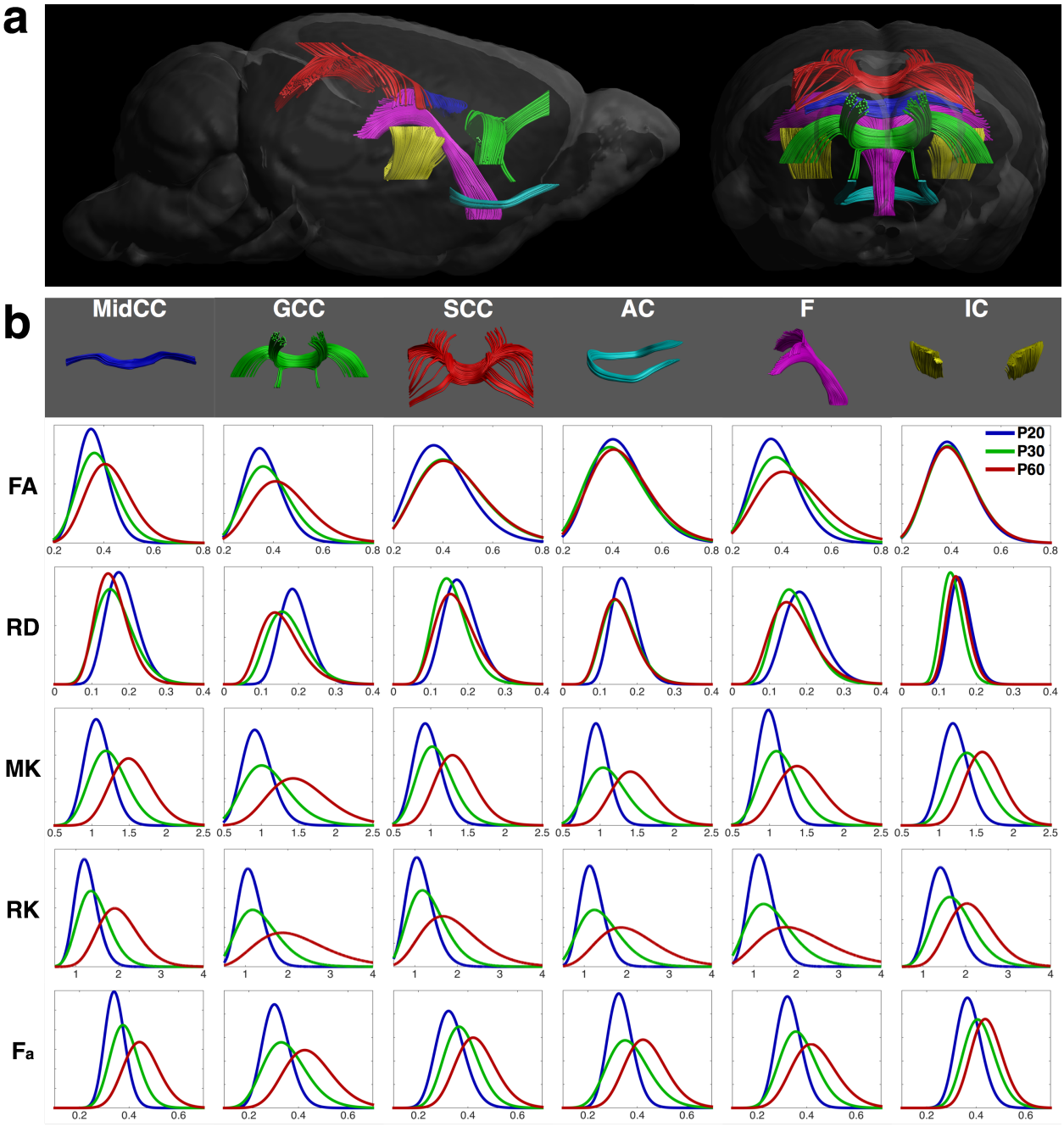

FIG. 5.6. Tractography and tract-based DWI measures. (a) Six white matter tracts defined on a normal P30 mouse brain shown in sagittal (left) and coronal (right) orientations. Each WM tract is represented by a different color: MidCC = blue, GCC = green, SCC = red, AC = cyan, F = magenta, and IC = yellow. (b) Tract-based measures of DWI metrics FA, RD, MK, RK, and F_a (rows) in each WM tract (columns) for control brains at P20 (blue), P30 (green), and P60 (red). Plot curves are defined by gamma distributions fitted to parameter values from all voxels in each tract, across all control brains at each age.

fornix for the TSC group, and all tracts for the PTEN model. Within each age, FA was similar across models, with the exception of generally lower FA in TSC at P60. Also, there were

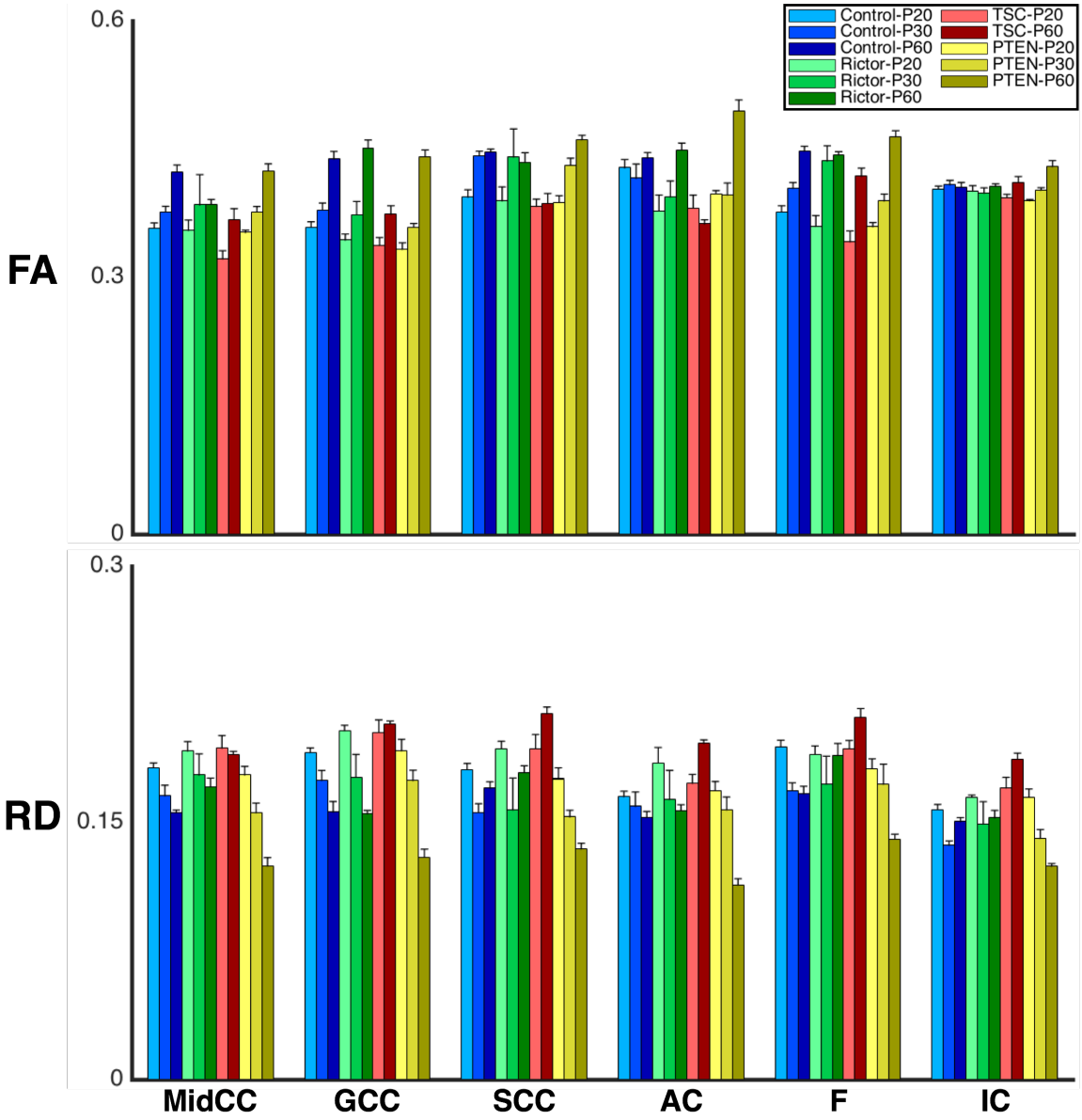

FIG. 5.7. Tract-based group comparison of DTI parameters FA and RD. Bar heights represent the tract-based parameter means across each group, with error bars representing the SEM. The four models are represented with different colors: control = blue, Rictor = green, TSC = red, and PTEN = yellow and the three ages are represented by different shades of each color: P20 = light, P30 = medium, and P60 = dark. 6 WM tracts are indicated on the x-axis: MidCC = midbody of the corpus callosum, GCC = genu, SCC = splenium, AC = anterior commissure, F = fornix, and IC = internal capsule. FA is unitless and RD is in units of $\mu m^2/ms$.

minimal differences in FA of the internal capsule across all groups. Significant decreases in RD from P20 to P60 were observed in the MidCC, GCC, SCC, AC, and F for the control group, the

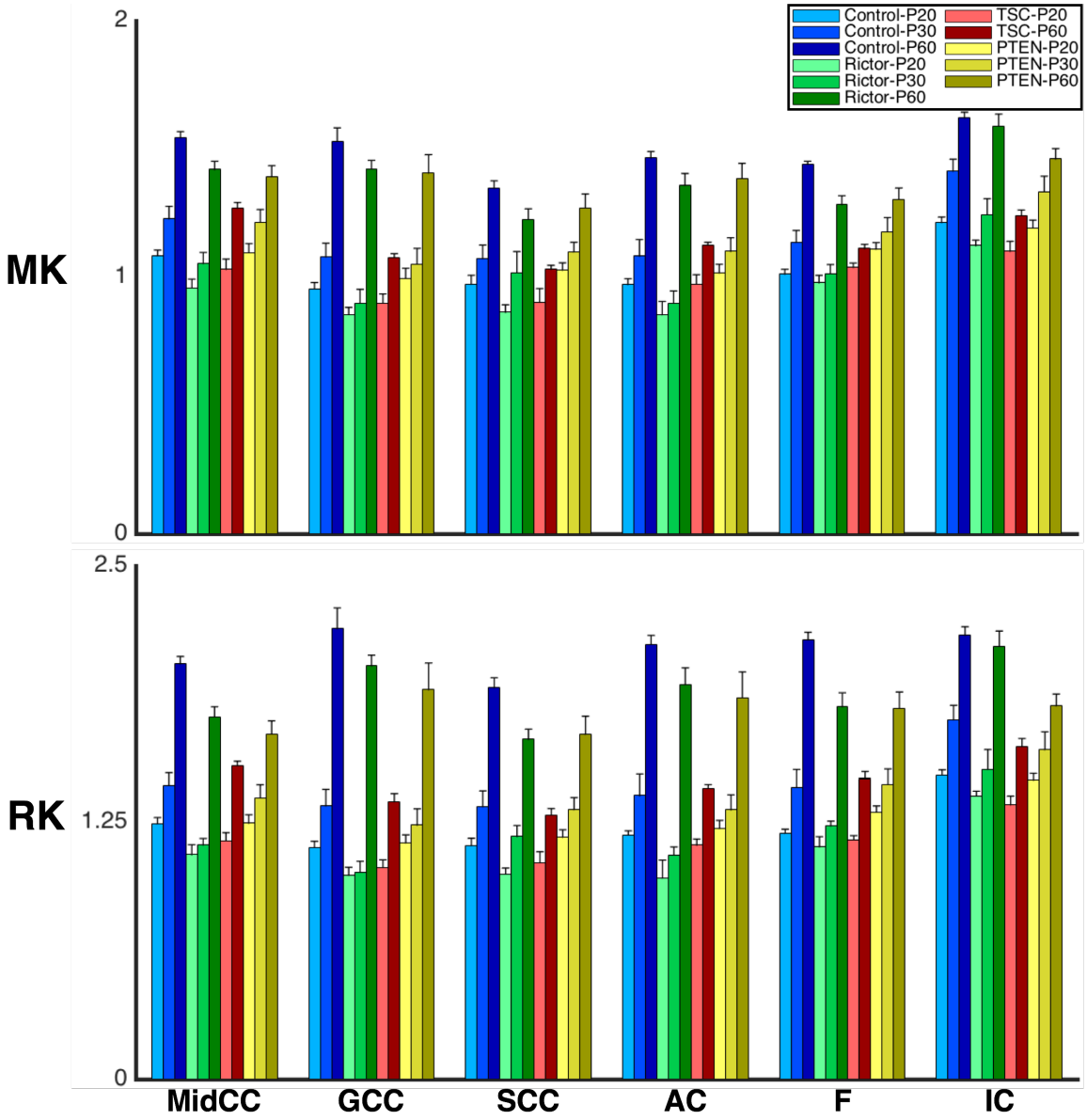

FIG. 5.8. Tract-based group comparison of DKI parameters MK and RK. Bar heights represent the tract-based parameter means across each group, with error bars representing the SEM. The four models are represented with different colors: control = blue, Rictor = green, TSC = red, and PTEN = yellow and the three ages are represented by different shades of each color: P20 = light, P30 = medium, and P60 = dark. 6 WM tracts are indicated on the x-axis: MidCC = midbody of the corpus callosum, GCC = genu, SCC = splenium, AC = anterior commissure, F = fornix, and IC = internal capsule. Kurtosis is unitless.

MidCC, GCC, and AC for the Rictor model, and all tracts for the PTEN model. On the other hand, RD for the TSC model generally increased from P20 to P60. At P20 and P30, RD of each model was similar to the control group, but at P60, Rictor had higher RD in the MidCC and F, TSC had higher RD in all tracts, and PTEN showed lower RD in all tracts. Changes in MD (not shown) were similar to those seen in RD, and AD remained mostly the same across groups except for a decrease in the AD of the PTEN P60 group compared with control brains.

Figure 5.8 shows tract-based group means of DKI metrics MK and RK. Significant increases ($p < 0.05$) in MK between P20 and P60 can be observed for all tracts in each model, including the TSC model where minimal changes were observed in DTI parameters. At P20 and P30, few differences in MK exist between the control group and CKO models, although MK of the Rictor group is slightly reduced at P30. At P60, there were significant decreases in MK in the Rictor model for the MidCC and F, in the TSC model for all tracts, and in the PTEN model for the MidCC, F, and IC. The changes in RK mimic those seen in MK, except they are greater in magnitude, meaning that RK is better able to distinguish changes between ages P20 and P30 as well as P30 and P60, in addition to differences existing between the control group and the Rictor and PTEN models. AK (not shown) generally increased as a function of age, although these changes were more subtle than those observed with MK and RK. Additionally, AK was mostly similar between control and CKO groups at each age.

Tract-based group means of WMTI parameters F_a and $D_{e,\perp}$ are shown in Fig. 5.9. Similar to MK and RK, significant increases in F_a were observed between P20 and P60 for all tracts and all models. At P20, F_a of the Rictor and TSC models were slightly reduced compared with the control group, yet at P30, F_a was similar for the control and Rictor groups. However, at P60, the Rictor group exhibited significantly lower F_a in the MidCC, SCC, AC, and F and the TSC group

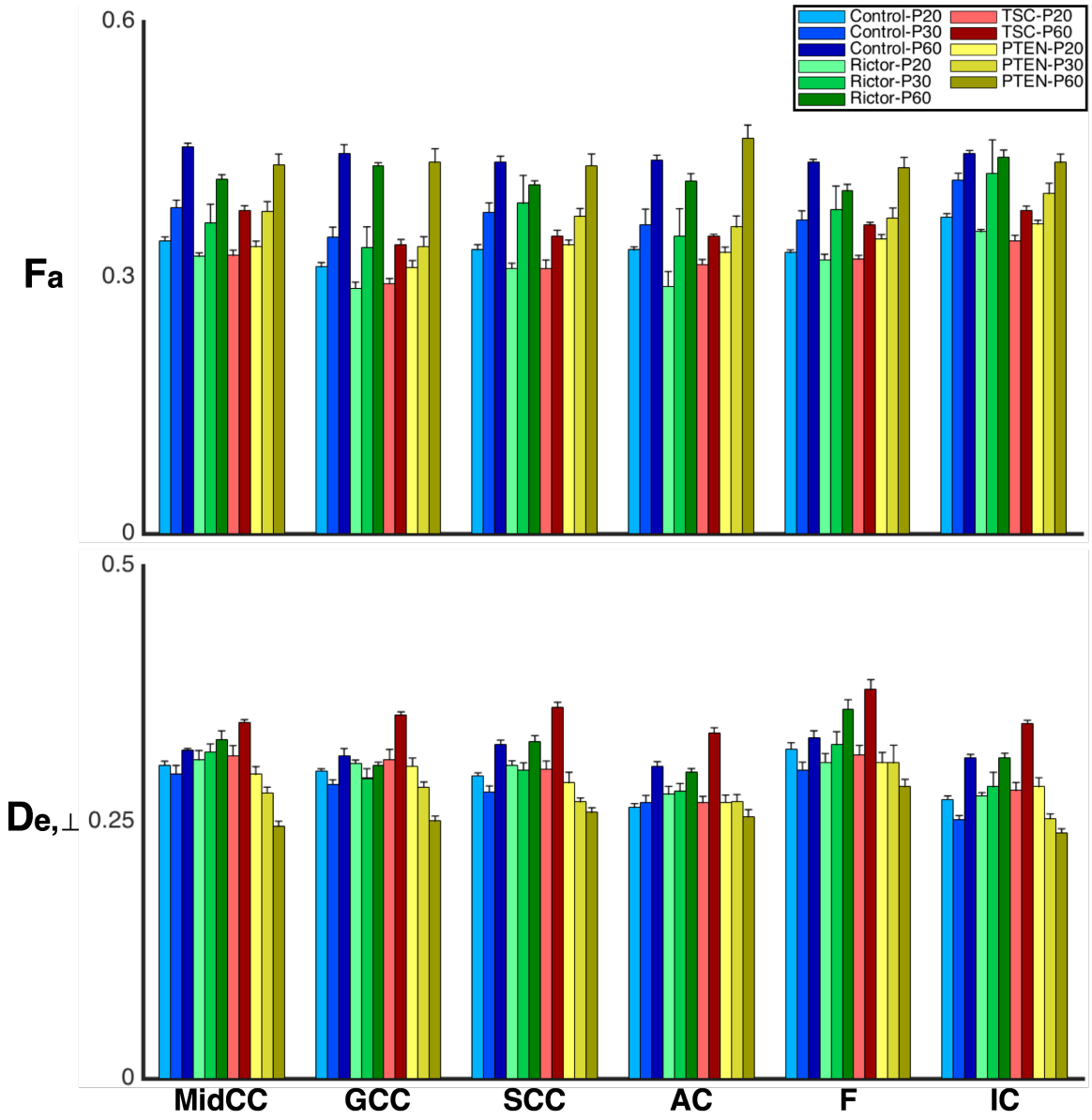

FIG. 5.9. Tract-based group comparison of WMTI parameters F_a and $D_{e,\perp}$. Bar heights represent the tract-based parameter means across each group, with error bars representing the SEM. The four models are represented with different colors: control = blue, Rictor = green, TSC = red, and PTEN = yellow and the three ages are represented by different shades of each color: P20 = light, P30 = medium, and P60 = dark. 6 WM ROIs are indicated on the x-axis: MidCC = midbody of the corpus callosum, GCC = genu, SCC = splenium, AC = anterior commissure, EC = external capsule, and IC = internal capsule. F_a is unitless and $D_{e,\perp}$ is in units of $\mu m^2/ms$.

had lower F_a in all 6 tracts. The PTEN model showed no significant changes in F_a compared with the control group at all ages. From age P20 to P60, there were significant increases ($p <$

0.05) in $D_{e,\perp}$ for the control group in the MidCC, SCC, AC, and IC, for the Rictor group in the AC, F, and IC, and for the TSC group in all tracts. On the other hand, decreases in $D_{e,\perp}$ of the PTEN model were observed in the MidCC, SCC, GCC, and IC as age increased from P20 to P60. Changes in $D_{e,\perp}$ between the control group and CKO models at ages P20 and P30 were minimal. At P60, in comparison to the control group, $D_{e,\perp}$ was similar in the Rictor group, increased in all tracts for the TSC group, and decreased in all tracts for the PTEN model. WMTI metric D_a (not shown) was mostly similar across all models and ages, although slight increases were observed in a few tracts for the control, Rictor, and TSC groups from P20 to P60. Similar to $D_{e,\perp}$, $D_{e,\parallel}$ (not shown) generally increased in the control, Rictor, and TSC groups and decreased in the PTEN group as age increased from P20 to P60.

Figure 5.10 shows bar graphs representing the group means of tract-based measurements of myelin-related metrics MWF and PSR. Significant increases ($p < 0.05$) in MWF between P20 and P60 were observed in all tracts for the control and PTEN groups. In contrast, MWF increased in only the GCC, AC, and IC for the Rictor group and no significant differences were observed in the TSC group. For the control and PTEN groups, there were more significant increases in MWF present between P20 and P30 (all tracts for the control group, all tracts except the MidCC for the PTEN model) than there were between P30 and P60 (only IC for the control group, GCC and F for the PTEN model). At P20, MWF in the control, Rictor, and PTEN groups was mostly similar, except for higher MWF present in the IC for the PTEN group. In contrast, MWF was significantly lower in the TSC model for all tracts except the MidCC. At P30, the Rictor and PTEN models begin to show differences with the control group, with decreases observed in the GCC, SCC, AC, and IC for the Rictor group and increases in the F and IC for the PTEN group. Finally at P60, compared with the control group, MWF was lower in all tracts

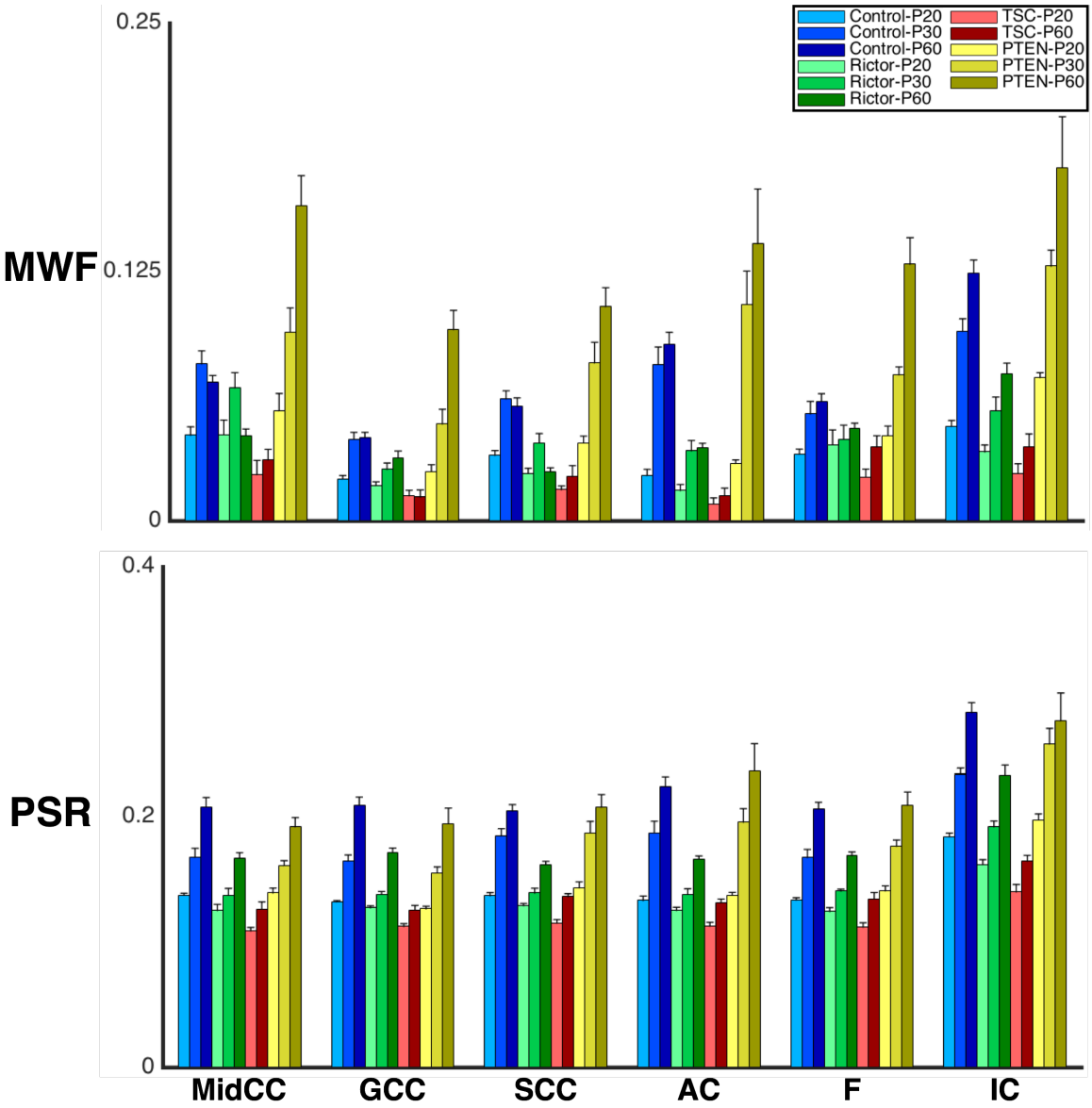

FIG. 5.10. Tract-based group comparison of myelin-associated MR parameters MWF and PSR. Bar heights represent the tract-based parameter means across each group, with error bars representing the SEM. The four models are represented with different colors: control = blue, Rictor = green, TSC = red, and PTEN = yellow and the three ages are represented by different shades of each color: P20 = light, P30 = medium, and P60 = dark. 6 WM ROIs are indicated on the x-axis: MidCC = midbody of the corpus callosum, GCC = genu, SCC = splenium, AC = anterior commissure, EC = external capsule, and IC = internal capsule. MWF and PSR are unitless.

except the GCC for the Rictor model, lower in all tracts for the TSC model, and higher in the MidCC, GCC, SCC, and F for the PTEN group. Regarding PSR, significant increases were seen in the control group between P20 and P30, as well as between P30 and P60. Also, significant

increases between P20 and P60 were observed in all tracts for the Rictor and PTEN groups and in the SCC, AC, F, and IC of the TSC model. Generally, the Rictor and TSC groups exhibited lower white matter PSR at P20 than the control group, whereas the PTEN group was similar to the control group at this age. At P30, the Rictor group had significantly lower PSR in all tracts compared with the control group, but the PTEN model remained similar to the control group. Lastly, at P60, significant decreases in PSR were present in all tracts for the Rictor and TSC groups when compared with the control group, yet no significant differences were observed between the PTEN and control groups.

5.3.4 Correlation Analysis

Figure 5.11 shows scatter plots of select DWI metrics: RD, RK, F_a, and $D_{e,\perp}$, versus histology measures across all brains, along with simple linear correlations. RD, RK, and F_a show strong correlations with histologic myelin fraction, axon fraction, axon diameter and myelinated axon density, whereas $D_{e,\perp}$ did not exhibit significant correlations with any of these histologic measures. The strongest correlation observed was between RK and ρ_a ($r^2 = 0.64$). Table 5.2 summarizes the linear correlation results for all MR and histology metrics, showing r^2 for significant correlations. Correlations with histology were observed for FA and MD, but in general, these were weaker than those seen for RD, RK, and F_a. Similar to RK, MK correlated strongly with f_m, f_a, ρ_a, and d_a. However, none of these parameters correlated with myelin thickness. Axial-associated DWI parameters, AD, AK, D_a, and $D_{e,\parallel}$, did not exhibit any correlation with histology, except for a weak correlation between $D_{e,\parallel}$ and z_m. As expected, MWF and PSR correlated strongly with f_m and ρ_a. However, they also showed weak correlations with

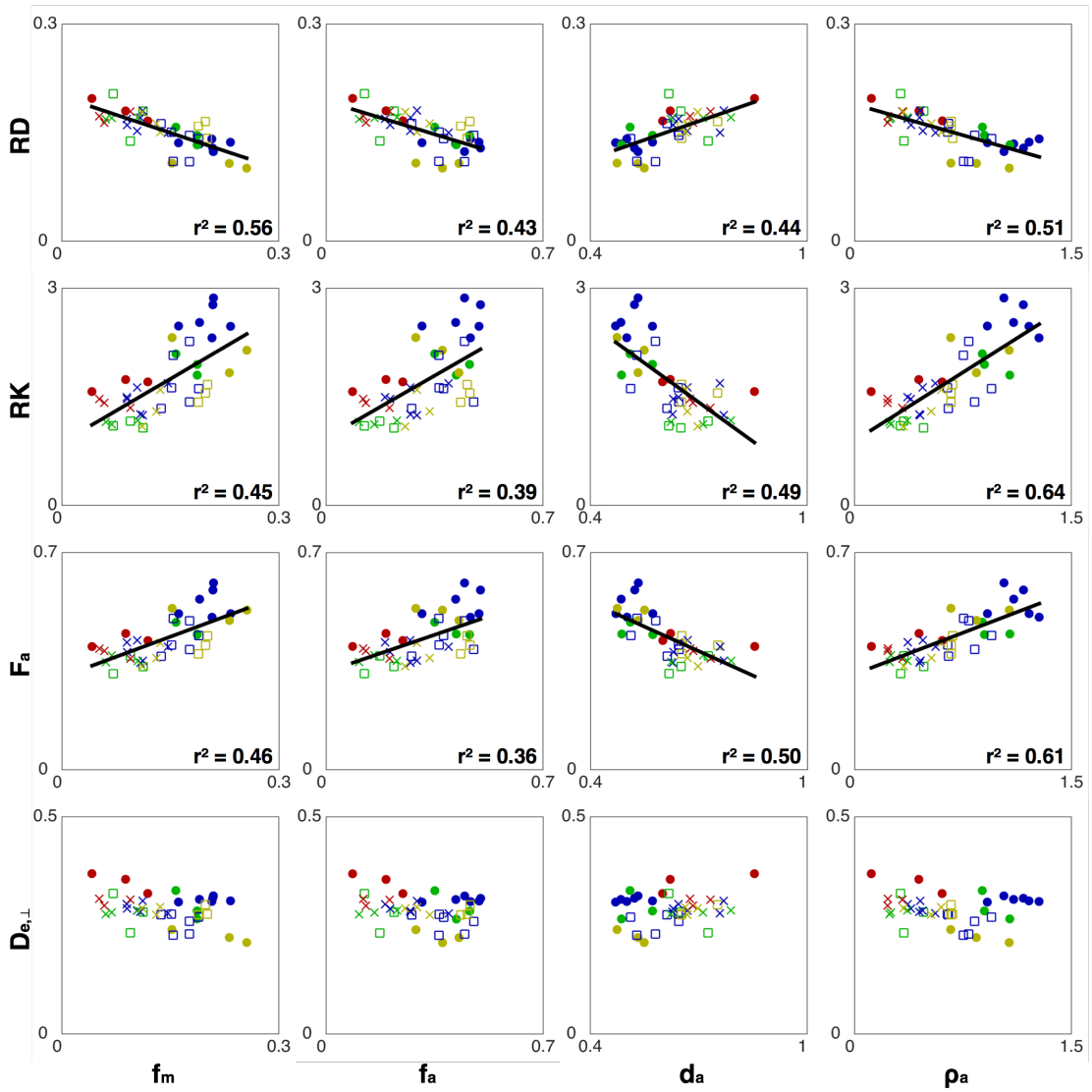

FIG. 5.11. Scatter plots of DWI metrics RD, RK, F_a, and $D_{e,\perp}$ (y-axis) vs. histology measures f_m, f_a, d_a, ρ_a (x-axis). Each point is an ROI mean of the MidCC from an individual mouse brain. The shape represents the age: P20 = x, P30 = square, and P60 = circle and the color represents the model: control = blue, Rictor = green, TSC = red, and PTEN = yellow. All MRI and histology ROIs are located in the MidCC. For significant linear correlations, the fitted line is shown and r^2 is displayed in the lower right-hand corner of each plot. RK, F_a, f_m, and f_a are unitless, RD and $D_{e,\perp}$ are in units of $\mu m^2/ms$, d_a is in units of μm, and ρ_a is in units of axons/μm^2.

axon diameter, and PSR correlated strongly with axon fraction. In addition, neither MR metric correlated with myelin thickness.

Table 5.2. r^2 from linear correlations of MRI metrics with histology measures.

	DTI				DKI			WMTI				Myelin	
	FA	MD	AD	RD	MK	AK	RK	F_a	D_a	$D_{e,\parallel}$	$D_{e,\perp}$	MWF	PSR
f_m	0.27	0.43		0.56	0.44		0.45	0.46				0.49	0.57
f_a		0.32		0.43	0.38		0.39	0.36					0.45
d_a	0.29	0.31		0.44	0.44		0.49	0.50				0.34	0.30
ρ_a	0.39	0.34		0.51	0.55		0.64	0.61				0.39	0.63
z_m										0.26			

Only r^2 values for significant correlations ($p < 0.05$) are shown.

5.4 Discussion

The quantitative EM measures reported in Fig. 5.2 show clear differences in WM microstructure between ages P20 and P60 in normal development, as well as between control and myelin-related CKO mouse models. In control mice, there was a large increase in the number of myelinated axons as age progressed from P20 to P60, consistent with previous results (Wiggins, 1982). Mean myelin thickness remained unchanged and mean myelinated axon diameter decreased, yet both myelin fraction and myelinated axon fraction increased, driven primarily by the increase in myelinated axon density. The reduction in mean myelinated axon diameter does not necessarily indicate the axons are shrinking during development, but rather that oligodendrocytes generally myelinate larger axons before smaller ones (Nave and Salzer, 2006; Voyvodic, 1989). The Rictor model showed reduced myelin and axon fractions and axon density at P20 and P30, but these changes were less apparent at P60, in agreement with the moderate hypomyelination phenotype in adult mice previously reported (Carson et al., 2013; Kelm et al., 2016), but also indicating that myelination may be delayed in these animals during development before recovering to near normal levels in adult mice. The TSC model presented an even greater

reduction in myelinated axon density and axon and myelin fractions at each age (compared with controls), and showed minimal changes in these metrics between P20 and P60. From this, the TSC model can be characterized by extreme hypomyelination that persists into adulthood, consistent with previous studies (Carson et al., 2015; Kelm et al., 2016). Both the Rictor and TSC hypomyelination models present with reduced myelinated axon density, caused by a reduction in the number of mature oligodendrocytes, as opposed to hypomyelination due to decreases in myelin thickness. In contrast, the PTEN hypermyelination model exhibited increases in myelin thickness, in agreement with prior work (Harrington et al., 2010). However, histologic myelin fraction was only slightly higher than that in control mice due to small decreases in myelinated axon density. This is the first study to report EM-derived measures of axon and myelin microstructure for these models during development. Due to switching from a manual to an automated approach in the EM image analysis, measures of myelin thickness for adult mice reported in this work are significantly greater than those previously reported (Kelm et al., 2016) and may be slightly overestimated, yet more repeatable and user-independent.

Group-averaged DWI parameter maps shown in Figs. 5.3-5.5 allow for global assessments of both white matter and gray matter during normal development. From these, it was apparent that radial-associated DWI metrics exhibited greater changes from P20 to P60 than measures related to the axial direction. Consistent with previous work (Cheung et al., 2009), changes during development in white matter MK and RK appear to be much greater than those observed with MD and RD, and although change in AD were minimal, increases in white matter AK were readily apparent. Increases in the WMTI metric F_a as age increased from P20 to P60 were visibly noticeable, however alterations in compartmental diffusivities across age were minimal. Since the main microstructural change among the control brains in this study was an

increase in myelination, it can be inferred that the increase in F_a was primarily driven by a decrease in non-myelin water fraction (i.e., an increase in the "silent" myelin water) rather than an increase in intra-axonal water. This is the first study to assess the progression of WMTI metrics in normal brain at this stage of development.

This work utilized diffusion tractography to compare MRI parameters on a tract-wise basis across brain development, similar to the approach used by Lebel and coworkers (Lebel et al., 2008). During brain development, variable changes in the area of brain regions, in addition to overall brain size, make voxel-wise and ROI-based comparisons difficult to perform accurately and on a large scale, even with well-performing deformable registration. However, a tract-based approach alleviates these issues by evaluating MR metrics by tract, making it more robust to alterations in tract size and alignment across age, with the assumption that white matter is the structure of interest. Additionally, since white matter is typically defined by tracts (rather than regions, as with gray matter), it makes intuitive sense that white matter comparisons with MRI should be made on a tract-wise basis when possible. Finally, it is important to recognize that mean tract-specific measures should not be directly compared to those from 2D ROI analysis, since MR metrics can vary greatly within a given tract.

The tract-based DTI and DKI results shown in Figs. 5.7 and 5.8 confirm an increased sensitivity of DKI metrics over DTI metrics during both normal and abnormal white matter development. Also, the trends for DTI and DKI metrics across tracts were as expected in normal development characterized by increased myelination. One interesting observation is that DTI metrics FA and RD were less able to distinguish age-related changes in the internal capsule, an earlier-myelinating tract, in comparison with MK and RK. Although differences in FA and RD did exist between the CKO models and the control group at P60, differences at ages P20 and P30

were minimal. On the other hand, MK and RK exhibited a slightly improved ability to distinguish between the CKO models, even at the younger ages. This means that the increased sensitivity of DKI makes it a promising diagnosis tool for assessing the progression of abnormal white matter development, as well as treatment efficacy. Additionally, the increased sensitivity of RK over MK signifies the importance of utilizing directional kurtosis analysis in white matter evaluation. Lastly, although an increase in myelination is the primary change in this stage of normal development, increases in AK were also observed, possibly indicating the presence of other microstructural changes such as axonal pruning (Semple et al., 2013).

The biophysical white matter model WMTI offers unique information and the potential for improved specificity over the DTI and DKI models. Tract-based measures of F_a displayed in Fig. 5.9 show similar trends to those seen in MK and RK, as expected, since F_a and RK are closely related. On the other hand, changes in $D_{e,\perp}$ during development seem less intuitive. Based on previous work (Jelescu et al., 2016b; Kelm et al., 2016), an increase in myelin content would be expected to cause a small decrease in $D_{e,\perp}$. Although this was true for the PTEN model, for the control, Rictor, and TSC groups, slight increases in $D_{e,\perp}$ were observed as age increased from P20 to P60. This minor shift could potentially be due to axonal pruning, which would theoretically reduce diffusion restrictions in the extracellular space as unnecessary axons are eliminated. The thicker myelin sheaths present in the PTEN model may explain why this group behaved differently from the others, indicating that $D_{e,\perp}$ may be useful for evaluating differences in myelin thickness.

Tract-based comparisons can be extended beyond DWI metrics to other MRI measures of white matter microstructure, in this case, MWF from MET_2 and PSR from qMT. This approach, termed “tractometry”, was first proposed by Bells et al. (Bells et al., 2011), yet has not been

previously used to assess brain development. The group comparisons from Fig. 5.10 indicate that both MWF and PSR were able to detect the increase in myelination during development, as well as differences between normal and abnormal myelination. In fact, in normally-developing brain, PSR was highly sensitive and able to detect increased myelination in all tracts from P20 to P30 to P60. Compared to PSR, MWF increases across age were not as consistent, particularly in the corpus callosum. This may be attributed to some erroneously high MWF values caused by susceptibility artifacts in white matter adjacent to large ventricles (e.g., the lateral ventricle just inferior to the corpus callosum). Lastly, the PTEN model showed similar PSR to the control group, but much higher MWF. Considering that the PTEN model exhibited similar histologic myelin fraction, yet greater myelin thickness, it can be inferred that MWF is sensitive to variations in myelin thickness whereas PSR is not, in agreement with previous work (Dula et al., 2010; Harkins et al., 2011).

Linear correlations shown in Fig. 5.11 and Table 5.2 indicate strong correlations existing between DWI metrics and histologic metrics across normal and abnormal development. As expected, since myelination was the primary variable across groups, MD, RD, MK, and RK exhibited significant correlations whereas AD and AK did not. Generally, RD and RK showed stronger correlations with myelin content (i.e., f_m and ρ_a) compared to axon measures (i.e., f_a and d_a), indicating some degree of specificity to myelin. None of these DWI measures correlated with myelin thickness, signifying that they are sensitive to the overall amount of myelin present as opposed to variations in myelin thickness. Fig. 5.11 also shows that F_a closely approximates the histologic axon fraction (with myelin fraction removed) for the control and PTEN groups at P30 and P60 and the Rictor group at P60, or when myelinated axon density is greater, yet overestimates it for each model at P20 and for the TSC model at all ages, when myelinated axon

density is low. This overestimation may be attributed to a large number of unmyelinated axons present in these groups that are not included in the histologic axon fraction measurement, yet contribute to F_a. $D_{e,\perp}$ did not correlate significantly with the histologic measures from this study, although a trend of decreasing $D_{e,\perp}$ with increasing myelin thickness was observed. Previous studies have proposed $D_{e,\perp}$ to be specific to demyelination or myelin thickness (Fieremans et al., 2012; Jelescu et al., 2016b). In this study, the decrease in $D_{e,\perp}$ present in the PTEN model at P60 does support this, yet the lack of strong correlation with myelin thickness also indicates that $D_{e,\perp}$ may be limited by its sensitivity. The correlations between DWI metrics and histology observed in brain development were similar to those reported in adult hypomyelinated mice in Chapter 3. From this, it can be inferred that the relationships between DWI and microstructure reported in this work are also applicable to a wider range of studies outside of brain development alone.

As anticipated, strong correlations were observed between the myelin-associated MR metrics, MWF and PSR, and myelin content. Additionally, only weak correlations were observed with axon-related histology metrics, validating the increased specificity of MWF and PSR to myelin. Surprisingly, the strong correlations with f_m and ρ_a were similar to those shown by DWI metrics, which supports the idea that DWI is highly sensitive to changes in myelination, on the same level as MWF and PSR, although not as specific.

Previous studies assessing DKI and WMTI during development, as well as histologic evaluation of these metrics at any age, have been limited. Cheung and coworkers examined changes in DTI and DKI metrics during rat brain development, finding that DKI offered greater sensitivity and complementary information compared to DTI (Cheung et al., 2009). Another study assessed a Huntington's disease model in rats at ages P15 and P30 with DKI and myelin basic protein immunohistochemistry, observing increases in kurtosis and myelin basic protein as

age increased (Blockx et al., 2012). Previous work (see Chapter 3) compared DKI and WMTI metrics to quantitative histology of myelin and axon morphology in adult transgenic mouse models of hypomyelination, observing a close relationship between DKI and myelin content (Kelm et al., 2016). Another study evaluated DKI and WMTI metrics in a cuprizone mouse model of demyelination and found correlations between these measures and solochrome staining for myelin (Falangola et al., 2014). Additionally, Jelescu and coworkers compared WMTI metrics to EM histology in the cuprizone model, observing that axonal water fraction correlated with histologic axon fraction and $D_{e,\perp}$ correlated with g-ratio (Jelescu et al., 2016b). Lastly, WMTI was utilized to assess brain development in humans from birth to 3 years, finding an increase in axonal water fraction as a function of age (Jelescu et al., 2015). However, the current study is the first to compare DKI and WMTI measures to those derived from EM histology during brain development. Additionally, this work is the first to evaluate WMTI metrics during brain development from childhood to adulthood.

While they are extremely sensitive to white matter microstructure, diffusion signal models, such as DTI and DKI, are limited in their specificity. Both the DTI and DKI models are unable to properly characterize the multiple tissue compartments present in white matter. However, biophysical models of diffusion in white matter, such as CHARMED (Assaf et al., 2004), NODDI (Zhang et al., 2012), and WMTI, separately characterize intra- and extra-axonal spaces and show promise in providing specific information about axon and myelin microstructure. While promising, these models also come with their own set of limitations, such as *a priori* assumptions about tissue structure, low precision from non-linear fits, and bias due to the presence of multiple local minima (Jelescu et al., 2016a). In this study, WMTI did provide reasonable estimates of axonal water fraction and increased specificity to changes in myelin

thickness, making it a useful complement to the DTI and DKI models. Both signal models and biophysical models of diffusion have the ability to provide valuable information regarding white matter microstructure that can be helpful in the diagnosis and treatment of white matter disorders.

Another limitation of this study is that it was performed on *ex vivo* mouse brain as opposed to a longitudinal study across development. *Ex vivo* brain tissue has previously been shown to exhibit decreased diffusivity and increased kurtosis compared to *in vivo* measurements due to chemical fixation (Hui et al., 2008; Sun et al., 2003). Also, different fixative solutions have been shown to have a variable effect on both relaxation and diffusion in tissue (Shepherd et al., 2009). Additionally, tissue fixation may result in variable shrinking or distortion of microstructure that could affect the EM measures of axon and myelin morphology (Fox et al., 1985). Therefore, caution should be used when comparing these results to *in vivo* DWI assessments of brain development. Finally, since different animals had to be used for each time point, a direct comparison across age for an individual animal was not possible. Although difficult to perform, an *in vivo* longitudinal study would be useful to validate the results from this study and allow for improved assessment of potential treatments.

Making direct comparisons between MRI parameters and histological measures also has limitations. First, choosing the same ROI for both MRI and EM is difficult, especially when myelination is low and contrast between white matter and gray matter is decreased (both in MR images and toluidine blue-stained sections). In this study, the curve in the superior end of the fornix was used as a landmark to determine the location of the MidCC ROI, since this was clearly visible in both MR images and light microscopy images of the thick histology section. Even if it assumed that the ROIs are completely aligned, the thickness of the EM section (~70

nm) is still orders of magnitude smaller than any dimension of an MR voxel, so the white matter microstructure can never be perfectly matched between the two modalities. Additionally, to make the study time-feasible, the cumulative FOV of the images collected for EM measurements was much smaller than the area of the entire ROI, making it important to consider intra-tract variability when determining how much EM data is necessary.

5.5 Conclusions

DKI exhibited greater sensitivity to developmental changes in white matter compared with DTI. Furthermore, DKI demonstrated improved capability in distinguishing between normally-developing and abnormally-developing mouse brain. Quantitative histology revealed that the primary change in this stage of brain development was an increase in the number of myelinated axons, indicating that DKI can better report on myelin content. The biophysical WMTI model provided increased microstructural specificity through moderately accurate estimates of axon water fraction and improved reporting on myelin thickness differences with extra-axonal radial diffusivity, although this metric was limited by low sensitivity. Myelin-associated MR metrics, MWF and PSR, correlated strongly with total myelin content, with MWF measures also demonstrating sensitivity to differences in myelin thickness. In general, the relationships between DWI and WM microstructure during the complex process of brain development were similar to those observed in adult mice with abnormal myelination, indicating that these associations are applicable to a wide array of white matter changes.

5.6 Acknowledgements

The author thanks Brittany Parker for technical assistance with animal husbandry and Janice Williams, Ph.D., of the VUMC Cell Imaging Shared Resource for assistance with microscopy. Processing of EM sections and EM image collection were performed through the use of the VUMC Cell Imaging Shared Resource, supported by NIH grants CA68485, DK20593, DK58404, HD15052, DK59637, and EY008126. This work was also supported by NIH grants R01 EB001744, R01 EB019980, 5K08 NS050484, and S10 RR029523.

5.7 References

Andersson, J.L., Jenkinson, M., Smith, S., 2007. Non-linear registration, aka Spatial normalisation FMRIB technical report TR07JA2. FMRIB Analysis Group of the University of Oxford 2.

Assaf, Y., Freidlin, R.Z., Rohde, G.K., Basser, P.J., 2004. New modeling and experimental framework to characterize hindered and restricted water diffusion in brain white matter. Magn. Reson. Med. 52, 965–978.

Barnea-Goraly, N., Kwon, H., Menon, V., Eliez, S., Lotspeich, L., Reiss, A.L., 2004. White matter structure in autism: preliminary evidence from diffusion tensor imaging. Biol. Psychiatry 55, 323–326.

Basser, P.J., Mattiello, J., LeBihan, D., 1994. MR diffusion tensor spectroscopy and imaging. Biophys. J. 66, 259–267.

Beaulieu, C., 2002. The basis of anisotropic water diffusion in the nervous system - a technical review. NMR Biomed. 15, 435–455. doi: 10.1002/nbm.782

Bells, S., Cercignani, M., Deoni, S., Assaf, Y., Pasternak, O., Evans, C.J., Leemans, A., Jones, D.K., 2011. Tractometry–comprehensive multi-modal quantitative assessment of white matter along specific tracts. 19th Annual Meeting of the International Society for Magnetic Resonance in Medicine, Montreal, Canada. 678.

Benes, F.M., Turtle, M., Khan, Y., Farol, P., 1994. Myelination of a key relay zone in the hippocampal formation occurs in the human brain during childhood, adolescence, and adulthood. Arch. Gen. Psychiatry 51, 477–484.

Blockx, I., De Groof, G., Verhoye, M., Van Audekerke, J., Raber, K., Poot, D., Sijbers, J.,

Osmand, A.P., Hörsten, Von, S., Van der Linden, A., 2012. Microstructural changes observed with DKI in a transgenic Huntington rat model: evidence for abnormal neurodevelopment. NeuroImage 59, 957–967.

Brody, B.A., Kinney, H.C., Kloman, A.S., Gilles, F.H., 1987. Sequence of central nervous system myelination in human infancy. I. An autopsy study of myelination. J. Neuropathol. Exp. Neurol. 46, 283–301.

Carson, R.P., Fu, C., Winzenburger, P., Ess, K.C., 2013. Deletion of Rictor in neural progenitor cells reveals contributions of mTORC2 signaling to tuberous sclerosis complex. Hum. Mol. Gen. 22, 140–152. doi: 10.1093/hmg/dds414

Carson, R.P., Kelm, N.D., West, K.L., Does, M.D., Fu, C., Weaver, G., McBrier, E., Parker, B., Grier, M.D., Ess, K.C., 2015. Hypomyelination following deletion of Tsc2 in oligodendrocyte precursors. Ann. Clin. Transl. Neurol. 12, 1041–1054. doi: 10.1002/acn3.254

Cheung, M.M., Hui, E.S., Chan, K.C., Helpern, J.A., Qi, L., Wu, E.X., 2009. Does diffusion kurtosis imaging lead to better neural tissue characterization? A rodent brain maturation study. NeuroImage 45, 386–392. doi: 10.1016/j.neuroimage.2008.12.018

Davis, K.L., Stewart, D.G., Friedman, J.I., Buchsbaum, M., Harvey, P.D., Hof, P.R., Buxbaum, J., Haroutunian, V., 2003. White matter changes in schizophrenia: evidence for myelin-related dysfunction. Arch. Gen. Psychiatry 60, 443–456. doi: 10.1001/archpsyc.60.5.443

Dula, A.N., Gochberg, D.F., Valentine, H.L., Valentine, W.M., Does, M.D., 2010. Multiexponential T2, magnetization transfer, and quantitative histology in white matter tracts of rat spinal cord. Magn. Reson. Med. 63, 902–909. doi: 10.1002/mrm.22267

Falangola, M.F., Guilfoyle, D.N., Tabesh, A., Hui, E.S., Nie, X., Jensen, J.H., Gerum, S.V., Hu, C., LaFrancois, J., Collins, H.R., Helpern, J.A., 2014. Histological correlation of diffusional kurtosis and white matter modeling metrics in cuprizone-induced corpus callosum demyelination. NMR Biomed. 27, 948–957. doi: 10.1002/nbm.3140

Fieremans, E., Jensen, J.H., Helpern, J.A., Kim, S., Grossman, R., Inglese, M., 2012. Diffusion distinguishes between axonal loss and demyelination in brain white matter. 20th Annual Meeting of the International Society for Magnetic Resonance in Medicine. Melbourne, Australia. 465.

Flynn, S.W., Lang, D.J., MacKay, A.L., Goghari, V., Vavasour, I.M., Whittall, K.P., Smith, G.N., Arango, V., Mann, J.J., Dwork, A.J., 2003. Abnormalities of myelination in schizophrenia detected in vivo with MRI, and post-mortem with analysis of oligodendrocyte proteins. Mol. Psychiatry 8, 811–820.

Fox, C.H., Johnson, F.B., Whiting, J., Roller, P.P., 1985. Formaldehyde fixation. J. Histochem. Cytochem. 33, 845–853.

Gochberg, D.F., Gore, J.C., 2007. Quantitative magnetization transfer imaging via selective inversion recovery with short repetition times. Magn. Reson. Med. 57, 437–441.

Harkins, K.D., Dula, A.N., Does, M.D., 2011. Effect of intercompartmental water exchange on the apparent myelin water fraction in multiexponential T2 measurements of rat spinal cord. Magn. Reson. Med. 67, 793–800. doi: 10.1002/mrm.23053

Harrington, E.P., Zhao, C., Fancy, S.P.J., Kaing, S., Franklin, R.J.M., Rowitch, D.H., 2010. Oligodendrocyte PTEN is required for myelin and axonal integrity, not remyelination. Ann. Neurol. 68, 703–716. doi: 10.1002/ana.22090

Hui E.S., Cheung M.M., Qi L, Wu E.X., 2008. Towards better MR characterization of neural tissues using directional diffusion kurtosis analysis. NeuroImage 42, 122-134.

Jelescu, I.O., Veraart, J., Adisetiyo, V., Milla, S.S., Novikov, D.S., Fieremans, E., 2015. One diffusion acquisition and different white matter models: how does microstructure change in human early development based on WMTI and NODDI? NeuroImage 107, 242–256. doi: 10.1016/j.neuroimage.2014.12.009

Jelescu, I.O., Veraart, J., Fieremans, E., Novikov, D.S., 2016a. Degeneracy in model parameter estimation for multi-compartmental diffusion in neuronal tissue. NMR Biomed. 29, 33–47.

Jelescu, I.O., Zurek, M., Winters, K.V., Veraart, J., Rajaratnam, A., Kim, N.S., Babb, J.S., Shepherd, T.M., Novikov, D.S., Kim, S.G., 2016b. In vivo quantification of demyelination and recovery using compartment-specific diffusion MRI metrics validated by electron microscopy. NeuroImage 132, 104–114.

Jenkinson, M., Bannister, P., Brady, M., Smith, S., 2002. Improved optimization for the robust and accurate linear registration and motion correction of brain images. NeuroImage 17, 825–841.

Jenkinson, M., Smith, S., 2001. A global optimisation method for robust affine registration of brain images. Med. Image Anal. 5, 143–156.

Kelm, N.D., West, K.L., Carson, R.P., Gochberg, D.F., Ess, K.C., Does, M.D., 2016. Evaluation of diffusion kurtosis imaging in ex vivo hypomyelinated mouse brains. NeuroImage 124, 612–626. doi: 10.1016/j.neuroimage.2015.09.028

Koenig, S.H., Brown, R.D., Spiller, M., Lundbom, N., 1990. Relaxometry of brain: why white matter appears bright in MRI. Magn. Reson. Med. 14, 482–495.

Kucharczyk, W., Macdonald, P.M., Stanisz, G.J., Henkelman, R.M., 1994. Relaxivity and magnetization transfer of white matter lipids at MR imaging: importance of cerebrosides and pH. Radiology 192, 521–529.

Lebel, C., Walker, L., Leemans, A., Phillips, L., Beaulieu, C., 2008. Microstructural maturation of the human brain from childhood to adulthood. NeuroImage 40, 1044–1055. doi: 10.1016/j.neuroimage.2007.12.053

Leemans, A., Jeurissen, B., Sijbers, J., Jones, D.K., 2009. ExploreDTI: a graphical toolbox for processing, analyzing, and visualizing diffusion MR data. 17th Annual Meeting of the International Society for Magnetic Resonance in Medicine, Honolulu, Hawaii. 3537.

MacKay, A., Whittall, K., Adler, J., Li, D., Paty, D., Graeb, D., 1994. In vivo visualization of myelin water in brain by magnetic resonance. Magn. Reson. Med. 31, 673–677.

Menon, R.S., Rusinko, M.S., Allen, P.S., 1992. Proton relaxation studies of water compartmentalization in a model neurological system. Magn. Reson. Med. 28, 264–274.

Nave, K.-A., Salzer, J.L., 2006. Axonal regulation of myelination by neuregulin 1. Curr. Opin. Neurobiol. 16, 492–500.

Neil, J., Miller, J., Mukherjee, P., Hüppi, P.S., 2002. Diffusion tensor imaging of normal and injured developing human brain-a technical review. NMR Biomed. 15, 543–552.

Paxinos, G., Franklin, K.B., 2004. The mouse brain in stereotaxic coordinates. Gulf Professional Publishing.

Paydar, A., Fieremans, E., Nwankwo, J.I., Lazar, M., Sheth, H.D., Adisetiyo, V., Helpern, J.A., Jensen, J.H., Milla, S.S., 2014. Diffusional kurtosis imaging of the developing brain. AJNR Am. J. Neuroradiol. 35, 808–814.

Semple, B.D., Blomgren, K., Gimlin, K., Ferriero, D.M., Noble-Haeusslein, L.J., 2013. Brain development in rodents and humans: identifying benchmarks of maturation and vulnerability to injury across species. Prog. Neurobiol. 106, 1–16.

Shepherd, T.M., Thelwall, P.E., Stanisz, G.J., Blackband, S.J., 2009. Aldehyde fixative solutions alter the water relaxation and diffusion properties of nervous tissue. Magn. Reson. Med. 62, 26–34. doi: 10.1002/mrm.21977

Sled, J.G., Pike, G.B., 2000. Quantitative interpretation of magnetization transfer in spoiled gradient echo MRI sequences. J. Magn. Reson. 145, 24–36. doi: 10.1006/jmre.2000.2059

Smith, S.M., Jenkinson, M., Woolrich, M.W., Beckmann, C.F., Behrens, T.E., Johansen-Berg, H., Bannister, P.R., De Luca, M., Drobnjak, I., Flitney, D.E., 2004. Advances in functional and structural MR image analysis and implementation as FSL. NeuroImage 23, S208–S219.

Sun, S.-W., Neil, J.J., Song, S.-K., 2003. Relative indices of water diffusion anisotropy are equivalent in live and formalin-fixed mouse brains. Magn. Reson. Med. 50, 743–748.

Voyvodic, J.T., 1989. Target size regulates calibre and myelination of sympathetic axons. Nature

342, 430–433.

Wiggins, R.C., 1982. Myelin development and nutritional insufficiency. Brain Res. Rev. 4, 151–175.

Yakovlev, P.I., Lecours, A.-R., 1967. The myelogenetic cycles of regional maturation of the brain. Regional development of the brain in early life 3–70.

Zhang, H., Schneider, T., Wheeler-Kingshott, C.A., Alexander, D.C., 2012. NODDI: practical in vivo neurite orientation dispersion and density imaging of the human brain. NeuroImage 61, 1000–1016.

CHAPTER 6

DIFFUSION KURTOSIS IMAGING OF PERIPHERAL NERVE INJURY AND REPAIR

6.1 Introduction

Although acute peripheral nerve injury is relatively common in the clinical setting, accurate non-invasive diagnosis tools are limited. Current non-invasive methods, such as electrophysiological testing and physical examination, are often unable to determine the extent of nerve injury, and in these cases, exploratory surgery is required to determine whether the nerve is in need of surgical repair (Gaudet et al., 2011; Grant et al., 1999). Additionally, due to Wallerian degeneration, the surgical outcome of peripheral nerve repair is largely unknown until the nerve regenerates and reinnervates the target muscle, which could take on the order of months. By the time this occurs, it may be too late for corrective surgery to be effective, so therefore, early assessment of nerve regeneration is critical (Campbell, 2008).

Peripheral nerve injury and subsequent Wallerian degeneration involve complex microstructural changes, including demyelination/remyelination, axon loss and regeneration, edema, and inflammation, making it important for diagnostic tools to be sensitive and specific to each of these processes. Even though MR imaging is not currently the clinical standard for peripheral nerve injury assessment, there has been previous work investigating the feasibility of utilizing MRI to image peripheral nerve. Standard T_2-weighted MRI has been proposed for imaging peripheral nerve injury, since injured regions appear hyperintense due to increased T_2 attributed to edema (Bendszus and Stoll, 2005; Bendszus et al., 2004; Does and Snyder, 1996). However, although this approach may be able to determine the presence of an injury, it lacks in

specificity as far as determining the extent of the injury (e.g., crush or transection) or whether nerve regeneration is taking place. In contrast, diffusion-weighted MRI (DWI) may be able to provide improved sensitivity and specificity to the various stages of nerve injury and repair.

DWI involves the sensitization of the MRI signal to the random displacement of water molecules in a given medium, which in peripheral nerve, is largely influenced by microstructural tissue components such as axonal membranes and myelin. DTI describes the directional dependence of diffusion through rotationally invariant metrics FA, MD, AD, and RD (Basser and Jones, 2002; Basser et al., 1994a; 1994b; Beaulieu, 2002; Le Bihan et al., 2001). Diffusion is highly anisotropic in peripheral nerve, making DTI especially suitable for nerve characterization. DTI has been previously applied to peripheral nerve imaging, observing changes in FA and diffusivity due to injury, as well as utilizing DTI tractography to visualize peripheral nerve injury and regeneration (Beaulieu et al., 1996; Boyer et al., 2015; Guggenberger et al., 2012; Lehmann et al., 2010; Li et al., 2013; Morisaki et al., 2011). However, DTI uses a single compartment diffusion signal model based on a Gaussian approximation of free diffusion, limiting its specificity in a heterogeneous environment, such as injured peripheral nerve.

Diffusion kurtosis imaging is an extension of the DTI model that provides additional information regarding the heterogeneity of tissue microstructure (Hui et al., 2008; Jensen and Helpern, 2010; Jensen et al., 2005; Lu et al., 2006; Wu and Cheung, 2010), including improved assessment of myelination (Cheung et al., 2009; Kelm et al., 2016). Analogous to DTI, diffusion kurtosis can be described in three dimensions by a kurtosis tensor, from which MK, AK, and RK can be extracted. In addition, DKI also utilizes a single-compartment model of the DWI signal that exhibits limited specificity to multiple tissue compartments, such as intra- and extra-cellular spaces. In contrast, the biophysical DKI-based WMTI model is a multi-compartment model of

intra- and extra-axonal spaces that may provide improved specificity to peripheral nerve injury (Fieremans et al., 2011). WMTI uses the diffusion and kurtosis tensors to separate nervous tissue into intra- and extra-axonal spaces, so that the following parameters can be derived: axonal water fraction (F_a), intra-axonal diffusivity (D_a), and axial and radial diffusivity ($D_{e,\parallel}$ and $D_{e,\perp}$, respectively). Previous work has associated F_a with axonal loss, D_a and $D_{e,\parallel}$ with axon structure, and $D_{e,\perp}$ with myelination (Falangola et al., 2008; Fieremans et al., 2013; Jelescu et al., 2016; Kelm et al., 2016). Both the DKI and WMTI models have not been previously applied to peripheral nerve imaging.

The objective of this study was to evaluate the performance of DTI, DKI, and WMTI metrics in characterizing an acute peripheral nerve injury model in rodents at various time points after surgical repair. The process of Wallerian degeneration and nerve regeneration is commonly modeled in rat sciatic nerve through a crush or transection injury. In this study, rat sciatic nerves were completely transected, immediately repaired, and then excised at time points spanning from 1 hour to 6 weeks post-repair (i.e., the entirety of the degeneration/regeneration process). DWI metrics were then measured in excised sciatic nerves at each time point in order to better understand the relationship of these parameters to the complex process of nerve injury and repair.

6.2 Materials and Methods

For this study, a total of 20 adult female Sprague-Dawley rats were used. After transection injury and repair, nerves were harvested at time points of 1 hour, 3 days, 1 week, 3 weeks, and 6 weeks post-surgery (N = 4 for each time point) The methods for nerve preparation, MR imaging, and data analysis were as described in Section 2.2.

6.3 Results

6.3.1 DTI

Figure 6.1 shows representative parameter maps of DTI metrics FA, MD, AD, and RD for injured sciatic nerves at each time point. As anticipated, qualitatively, there were minimal differences in these parameters in the proximal ends of the nerves, although it does appear that diffusivity was increased in this region 3 days post-injury. At the injury site, FA is noticeably reduced through 3 weeks post-injury, but closer to normal after 6 weeks. Also, apparent decreases in AD and increases in RD were observed as soon as 1 hour after the injury, and although approaching normal values by 6 weeks, AD and RD were still reduced and increased compared to normal nerve, respectively. Changes in MD at the injury site are not visually obvious. Distal to the injury, FA appears slightly reduced beginning at 3 days and is lowest at 3 weeks, yet seems mostly normal at 6 weeks. Also, RD is noticeably increased by 3 days and

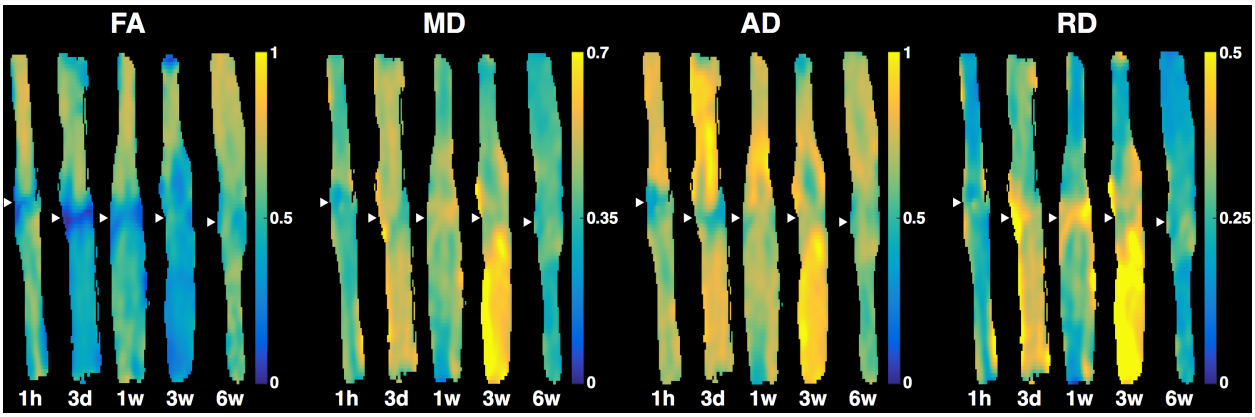

FIG. 6.1. Representative DTI parameter maps of injured sciatic nerves. Parameter maps of FA, MD, AD, and RD (left to right) are shown for nerves from each group. Time points are indicated below each nerve: 1h = 1 hour, 3d = 3 days, 1w = 1 week, 3w = 3 weeks, and 6w = 6 weeks. White arrows point to the injury site for each nerve. FA is unitless and diffusivities are in units of $\mu m^2/ms$.

much higher than normal levels at 3 weeks, before returning to normal at 6 weeks. Distal AD appears mostly unaffected except for a slight increase at the 3-week time point. MD showed changes similar to RD distal to the injury, yet these are not as visually apparent.

The results of the ROI analysis for DTI metrics are shown in Fig. 6.2. First, few changes

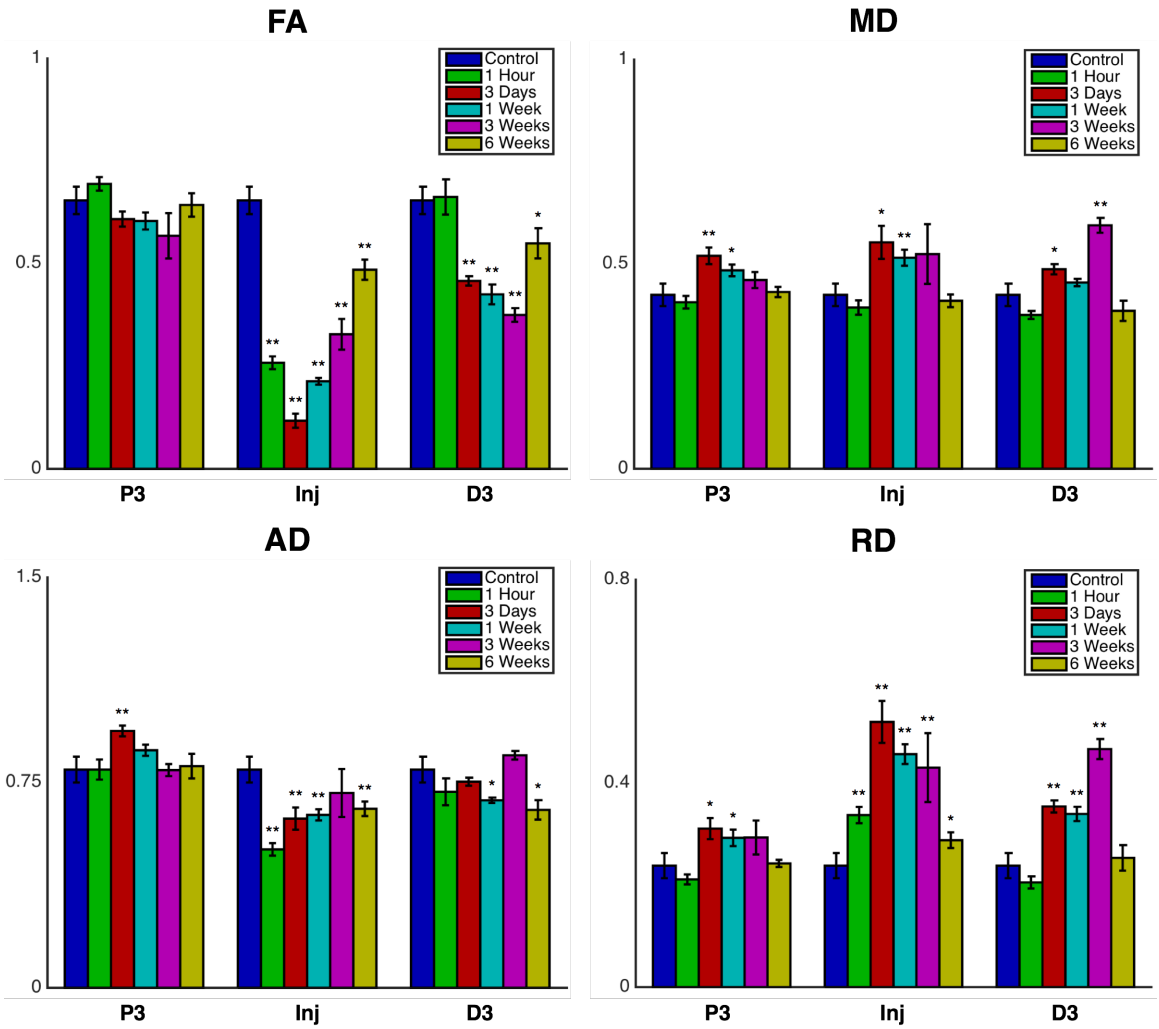

FIG. 6.2. ROI group comparison of DTI parameters FA, MD, AD, and RD. Bar heights represent the ROI parameter means across each group, with error bars spanning the mean ± SEM. The 6 groups are represented with different colors: control = blue, 1 hour = green, 3 days = red, 1 week = cyan, 3 weeks = magenta, and 6 weeks = yellow. The 3 location ROIs are indicated on the x-axis: P3 = 3 mm proximal to the injury site, Inj = injury site, and D3 = 3 mm distal to the injury site. FA is unitless and diffusivities are in units of $\mu m^2/ms$. * denotes $p < 0.05$ and ** denotes $p < 0.01$ for comparison between the control group and each injury group.

were seen in the proximal end, except for significant increases in diffusivity observed at 3 days and 1 week. At the injury site, FA was greatly reduced as soon as 1 hour after injury, decreased even more by 3 days, and then steadily increased through 6 weeks. However, even 6 weeks post-injury, FA was still lower at the injury site than normal nerve. 3 mm distal to the injury, a significant reduction in FA was shown at 3 days, and it continued to decrease until 3 weeks. At 6 weeks, distal FA is closer to normal, yet similar to the injury site, was still lower than that in normal nerve. AD at the injury site was greatly reduced as soon as 1 hour after the surgery, but then steadily increased through 6 weeks, although it remained lower than normal nerve. Distal to the injury site, minimal changes in AD were observed, except for a minor decrease by 6 weeks. In contrast to AD, RD was increased at the injury site immediately after the surgery, reached a peak at 3 days, before decreasing closer to normal levels by 6 weeks. For the 3-mm distal ROI, RD increased at 3 days and reached a peak at 3 weeks, yet was similar to normal nerve at 6 weeks. Since AD and RD demonstrated opposing trends, MD did not present with as many changes. However, there were increases in MD, both at the injury site and distal to the injury, from 3 days through 3 weeks.

6.3.2 DKI

Figure 6.3 shows maps of DKI parameters MK, AK, and RK for representative injured nerves at each time point. First, kurtosis appears to be similar across time points for the proximal section of the nerves. At the injury site, AK appears greatly increased after 1 hour and 3 days, before falling close to normal levels. On the other hand, RK seems to steadily decrease until 1 week post-surgery, then increase from 1 week to 6 weeks. Qualitatively, similar to AK, MK is increased at the injury site for the early time points. Distal to the injury, AK appears to be

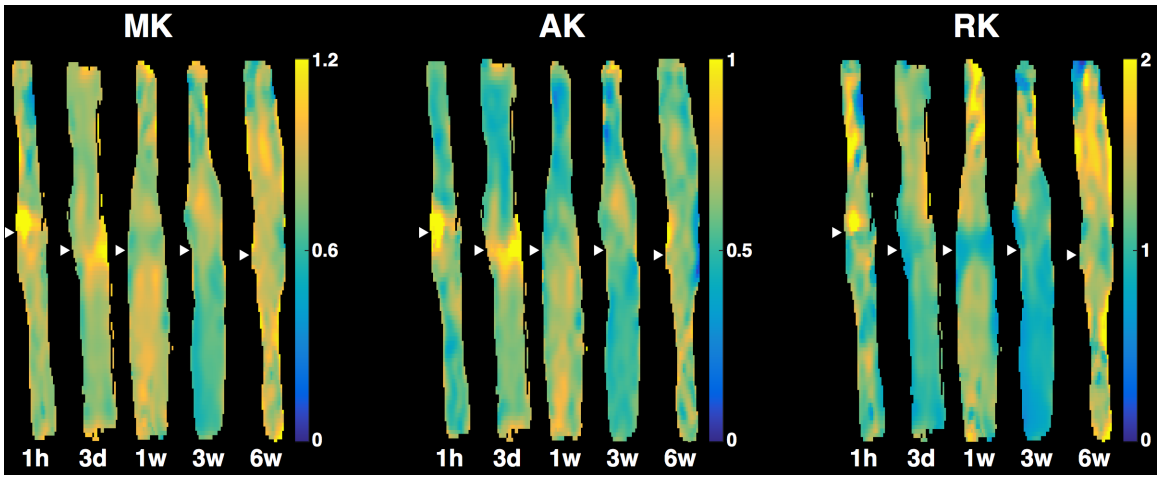

FIG. 6.3. Representative DKI parameter maps of injured sciatic nerves. Parameter maps of MK, AK, and RK (left to right) are shown for nerves from each group. Time points are indicated below each nerve: 1h = 1 hour, 3d = 3 days, 1w = 1 week, 3w = 3 weeks, and 6w = 6 weeks. White arrows point to the injury site for each nerve. Kurtosis is unitless.

increased at 3 days and 1 week, yet closer to normal at 3 weeks. Additionally, RK seems to decrease beginning 3 days post-surgery, reach a low point at 3 weeks, and return back to normal at 6 weeks. Changes in MK were not as apparent, although a decrease in MK is obvious at the 3-week time point.

ROI means and group comparisons of DKI metrics MK, AK, and RK are demonstrated in Fig. 6.4. MK in injured nerves remained similar to normal nerve, except for an increase 1 hour post-surgery at the injury site and a decrease distal to the injury at 3 weeks. On other hand, significant increases and decreases in AK and RK, respectively, were observed at the injury site. AK was highest at the 1-hour time point and RK was lowest at the 1-week time point. Both metrics returned closer to normal levels by 6 weeks, although they were still significantly different compared to the control group. 3 mm distal to the injury site, significant increases in AK were observed at the 3-day, 1-week, and 6-week time points and decreases in RK were shown from 3 days through 3 weeks, with the lowest RK observed at 3 weeks.

6.3.3 WMTI

WMTI parameter maps of representative nerves for each time point are displayed in Fig. 6.5. First, looking at the proximal end, changes in these metrics are not visually apparent, except for a slight decrease in F_a at 3 days post-injury. At the injury site, noticeable decreases in F_a, D_a, and

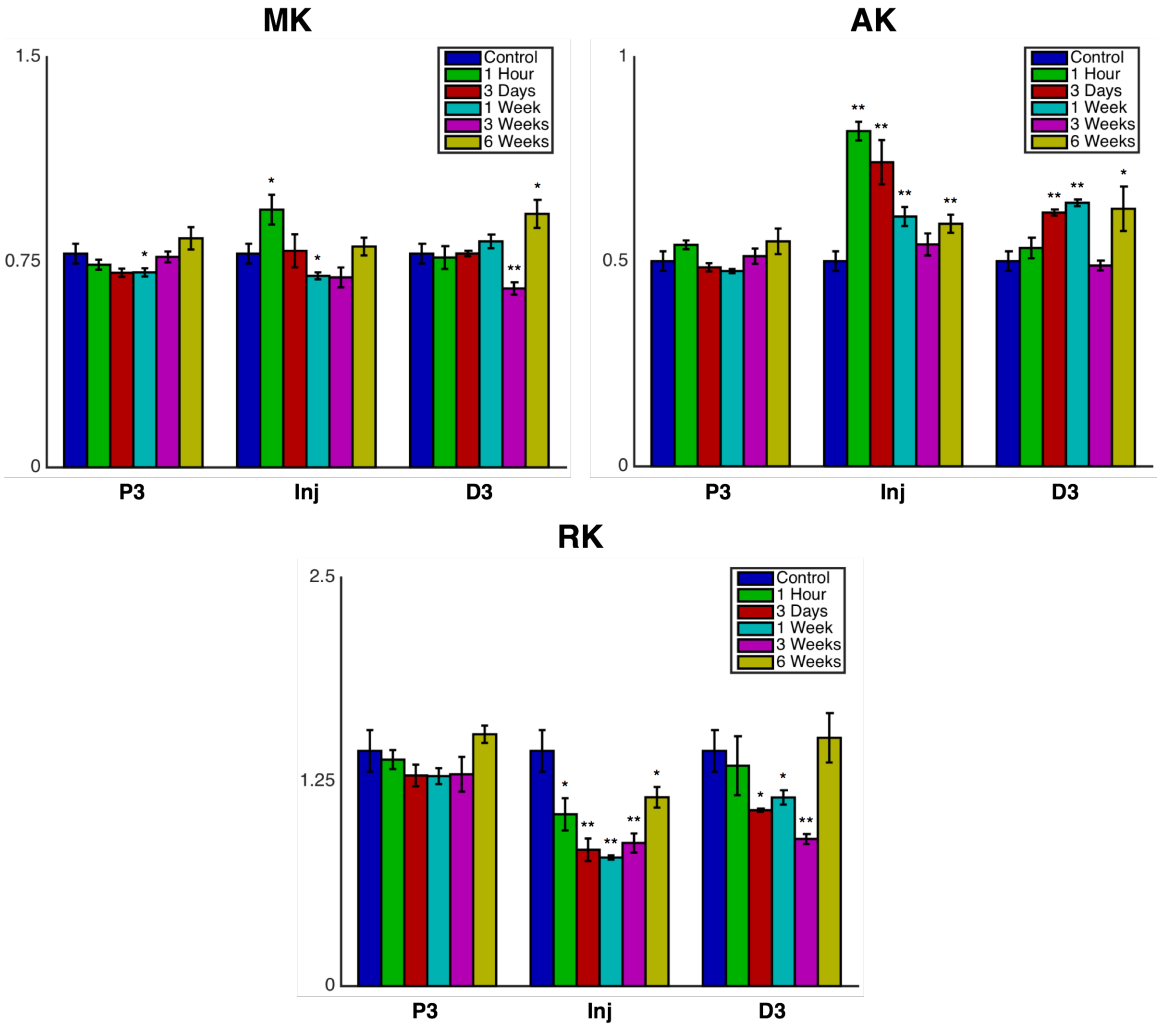

FIG. 6.4. ROI group comparison of DKI parameters MK, AK, and RK. Bar heights represent the ROI parameter means across each group, with error bars spanning the mean ± SEM. The 6 groups are represented with different colors: control = blue, 1 hour = green, 3 days = red, 1 week = cyan, 3 weeks = magenta, and 6 weeks = yellow. The 3 location ROIs are indicated on the x-axis: P3 = 3 mm proximal to the injury site, Inj = injury site, and D3 = 3 mm distal to the injury site. Kurtosis is unitless. * denotes $p < 0.05$ and ** denotes $p < 0.01$ for comparison between the control group and each injury group.

$D_{e,\parallel}$, and increases in $D_{e,\perp}$ were observed after 3 days. Also, $D_{e,\parallel}$ and $D_{e,\perp}$ appear to return close to normal by 6 weeks, yet F_a and $D_{e,\parallel}$ do not, although these metrics were trending towards normal. Distal to the injury, F_a and D_a are noticeably lower than normal from 3 days through 3 weeks. In contrast, $D_{e,\parallel}$ exhibited minimal differences compared to normal nerve. $D_{e,\perp}$ appears to be increased distal to the injury at the 3-day, 1-week, and 3-week time points.

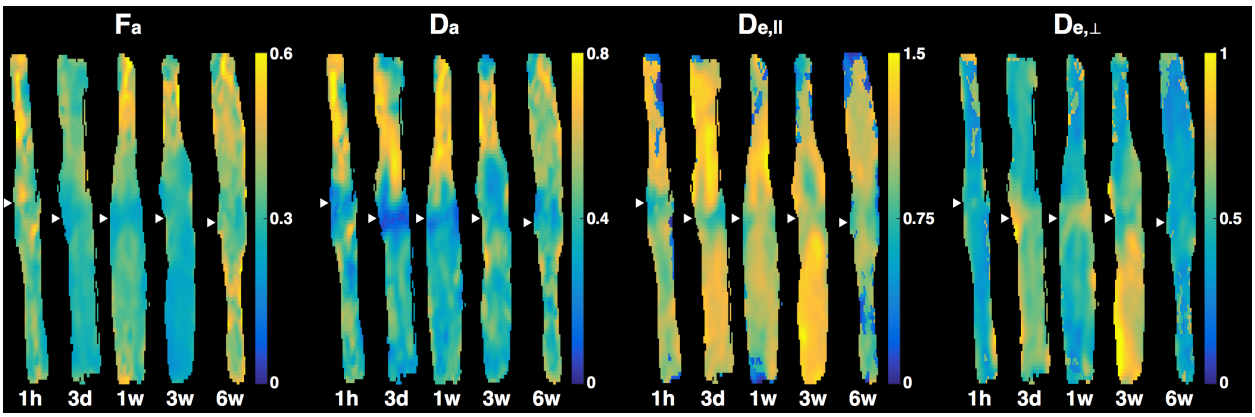

FIG. 6.5. Representative WMTI parameter maps of injured sciatic nerves. Parameter maps of F_a, D_a, $D_{e,\parallel}$, and $D_{e,\perp}$ (left to right) are shown for nerves from each group. Time points are indicated below each nerve: 1h = 1 hour, 3d = 3 days, 1w = 1 week, 3w = 3 weeks, and 6w = 6 weeks. White arrows point to the injury site for each nerve. F_a is unitless and diffusivities are in units of $\mu m^2/ms$.

Figure 6.6 shows group comparisons of WMTI metrics for each ROI location and injury time point. Group means at the 3-mm proximal ROI were similar to normal, except for a decrease in F_a and an increase in $D_{e,\parallel}$ at 3 days. At the injury site, F_a and D_a were significantly decreased at all time points, with the lowest at 3 days and the highest at 6 weeks. On the other hand, $D_{e,\parallel}$ was only decreased slightly 1 hour after injury and similar to the control group at all other time points. $D_{e,\perp}$ at the injury site showed opposite trends compared to F_a and D_a, as it was elevated from 1 hour through 3 weeks, with the highest value at 3 days post-injury. Lastly,

considering the distal ROI, F_a and D_a were significantly lower and $D_{e,\perp}$ significantly greater from 3 days through 3 weeks, whereas no significant differences were observed in $D_{e,\parallel}$. Additionally, although F_a and $D_{e,\perp}$ were restored to normal values by 6 weeks, D_a remained lower than normal even at this late time point.

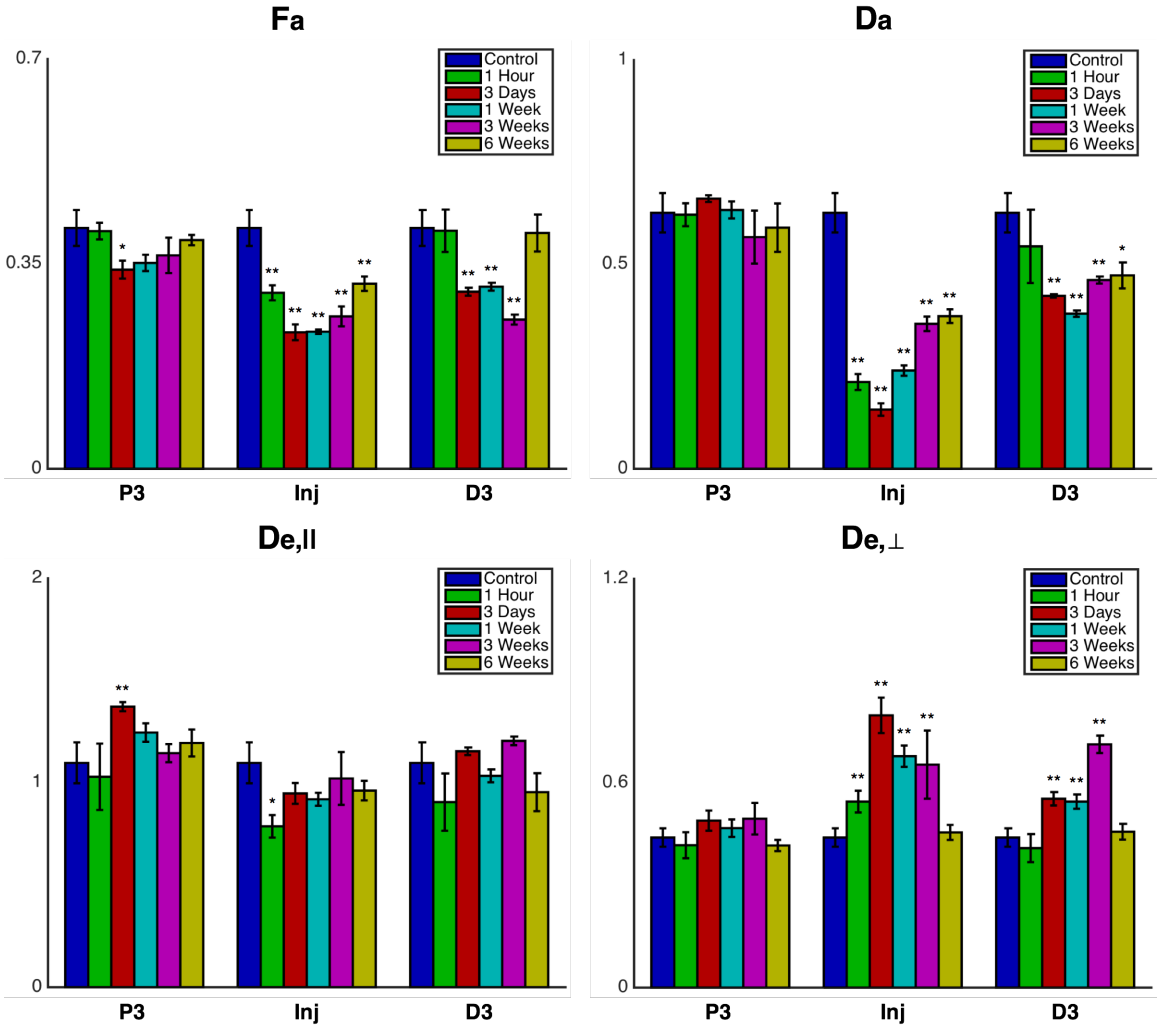

FIG. 6.6. ROI group comparison of WMTI parameters F_a, D_a, $D_{e,\parallel}$, and $D_{e,\perp}$. Bar heights represent the ROI parameter means across each group, with error bars spanning the mean ± SEM. The 6 groups are represented with different colors: control = blue, 1 hour = green, 3 days = red, 1 week = cyan, 3 weeks = magenta, and 6 weeks = yellow. The 3 location ROIs are indicated on the x-axis: P3 = 3 mm proximal to the injury site, Inj = injury site, and D3 = 3 mm distal to the injury site. F_a is unitless and diffusivities are in units of $\mu m^2/ms$. * denotes $p < 0.05$ and ** denotes $p < 0.01$ for comparison between the control group and each injury group.

6.4 Discussion

The DTI results reported in Figs. 6.1 and 6.2 were generally in agreement with previous work. At the injury site, FA was reduced immediately post-injury, driven by both decreases in axial diffusivity and increases in radial diffusivity. This outcome could potentially be caused by a disruption in axonal membranes, decreasing AD, and an influx of edema, increasing diffusivity in all directions (but relatively greater in the radial direction). As anticipated, the distal portion of the nerve remains unaffected at this short time point. At 3 days post-injury, which is characterized by edema, inflammation, and axon and myelin degeneration, FA is reduced even more at the injury site, despite a slight increase in AD, due to a large increase in radial diffusivity. The increases in AD and RD signify the continued accumulation of fluid, with the even greater increase in RD also indicating axon degeneration and demyelination may have occurred. In the distal portion of the nerve, FA is decreased at 3 days, driven by a large increase in RD. Since AD remained the same and RD, although increased, is still lower than at the injury site, disintegration of axonal membranes and potentially demyelination, rather than edema, appear to be the primary causes. From 3 days to 3 weeks, FA steadily increases at the injury site, caused by a decrease in RD and an unchanging AD. From this, it is difficult to disentangle whether the decrease in RD is caused by a decrease in edema, an increase in axonal membranes and myelination, or both. 3 mm distal to the injury site, there is not much change in DTI metrics between 3 days and 1 week, potentially indicating that most axonal degeneration has already occurred. However, between 1 week and 3 weeks, a sharp increase in RD possibly signifies that demyelination has occurred and axons have not regenerated far enough distally by 3 weeks. At 6 weeks, RD is much closer to that in normal nerve for both the injury site and 3 mm distal to it,

indicating that axon regeneration and myelination may be mostly complete. However, even at 6 weeks, FA and AD remain lower than normal at the injury site and distal to the injury, possibly meaning that there is increased axon dispersion or a reduction in the number of regenerated axons compared with normal nerve. Lastly, although changes at the proximal ROI were minimal as expected, there were slight increases in diffusivity at 3 days and 1 week, potentially due to edema. Although changes in MD were observed, AD and RD are more insightful metrics in tissue with highly anisotropic diffusion, such as peripheral nerve.

For the most part, DKI metrics in Figs. 6.3 and 6.4 showed opposing trends compared to their corresponding DTI parameters. Generally, during nerve degeneration, increased AK seems to correspond to axonal degeneration and decreased RK to demyelination, with the contrary true for regeneration. This is in agreement with previous work comparing radial kurtosis and brain myelination (Cheung et al., 2009; Kelm et al., 2016). Previous studies in brain imaging have shown that DKI metrics are more sensitive than DTI metrics. In this case, RD and RK exhibited similar sensitivity to microstructural changes, yet AK showed slightly increased sensitivity over AD to changes between each time point (based on rank-sum test between each group, data not shown). Also, at the proximal ROI, diffusivity changes outweighed changes in kurtosis, potentially indicating that kurtosis was less sensitive to the presence of edema. Additionally, the kurtosis values for this study were much lower than those observed in brain white matter. This can presumably be attributed to the larger axons present in peripheral nerve, causing the diffusion displacement distribution to be less peaked, resulting in lower kurtosis. Finally, although DTI and DKI parameters were highly sensitive to the underlying microstructural changes accompanying peripheral nerve injury and repair, these single compartment models demonstrate limited specificity.

In contrast to DTI and DKI, the WMTI metrics shown in Figs. 6.5 and 6.6 ideally characterize the intra- and extra-axonal spaces separately. F_a showed trends similar to radial kurtosis, indicating sensitivity to axonal loss and demyelination (since myelin is not accounted for in the WMTI model, a loss of myelin will increase non-axonal space, decreasing the axon water fraction). Additionally, even at 6 weeks, F_a is still lower than normal at the injury site, yet near normal distal to the injury, potentially indicating the presence of some edema or inflammation at the injury location. Large decreases in D_a were observed at the injury site just after surgery, most likely due to the severance of axon membranes. D_a reached its lowest value after 3 days at the injury site and after 1 week at the distal ROI, indicating that D_a was sensitive to the progression of axon degeneration. Additionally, minimal change in D_a occurred between 3 and 6 weeks, signifying that the remyelination occurring then had little affect on this metric. Therefore, D_a appears to be specific to axon injury and degeneration/regeneration. Also, after 6 weeks, D_a remained lower at the injury site and distal to the injury, possibly signifying increased axonal dispersion after regeneration. $D_{e,\parallel}$ remained mostly the same across ROIs and time points, However, an increase in $D_{e,\parallel}$ in the proximal ROI after 3 days suggests that $D_{e,\parallel}$ may be sensitive to edema, although this appears to conflict with a lack of change in this metric observed at the site of injury. Changes observed in $D_{e,\perp}$ were quite similar to those seen in RD. Considering that the changes in RD are attributed to the breakdown of axonal membranes and subsequent demyelination, making the intra-axonal space much smaller, changes in the extra-axonal radial diffusivity should theoretically be similar to those observed in the overall radial diffusivity. It should be noted that in a small percentage of voxels, due to relatively low SNR, estimation of the extra-axonal diffusion tensor failed, producing erroneous values for $D_{e,\parallel}$ and $D_{e,\perp}$ (visually apparent in Fig. 6.5).

Generally, DTI, DKI, and WMTI all demonstrated sensitivity to the progression of nerve degeneration/regeneration after a transection injury and repair. Although not inherently specific to tissue microstructure, DTI metrics AD and RD did show strong associations to axon and myelin structure, respectively. However, particularly near the injury site, edema appears to be a confounding factor in the interpretation of AD and RD (as well as FA), as has been previously observed (Boyer et al., 2015). In this study, DKI metrics did not seem to provide much additional information over conventional DTI metrics, except moderate improvements in sensitivity to changes in axon structure between time points with AK. WMTI did appear to provide improved specificity over DTI and DKI, in particular, D_a seems more specific to changes in the axon microstructure, even in the presence of confounding factors such as edema.

One primary limitation of this study is the absence of histology to correlate with DWI metrics. Although difficult to obtain, histologic measures of axon and myelin microstructure would provide validation for the proposed relationships between these DWI models and the underlying tissue. Even though previous studies have reported histological analyses of the Wallerian degeneration/regeneration process, the ability to directly compare DWI and histological results in the same nerve would be beneficial in future studies. Another limitation is that DWI was performed on excised *ex vivo* nerve, requiring different animals for each time point, as opposed to a longitudinal study in the same animal across time. Although this would be a more ideal approach for assessing nerve repair, collecting DWI data in rat sciatic nerve *in vivo* remains challenging due to time constraints and relatively poor resolution. Additionally, the nerves in this study exhibited lower T_2 than expected, possibly due to prolonged fixation, which reduced SNR. Obtaining higher SNR DWI images, whether through higher nerve T_2 or longer

scan times (scans were limited to overnight or 12 hr for this study), would help improve DKI and WMTI parameter estimates.

6.5 Conclusions

DTI, DKI, and WMTI models provided sensitive measures to each stage of degeneration and regeneration following acute peripheral nerve injury and repair. This study was the first to utilize DKI and WMTI in the assessment of peripheral nerve. DKI metrics did show slightly increased sensitivity compared with DTI to microstructural changes, yet the practical value of using DKI over conventional DTI in this particular tissue model is questionable. On the other hand, the intra-axonal diffusivity derived from WMTI did appear to demonstrate increased specificity to axon structure, making it a potentially useful tool for future studies evaluating peripheral nerve injury. Future work focused on quantitative histological validation of DWI metrics in acute peripheral nerve injury would be beneficial in elucidating the relationship between these metrics and the underlying microstructure.

6.6 Acknowledgements

The author thanks Ashkan Afshari and Lyly Nguyen for performing all animal surgeries. This work was supported by NIH grants R01 EB001744, R01 EB019980, and S10 RR029523.

6.7 References

Basser, P.J., Jones, D.K., 2002. Diffusion-tensor MRI: theory, experimental design and data analysis–a technical review. NMR Biomed. 15, 456–467.

Basser, P.J., Mattiello, J., LeBihan, D., 1994a. Estimation of the effective self-diffusion tensor from the NMR spin echo. J. Magn. Reson. Ser. B 103, 247–254.

Basser, P.J., Mattiello, J., LeBihan, D., 1994b. MR diffusion tensor spectroscopy and imaging. Biophys. J. 66, 259–267.

Beaulieu, C., 2002. The basis of anisotropic water diffusion in the nervous system–a technical review. NMR Biomed. 15, 435–455. doi: 10.1002/nbm.782

Beaulieu, C., Does, M.D., Snyder, R.E., Allen, P.S., 1996. Changes in water diffusion due to Wallerian degeneration in peripheral nerve. Magn. Reson. Med. 36, 627–631.

Bendszus, M., Stoll, G., 2005. Technology insight: visualizing peripheral nerve injury using MRI. Nat. Clin. Pract. Neurol. 1, 45–53.

Bendszus, M., Wessig, C., Solymosi, L., Reiners, K., Koltzenburg, M., 2004. MRI of peripheral nerve degeneration and regeneration: correlation with electrophysiology and histology. Exp. Neurol. 188, 171–177.

Boyer, R.B., Kelm, N.D., Riley, D.C., Sexton, K.W., Pollins, A.C., Shack, R.B., Dortch, R.D., Nanney, L.B., Does, M.D., Thayer, W.P., 2015. 4.7-T diffusion tensor imaging of acute traumatic peripheral nerve injury. Neurosurg. Focus 39, E9–9. doi: 10.3171/2015.6.FOCUS1590

Campbell, W.W., 2008. Evaluation and management of peripheral nerve injury. Clin. Neurophysiol. 119, 1951–1965.

Cheung, M.M., Hui, E.S., Chan, K.C., Helpern, J.A., Qi, L., Wu, E.X., 2009. Does diffusion kurtosis imaging lead to better neural tissue characterization? A rodent brain maturation study. NeuroImage 45, 386–392. doi: 10.1016/j.neuroimage.2008.12.018

Does, M.D., Snyder, R.E., 1996. Multiexponential T2 relaxation in degenerating peripheral nerve. Magn. Reson. Med. 35, 207–213.

Falangola, M.F., Jensen, J.H., Babb, J.S., Hu, C., Castellanos, F.X., Di Martino, A., Ferris, S.H., Helpern, J.A., 2008. Age-related non-Gaussian diffusion patterns in the prefrontal brain. J. Magn. Reson. Imaging 28, 1345–1350. doi: 10.1002/jmri.21604

Fieremans, E., Benitez, A., Jensen, J.H., Falangola, M.F., Tabesh, A., Deardorff, R.L., Spampinato, M.V.S., Babb, J.S., Novikov, D.S., Ferris, S.H., Helpern, J.A., 2013. Novel white matter tract integrity metrics sensitive to Alzheimer disease progression. AJNR Am. J. Neuroradiol. 34, 2105–2112. doi: 10.3174/ajnr.A3553

Fieremans, E., Jensen, J.H., Helpern, J.A., 2011. White matter characterization with diffusional kurtosis imaging. NeuroImage 58, 177–188. doi: 10.1016/j.neuroimage.2011.06.006

Gaudet, A.D., Popovich, P.G., Ramer, M.S., 2011. Wallerian degeneration: gaining perspective on inflammatory events after peripheral nerve injury. J. Neuroinflammation 8, 110.

Grant, G.A., Goodkin, R., Kliot, M., 1999. Evaluation and surgical management of peripheral nerve problems. Neurosurgery 44, 825–839.

Guggenberger, R., Markovic, D., Eppenberger, P., Chhabra, A., Schiller, A., Nanz, D., Prussmann, K., Andreisek, G., 2012. Assessment of median nerve with MR neurography by using diffusion-tensor imaging: normative and pathologic diffusion values. Radiology 265, 194–203. doi: 10.1148/radiol.12111403

Hui E.S., Cheung M.M., Qi L, Wu E.X., 2008. Towards better MR characterization of neural tissues using directional diffusion kurtosis analysis. NeuroImage 42, 122-134.

Jelescu, I.O., Zurek, M., Winters, K.V., Veraart, J., Rajaratnam, A., Kim, N.S., Babb, J.S., Shepherd, T.M., Novikov, D.S., Kim, S.G., 2016. In vivo quantification of demyelination and recovery using compartment-specific diffusion MRI metrics validated by electron microscopy. NeuroImage 132, 104–114.

Jensen, J.H., Helpern, J.A., 2010. MRI quantification of non-Gaussian water diffusion by kurtosis analysis. NMR Biomed. 23, 698–710. doi: 10.1002/nbm.1518

Jensen, J.H., Helpern, J.A., Ramani, A., Lu, H., Kaczynski, K., 2005. Diffusional kurtosis imaging: The quantification of non-gaussian water diffusion by means of magnetic resonance imaging. Magn. Reson. Med. 53, 1432–1440. doi: 10.1002/mrm.20508

Kelm, N.D., West, K.L., Carson, R.P., Gochberg, D.F., Ess, K.C., Does, M.D., 2016. Evaluation of diffusion kurtosis imaging in ex vivo hypomyelinated mouse brains. NeuroImage 124, 612–626. doi: 10.1016/j.neuroimage.2015.09.028

Le Bihan, D., Mangin, J.F., Poupon, C., Clark, C.A., Pappata, S., Molko, N., Chabriat, H., 2001. Diffusion tensor imaging: concepts and applications. J. Magn. Reson. Imaging 13, 534–546.

Lehmann, H.C., Zhang, J., Mori, S., Sheikh, K.A., 2010. Diffusion tensor imaging to assess axonal regeneration in peripheral nerves. Exp. Neurol. 223, 238–244.

Li, X., Chen, J., Hong, G., Sun, C., Wu, X., Peng, M.J., Zeng, G., 2013. In vivo DTI longitudinal measurements of acute sciatic nerve traction injury and the association with pathological and functional changes. Eur. J. Radiol. 82, e707–e714.

Lu, H., Jensen, J.H., Ramani, A., Helpern, J.A., 2006. Three-dimensional characterization of non-gaussian water diffusion in humans using diffusion kurtosis imaging. NMR Biomed. 19, 236–247. doi: 10.1002/nbm.1020

Morisaki, S., Kawai, Y., Umeda, M., Nishi, M., Oda, R., Fujiwara, H., Yamada, K., Higuchi, T., Tanaka, C., Kawata, M., 2011. In vivo assessment of peripheral nerve regeneration by diffusion tensor imaging. J. Magn. Reson. Imaging 33, 535–542.

Wu, E.X., Cheung, M.M., 2010. MR diffusion kurtosis imaging for neural tissue

characterization. NMR Biomed. 23, 836–848. doi: 10.1002/nbm.1506

CHAPTER 7

CONCLUSIONS AND FUTURE DIRECTIONS

7.1 Conclusions

The objective of this work was to provide thorough evaluation and validation of advanced DWI models, DKI and WMTI, in a variety of neural tissue models related to clinically-significant neurological conditions. Previously, experimental evaluation of these imaging methods was limited, so this work seeks to fill in that gap, offering improved insight into what these metrics actually mean in a practical setting and how they can be applied for future assessments of neural tissue.

First, these DWI models were evaluated in hypo- and hypermyelinated adult mouse brain through comparisons to other myelin-specific MR methods and extensive EM measurements of axons and myelin morphology. From this work, it was determined that DKI offered improved sensitivity over DTI in distinguishing between varying levels of brain myelination, as well as, provided complementary information regarding diffusion in the intra- and extra-axonal space. WMTI demonstrated increased specificity to white matter microstructure, including axon fraction and myelin thickness. This work was the first to implement 3D DKI and WMTI imaging protocols for the study of mouse brain, as well as compare DKI and WMTI metrics to morphometric EM measures of axons and myelin.

Second, the advanced DWI models were assessed in both normally-developing and abnormally-developing mouse brain with histological validation. This work verified the relationship between DWI metrics and myelination shown in adult mice, making these

associations more widely-applicable to other studies of brain white matter. Again, DKI exhibited improved sensitivity over DTI, with a better ability to distinguish microstructural changes between different ages during development. Also, the biophysical WMTI model provided specificity to axon fraction and myelin thickness. This was the first study to evaluate DKI metrics in developing brain with EM histological validation. Additionally, this was the first work to examine WMTI parameters during this stage of brain development. Finally, this study was the first to provide tract-based measures of other myelin-specific MR measures in mouse brain, as well as, across brain development in general.

Lastly, DTI, DKI, and WMTI metrics were evaluated in an animal model of acute peripheral nerve injury and repair, providing sensitivity to each stage of degeneration and regeneration. DKI showed slightly increased sensitivity over DTI, yet WMTI intra-axonal diffusivity provided increased specificity to axon structure, making it potentially useful for future studies assessing peripheral nerve injury. This study was the first to evaluate peripheral nerve with DKI or WMTI.

7.2 Future Directions

There are multiple future directions stemming from this work. One such aim would be to expand upon the evaluation of the transgenic mouse models utilized in this work. This could include the translation of the imaging methods presented to *in vivo* imaging, allowing for longitudinal evaluation of mice across abnormal development, which would provide additional insight into the microstructural changes that are occurring. Additionally, this could provide for improved evaluation of potential treatments for tuberous sclerosis complex.

Another future direction would be the application of these DWI methods to other mouse models of neurological disorders and disease. Now that the relationship between these imaging metrics and tissue microstructure is better established, these DWI methods could be useful in providing noninvasive evaluation of the vast number of transgenic mouse models utilized in neuroscience research. Additionally, applying these DWI methods in a variety of animal models will help improve understanding of the metrics themselves and how they may be useful in a clinical setting, where the conditions may be more complex and confounding factors are more common.

Finally, it would be useful to provide histological validation of the DWI metrics in peripheral nerve injury. Having direct comparisons of the DKI and WMTI parameters to quantitative measures of axons, myelin, and intra- and extra-axonal spaces in the same nerve would provide confirmation of hypothesized relationships between DWI and injured peripheral nerve.

Overall, this dissertation provided significant advancement in the experimental knowledge of the DKI and WMTI models and how they can be useful in detecting neurological diseases and disorders, as well as, evaluating potential treatments.